
**Pacific Northwest
National Laboratory**

Operated by Battelle for the
U.S. Department of Energy

**A New Innovative Spherical Cermet
Nuclear Fuel Element to Achieve an Ultra-
Long Core Life for use in Grid-Appropriate
LWRs**

DJ Senior
CL Painter
KJ Geelhood
DW Wootan
GH Meriwether

JM Cuta
HE Adkins
DW Matson
CP Abrego

December 2007

Prepared for the U.S. Department of Energy
under Contract DE-AC05-76RL01830



DISCLAIMER

This report was prepared as an account of work sponsored by an agency of the United States Government. Neither the United States Government nor any agency thereof, nor Battelle Memorial Institute, nor any of their employees, makes **any warranty, express or implied, or assumes any legal liability or responsibility for the accuracy, completeness, or usefulness of any information, apparatus, product, or process disclosed, or represents that its use would not infringe privately owned rights.** Reference herein to any specific commercial product, process, or service by trade name, trademark, manufacturer, or otherwise does not necessarily constitute or imply its endorsement, recommendation, or favoring by the United States Government or any agency thereof, or Battelle Memorial Institute. The views and opinions of authors expressed herein do not necessarily state or reflect those of the United States Government or any agency thereof.

PACIFIC NORTHWEST NATIONAL LABORATORY

operated by

BATTELLE

for the

UNITED STATES DEPARTMENT OF ENERGY

under Contract DE-AC05-76RL01830

Printed in the United States of America

Available to DOE and DOE contractors from the
Office of Scientific and Technical Information,
P.O. Box 62, Oak Ridge, TN 37831-0062;
ph: (865) 576-8401
fax: (865) 576-5728
email: reports@adonis.osti.gov

Available to the public from the National Technical Information Service,
U.S. Department of Commerce, 5285 Port Royal Rd., Springfield, VA 22161
ph: (800) 553-6847
fax: (703) 605-6900
email: orders@ntis.fedworld.gov
online ordering: <http://www.ntis.gov/ordering.htm>



This document was printed on recycled paper.
(9/2003)

**A New Innovative Spherical Cermet Nuclear Fuel
Element to Achieve an Ultra-Long Core Life for use
in Grid-Appropriate LWRs**

| | |
|----------------|--------------|
| DJ Senor | JM Cuta |
| CL Painter | HE Adkins |
| KJ Geelhood | DW Matson |
| DW Wootan | C. P. Abrego |
| GH. Meriwether | |

December 2007

Prepared for the U.S. Department of Energy
under Contract DE-AC05-76RL01830

Pacific Northwest National Laboratory
Richland, Washington 99352

Summary

PNNL has proposed the Atoms for Peace Reactor (AFPR-100) concept as a 100 MWe, inherently safe, proliferation-resistant reactor that would be ideal for deployment to nations with emerging economies that decide to select nuclear power for the generation of carbon-free electricity. The basic concept of the AFPR is a water-cooled fixed particle bed, randomly packed with spherical fuel elements. The cylindrical core is approximately 3 m in height and 3 m in diameter, and consists of a series of four annular rings containing the spherical fuel elements. The reactor core is cooled by single-phase water flow within the particle bed at such a low rate that the bed will not fluidize. The concept incorporates a 20+ year core life requirement to enhance the proliferation resistance attribute associated with reactor. The ability to achieve an ultra long core life greatly reduces the need to handle fresh and spent fuel on site during the life of a plant, which in turn will greatly simplify safeguards oversight and the associated cost.

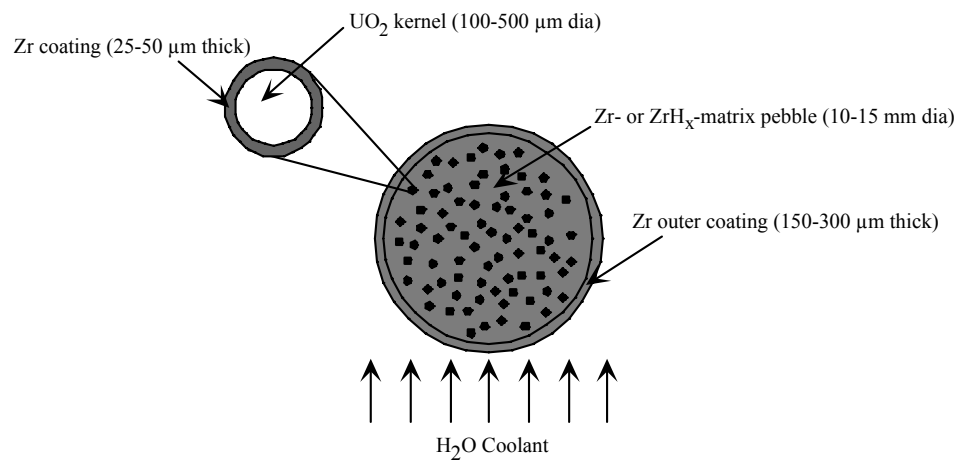
The concept relies heavily on the use of existing technology which is one advantage over other small reactor concepts currently being pursued. The ultra long core life is achieved by an innovative new spherical cermet fuel element, which relies on the use of common fuels, materials, and fabrication techniques, albeit in a somewhat novel way. The design of this new innovative fuel is the subject of this report. The feasibility of fabricating such a fuel will be discussed in a later report.

The new spherical cermet fuel consists of coated UO_2 kernels embedded in a zirconium, or zirconium hydride, matrix which is then overcoated with a protective outer fuel-free layer as shown. The spherical cermet fuel elements are envisioned to be 10-15 mm in diameter. The spherical cermet fuel element

provides structural stability over a service life of about 20 years and appears to be fabricable with existing technology. In general, the spherical fuel cermet fuel elements offer the following advantages over existing rodded fuel technology:

- high thermal conductivity,
- low fuel temperatures,
- good fission product retention, and
- good performance at high burnup.

Analyses of reactor physics performance parameters show that the spherical cermet fuel elements enable long core lifetime, easily-tailored power distribution, and attractive spent fuel isotopic composition. A fresh fuel enrichment of 12% provides sufficient initial reactivity to maintain criticality for at least 20 years of operation without refueling. The low fuel temperatures allow for higher burnup to be achieved due to reduced fission gas release and corrosion of the outer protective layer. The fuel average burnup for



the core over a 20 year period is about 53 GWD/MTU. A fuel free coating layer made of Zr (or Zr-base alloys such as Zr-1Nb) was selected to ensure good performance over a 20 year lifetime. The resultant plutonium isotopic composition is similar to that contained in commercial light water reactor spent fuel.

Evaluation of thermal-hydraulics characteristics of the core design shows that single-phase vertical upflow through a core fueled with such a fuel can remove 300 MW of heat with a reasonably low pressure drop for a relatively wide range of pressures and inlet temperatures. Based on analysis of the preliminary core design, recommended normal operating parameters are

- core inlet temperature of 204°C (400°F)
- core exit pressure of 12.41 MPa (1800 psia)
- core exit subcooling of 16.7 °C (30 °F) below saturation at the core exit pressure.

These parameters produce the following operating conditions:

- core pressure drop of 0.0564 MPa (8.2 psi)
- total flow rate of 585 kg/sec (1290 lbm/sec), assuming 1.5% bypass flow
- core exit temperature of 310°C (590°F)
- steam generated at a pressure of 9.875 MPa (1432 psia).

These are not the only parameters that could produce acceptable operating conditions in the core, but they provide a reasonable starting point for more detailed analysis of core performance.

Contents

| | |
|---|------|
| Summary..... | iii |
| 1.0 Introduction..... | 1.1 |
| 2.0 Spherical Cermet Fuel Concept..... | 2.1 |
| 2.1 Materials Selection..... | 2.1 |
| 2.2 Proposed Fuel Fabrication Method..... | 2.2 |
| 2.2.1 Kernel..... | 2.2 |
| 2.2.2 Zr Kernel Coating..... | 2.4 |
| 2.2.3 Pebble Fabrication..... | 2.6 |
| 2.2.4 Pebble Outer Coating..... | 2.7 |
| 2.3 Alternative Outer Coating Materials..... | 2.1 |
| 3.0 Fuel Performance Modeling..... | 3.1 |
| 3.1.1 Uranium Dioxide (UO ₂)..... | 3.1 |
| 3.1.2 Zirconium..... | 3.7 |
| 3.1.3 Zirconium Hydride (ZrH _{1.6})..... | 3.12 |
| 3.2 Spherical Cermet Fuel Effective Thermal Conductivity and Specific Heat..... | 3.15 |
| 3.3 Spherical Cermet Fuel Transient Thermal Analysis..... | 3.16 |
| 4.0 Neutronics Analysis..... | 4.1 |
| 4.1 AFPR Core Specifications for Analysis..... | 4.1 |
| 4.2 Methods..... | 4.2 |
| 4.3 Parametric Studies..... | 4.3 |
| 4.4 Analysis of Zr Base Case..... | 4.5 |
| 4.4.1 Description..... | 4.5 |
| 4.4.2 Burnup Analysis..... | 4.6 |
| 4.4.3 Decay Heat..... | 4.8 |
| 4.4.4 Fuel Isotopics..... | 4.9 |
| 4.4.5 Reactivity Coefficients..... | 4.9 |
| 4.5 Analysis of ZrH _{1.6} Base Case..... | 4.10 |
| 4.5.1 Description..... | 4.10 |
| 4.5.2 Burnup Analysis..... | 4.10 |
| 4.5.3 Decay Heat..... | 4.13 |
| 4.5.4 Fuel Isotopics..... | 4.13 |
| 4.6 Analysis Alternatives..... | 4.13 |
| 4.6.1 Radial Power Distribution Sensitivities..... | 4.13 |
| 4.6.2 Burnable Poison Studies..... | 4.16 |
| 4.6.3 Core Lifetime Studies..... | 4.18 |

| | | |
|-----|---|------|
| 4.7 | Spectral Comparisons..... | 4.20 |
| 4.8 | Conclusions | 4.22 |
| 5.0 | Thermal Hydraulics Analysis | 5.1 |
| 5.1 | Core Design for Single-Phase Flow | 5.2 |
| 5.2 | Core Thermal-Hydraulics for Single-Phase Flow | 5.5 |
| | 5.2.1 Core Operating Conditions..... | 5.5 |
| | 5.2.2 Material Temperatures in AFPR Core..... | 5.13 |
| 5.3 | Core Cooling in Accident Conditions | 5.18 |
| | 5.3.1 Short-term Response of AFPR Core to Accident Conditions | 5.19 |
| | 5.3.2 Long-term Response of AFPR Core to Accident Conditions..... | 5.20 |
| 6.0 | Conclusions and Recommendations for Future Work | 6.1 |
| 7.0 | References..... | 7.1 |

Figures

| | | |
|--------------|---|------|
| Figure 1.1 | Iterative Process Used to Evaluate Feasibility of Spherical Cermet Fuel Elements in the AFPR System..... | 1.4 |
| Figure 2.1. | Schematic representation of the AFPR pebble fuel concept..... | 2.1 |
| Figure 2.2. | The gel precipitation process for producing UO_2 fuel kernels. | 2.3 |
| Figure 2.3. | Cross sectional drawing of a FBCVD reactor for coating particle surfaces. | 2.5 |
| | (Pierson, 1999)..... | 2.5 |
| Figure 2.4. | PBMR pebble manufacturing process. | 2.7 |
| Figure 2.5. | Stylized representation of the spray process proposed for applying an outer coating to the pebble. Note that for thicker coatings, multiple spray/recrystallization cycles may be required. | 2.8 |
| Figure 2.6. | Photographs of samples after 1826 hours at $300^\circ C$. The metals are lightly corroded with oxide films but the ceramics are visually unaffected. However, the YSZ materials did exhibit weight gains. | 2.3 |
| Figure 3.1. | Thermal conductivity for 95% T.D. UO_2 fuel at various burnup levels | 3.2 |
| Figure 3.2. | Specific heat for 95% T.D. UO_2 fuel..... | 3.3 |
| Figure 3.3. | Fuel swelling and densification model predictions as a function of burnup for 95% T.D. fuel | 3.4 |
| Figure 3.4. | Young's modulus for UO_2 as a function of temperature for 95% T.D. fuel..... | 3.5 |
| Figure 3.5. | Shear modulus for UO_2 as a function of temperature for 95% T.D. fuel | 3.5 |
| Figure 3.6. | Thermal expansion strain for 95% T.D. UO_2 fuel | 3.6 |
| Figure 3.7. | Athermal fission gas release model | 3.7 |
| Figure 3.8. | Thermal conductivity for zirconium..... | 3.8 |
| Figure 3.9. | Specific heat for zirconium..... | 3.9 |
| Figure 3.10. | Young's modulus for unirradiated, fully annealed zirconium..... | 3.10 |
| Figure 3.11. | Shear modulus for unirradiated, fully annealed zirconium..... | 3.11 |
| Figure 3.12. | Thermal expansion strain for zirconium..... | 3.12 |
| Figure 3.13. | Thermal conductivity of ZrH_x for various hydrogen concentrations | 3.13 |
| Figure 3.14. | Specific heat of ZrH_x for various hydrogen concentrations..... | 3.14 |
| Figure 3.15. | ZrH_x density as a function of hydrogen content | 3.14 |

| | |
|---|------|
| Figure 3.16. Dependence of Pebble Time Constant on Pebble Diameter for Zr and ZrH _{1.6} Pebble Matrices | 3.16 |
| Figure 3.17. Dependence of Pebble ΔT on Pebble Diameter for Zr and ZrH _{1.6} Pebble Matrices | 3.17 |
| Figure 4.1. AFPR 1/8th Core Model Horizontal Slice..... | 4.2 |
| Figure 4.2. Variation of kernel packing fraction with Zr and ZrH _{1.6} matrix..... | 4.4 |
| Figure 4.3. Variation of pebble diameter for Zr matrix | 4.4 |
| Figure 4.4. Variation of fuel kernel diameter for Zr matrix..... | 4.5 |
| Figure 4.5. Burnup reactivity loss over 20 years for Zr base case | 4.6 |
| Figure 4.6. Burnup in each fuel region over 20 years for Zr base case..... | 4.7 |
| Figure 4.7. Fuel kernel power density in each fuel region for 20 year irradiation for Zr base case | 4.8 |
| Figure 4.8. Decay power for the AFPR core as a function of time after shutdown | 4.9 |
| Figure 4.9. Burnup reactivity loss over 20 years for ZrH _{1.6} base case | 4.11 |
| Figure 4.10. Burnup in each fuel region over 20 years for ZrH _{1.6} base case..... | 4.12 |
| Figure 4.11. Power density in each fuel region for 20 year irradiation for ZrH _{1.6} base case | 4.13 |
| Figure 4.12. Impact of fuel enrichment zoning on radial power distributions..... | 4.14 |
| Figure 4.13. Impact of moderator rods and radial reflector on radial power distributions | 4.15 |
| Figure 4.14. Impact of adding a radial reflector on the radial power distribution in the ZrH core..... | 4.15 |
| Figure 4.15. WIMS results using different burnable absorbers | 4.16 |
| Figure 4.16. Burnup reactivity loss over 20 years for Zr case with 2 zone boron burnable poison..... | 4.17 |
| Figure 4.17. Power density changes over 20 years for Zr case with 2 zone boron burnable poison | 4.18 |
| Figure 4.18. Effect of increasing kernel packing fraction on burnup reactivity loss for Zr base case.... | 4.19 |
| Figure 4.19. Burnup reactivity loss over 20 years for Zr case with core volume doubled by increasing the core radius | 4.19 |
| Figure 4.20. Burnup for each fuel region over 20 years for Zr case with core volume doubled by increasing the core radius | 4.20 |
| Figure 4.21. Neutron spectrum comparison between Zr base case, ZrH base case, and B burnable poison case..... | 4.21 |
| Figure 4.22. Comparison of neutron spectra for current cermet fuel cases with previous micro-fuel concept..... | 4.22 |
| Figure 5.1. Conceptual Illustration of Packed Bed Core with Vertical Upflow Cooling..... | 5.3 |
| Figure 5.2. Estimated Operating Temperatures and Pressures in the AFPR at 300 MW(thermal)..... | 5.4 |
| Figure 5.3. AFPR Core Flow Rate as a function of Inlet Temperature and Exit Pressure..... | 5.8 |
| Figure 5.4. Core Pressure Drop as a function of Inlet Temperature and Exit Pressure | 5.9 |
| Figure 5.5. Core Pressure Drop as a function of Core Exit Subcooling at Core Inlet Temperature of 204°C (400°F)..... | 5.10 |
| Figure 5.6. Core Pressure Drop as a function of Core Exit Subcooling at Core Inlet Temperature of 225°C (437°F)..... | 5.11 |
| Figure 5.7. Core Pressure Drop as a function of Core Exit Subcooling at Core Inlet Temperature of 250°C (482°F)..... | 5.12 |
| Figure 5.8. Saturation Pressure at Core Exit Temperature as a Function of Core Exit Subcooling | 5.12 |
| Figure 5.9. Estimated Nusselt Number for Acceptable Range of Fuel Particle Surface Temperatures.. | 5.15 |
| Figure 5.10. Fuel Particle Center Temperatures for Acceptable Range of Fuel Particle Surface Temperatures | 5.17 |
| Figure 5.11. Fuel Particle Center and Surface Temperatures as a Function of Nusselt Number for Heat Transfer to Coolant..... | 5.17 |

| | |
|--|------|
| Figure 5.12. Core Flow Rate and Power Decay Forcing Functions for Complete Loss of Flow Accident (CLOFA) in typical LWRs..... | 5.18 |
| Figure 5.13. Flow Rate Required to Remove Decay Heat in Hot Shutdown Conditions for AFPR Core..... | 5.21 |
| Figure 5.14. Friction Pressure Drop in Particle Bed Core for Flow Rate Required to Remove Decay Heat in Hot Shutdown Conditions..... | 5.22 |
| Figure 6.1 PWR Pebble Bed Fuel Assembly..... | 6.1 |

Tables

| | |
|--|------|
| Table 1.1 Comparison of AFPR Concept with other Small Reactors..... | 1.2 |
| Table 2.1. Weight Gain Data Associated from 1011 hours of Autoclave testing at 288°C..... | 2.2 |
| Table 3.1. Effective thermal properties for Spherical Cermet Fuel Element at normal and accident conditions..... | 3.15 |
| Table 3.2. Time constants for Spherical CERMET Fuel Element at normal and accident conditions ... | 3.17 |
| Table 3.3. Peak Center Temperatures for Spherical CERMET Fuel Element during normal and accident conditions..... | 3.18 |
| Table 4.1. AFPR Core Specifications..... | 4.1 |
| Table 4.2. AFPR Core Model Radial Dimensions..... | 4.3 |
| Table 4.3 Fuel Parameters Selected for Burnup Analysis..... | 4.5 |
| Table 4.4. Fuel Specifications for Zr base case..... | 4.6 |
| Table 4.5. Core average isotopics of spent fuel after 20 years of operation for Zr base case..... | 4.9 |
| Table 4.6. Fuel Specifications for ZrH1.6 base case..... | 4.10 |
| Table 4.7. Core average isotopics of spent fuel after 20 years of operation for ZrH1.6 base case..... | 4.13 |
| Table 5.1. AFPR Core Design Parameters Relevant to Thermal-Hydraulic Analysis..... | 5.5 |
| Table 5.2. Decay Heat After Shutdown in AFPR Core..... | 5.21 |
| Table 6.1 Summary of Key AFPR System Characteristics with Spherical Cermet Fuel Elements..... | 6.2 |

1.0 Introduction

Light water reactors (LWRs) currently dominate commercial nuclear power. The need for power plants capable of providing large baseline loads for use on well-developed electricity grids has historically driven the development of nuclear power reactors, resulting in large 1000+ MWe commercial units. Markets with much smaller power needs and less well-developed electrical distribution infrastructure, such as those found in developing nations, have not yet influenced the design of nuclear power reactors and technologies. A different reactor design approach, tailored for this market segment, could help meet the rising power demands associated with economic growth and urbanization, while avoiding the use of fossil fuels that would otherwise be burned in power plants. If deployed to developing nations, there will be a need to ensure that the reactor fuel cannot be easily diverted for use in nuclear or radiological weapons.

In 2005, the US Department of Energy began developing program elements associated with what would be announced in 2006 as the Global Nuclear Energy Partnership (GNEP). As part of President Bush's Advanced Energy Initiative, GNEP seeks to develop a worldwide consensus on enabling the expanded use of economical, carbon-free nuclear energy to meet growing electricity demand. An element of GNEP is to provide small reactors suitable for meeting the growing energy demands of emerging economies in developing nations that currently depend on oil and other fossil fuels. Developing smaller-scale, passively-safe, secure and proliferation-resistant reactors is necessary before nuclear energy is viable for use in developing nations with small-grid markets.

The Atoms for Peace Reactor (AFPR) is an evolutionary small reactor concept being developed by the Pacific Northwest National Laboratory (PNNL). The reactor system is envisioned to be proliferation-resistant, passively-safe, and economical for potential deployment to nations with emerging economies. The enabling feature of this reactor concept is the particulate fuel form. The fuel form provides fission product containment, low stored energy, and long core life. Studies of the AFPR system before FY06 focused on the neutronics and thermal-hydraulics characteristics of the system (Tsiklauri et al. 2005). These studies concluded the concept was viable, but performance of the reactor hinged on the ability of the fuel particles to perform as designed.

A comparison of currently-available small reactor designs is provided in Table 1.1. The only operational reactor among these is the Russian built KLT-40S that uses 36% enriched uranium with a 3-4 year refueling interval. The use of greater than 20% enriched fuel is less than desirable from a proliferation risk perspective. The other LWR reactor concepts have relatively short core lifetimes that will require frequent access to the core and significant fresh and spent fuel handling. The fast reactors have longer core lifetimes and correspondingly less need to handle fuel, but they will require significant investment in reactor technology and materials research due to higher operating temperatures and immature technology. The situation is similar for the pebble bed modular reactor (PBMR), a high-temperature gas-cooled reactor currently under development in South Africa. The AFPR concept offers advantages over these other reactors in that it has a long core life and the technology needed to build the reactor exists today; however, it is acknowledged that an extensive fuel qualification program would need to be undertaken.

Table 1.1 Comparison of AFPR Concept with other Small Reactors

| Reactor | Designer | Coolant | Fuel | Spectrum | Temp (°C) | Refueling (yr) | Status |
|---------|------------------|---------|---------------------------------|----------|-----------|----------------|---|
| AFPR | PNNL | Water | Zr/LEUO ₂ cermet | Thermal | 300 | 20+ | Concept, extension of existing technology |
| IRIS | Westinghouse | Water | Zr-alloy clad LEUO ₂ | Thermal | 300 | 5 | Under development, based on existing technology |
| MSBWR | General Electric | Water | Zr-alloy clad LEUO ₂ | Thermal | 300 | 10 | Under development, based on existing technology |
| SMART | South Korea | Water | Zr-alloy clad LEUO ₂ | Thermal | 300 | 3 | Under development, based on existing technology |
| KLT-40S | Russia | Water | 36% enriched UO ₂ | Thermal | 300 | 3-4 | Operational |
| STAR | Westinghouse | Pb | U-transuranic nitride fuel | Fast | 578 | 15-20 | Under development, needs new technology |
| 4S | Toshiba | Na | U-Zr Metal Fuel | Fast | 510 | 30 | Under development, needs new technology |
| PBMR | South Africa | He | TRISO | Thermal | 900 | Continuous | Developed |

In early 2006, a detailed feasibility assessment was performed by PNNL on the original reactor concept which assumed the use of a modified tristructural isotropic (TRISO) fuel (Painter et al. 2006, Geelhood et al. 2006). The modified TRISO fuel was similar to the German TRISO fuel in that spherical UO₂ kernels surrounded by graphite and ceramic coating layers needed to provide fission gas volume, solid swelling accommodation, fission product retention, and coolant corrosion resistance was coated with a outer protective layer to protect against waterside corrosion. TRISO fuel was originally developed for high-temperature gas reactor applications with coolant temperatures around 800°C. The feasibility assessment found that the lower coolant temperature of the AFPR (around 300°C) would result in significant irradiation-induced swelling in the SiC fission product barrier coating layer. Finite element modeling demonstrated that the swelling would be sufficient to cause the SiC layer, adjacent pyrolytic carbon (PyC) layers, and the outer corrosion protection coating layer to fail during the first year of operation. Other issues with the original fuel concept were identified, including anisotropic swelling of the PyC, crud deposition in the fuel particle bed, and difficulties associated with reliable management of the small (1-2 mm diameter) fuel particles. As a result, the modified TRISO fuel particles were judged inappropriate for use in AFPR as conceived.

An alternative fuel concept was developed by PNNL later in 2006 that incorporates the same UO_2 fuel kernels of the modified TRISO concept, but eliminates the graphite and ceramic coatings that are incompatible with the low-temperature, moderate-to-high burnup environment of the AFPR. Instead, the new fuel concept incorporates Zr-coated fuel kernels, mixed with an appropriate quantity of Zr powder, and hot pressed to form a spherical cermet pebble. The pebble is then coated with a corrosion protection layer of Zr or Zr-base alloy. Neutronic and thermal-hydraulic evaluations performed during 2006 demonstrated that not only are the cermet fuel elements feasible, but in fact offer many advantages over the original TRISO fuel concept including simpler fuel handling, lower pressure drop across the core, better heat transfer characteristics, simplified core design due to better moderation, and sufficient excess reactivity to allow a 20-year core life with moderate-to-high burnup (50–90 GW-d/MTU). In addition, the cermet fuel elements allow retention of other attractive features of the AFPR, including low stored energy in the fuel, rapid thermal response, robust fission product containment, and simple core design. The proliferation resistance of the AFPR concept is maintained with the cermet fuel concept through high burnup fuel, a novel fuel form that would require significant development to reprocess, and eliminating any need to open the pressure vessel during the 20-year core lifetime.

During the course of developing the new cermet fuel concept, it became clear that certain design aspects of the original AFPR system could be simplified due to the characteristics of the new fuel form. For example, more than a factor of three difference in the thermal flux component of the neutron spectrum existed between the highest and lowest density coolant regions when boiling was allowed in the bed. This significant difference would likely translate into a corresponding difference in specific power, since on the order of 70% of the fissions occur at thermal energies. Thus, local changes in the moderator/coolant density from boiling due to temperature or pressure variations could lead to significant local power differences. The stability of the coolant density gradient could become a concern for maintaining stable power operation of the reactor. Limiting the coolant to single phase flow in the fuel region significantly reduces this potential problem and simplifies the problem. As a result, in-core boiling was eliminated to provide more stability in localized power production, more uniform localized burnup, and lower pressure drop across the core. The change to single-phase flow in the core coupled with the larger size of the cermet pebbles significantly reduced the pressure drop across the core and allowed axial flow. This raises the possibility of natural convection cooling to remove decay heat in the event of a loss-of-flow accident. The elimination of in-core boiling coupled with the introduction of the cermet fuel elements also improved the moderator-to-fuel ratio so that moderator tubes were no longer necessary. This further simplified the system design while allowing more fuel in the core.

The interrelationship between material properties, neutronics, and thermal-hydraulics necessitates an iterative approach to fuel design. The approach taken in the present study to evaluate the feasibility of the spherical cermet fuel element concept for the AFPR system is illustrated in Figure 1.1. The following sections of the report will describe in detail the results obtained for materials (Section 2), fuel performance modeling (Section 3), neutronics (Section 4), and thermal-hydraulics (Section 5). In addition, an overall assessment of the proliferation resistance of the AFPR concept is included in Section 6. Finally, conclusions drawn from the work performed in 2006 are presented in Section 7. No attempt was made to evaluate the overall fuel cycle economics related to the use of this new fuel concept.

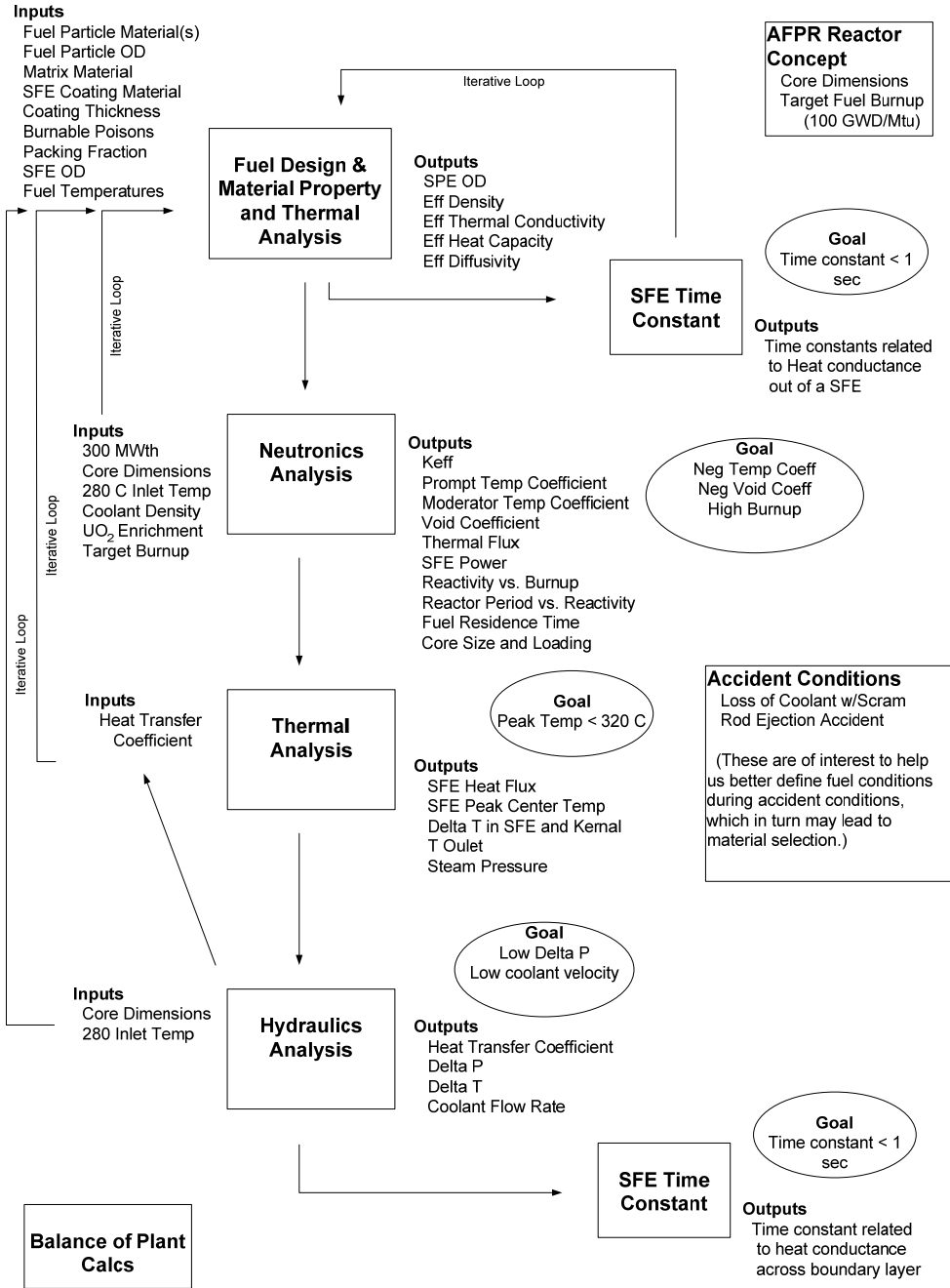


Figure 1.1 Iterative Process Used to Evaluate Feasibility of Spherical Cermet Fuel Elements in the AFPR System

2.0 Spherical Cermet Fuel Concept

The proposed spherical cermet fuel element concept for use as AFPR fuel incorporates small and dense UO_2 fuel kernels. The fuel kernels consist of low-enriched (i.e. less than 20% U-235) UO_2 and create heat via a controlled nuclear fission reaction. Additionally, the fuel kernels retain the majority of fission products within them due to low fuel temperatures. The individual fuel kernels have a thin Zr coating that acts as a fission product barrier and establishes a minimum separation distance between kernels to avoid hot spots in the fuel. The kernel coating also helps regulate the kernel packing fraction within the pebble. The Zr-coated kernels are embedded in a dense Zr or ZrH_x matrix to form a spherical pebble. The fuel element matrix must maintain its structural integrity throughout the life of the fuel element. The pebble outer surface is coated with a layer of Zr to provide an additional fission product barrier and protect the fuel-bearing portion of the pebble from the primary coolant. The primary advantage of the spherical cermet fuel element relative to more traditional LWR fuels is high thermal conductivity due to the small UO_2 kernels and lack of pellet-to-cladding gaps. A schematic of the AFPR pebble fuel concept is shown in Figure 2.1.

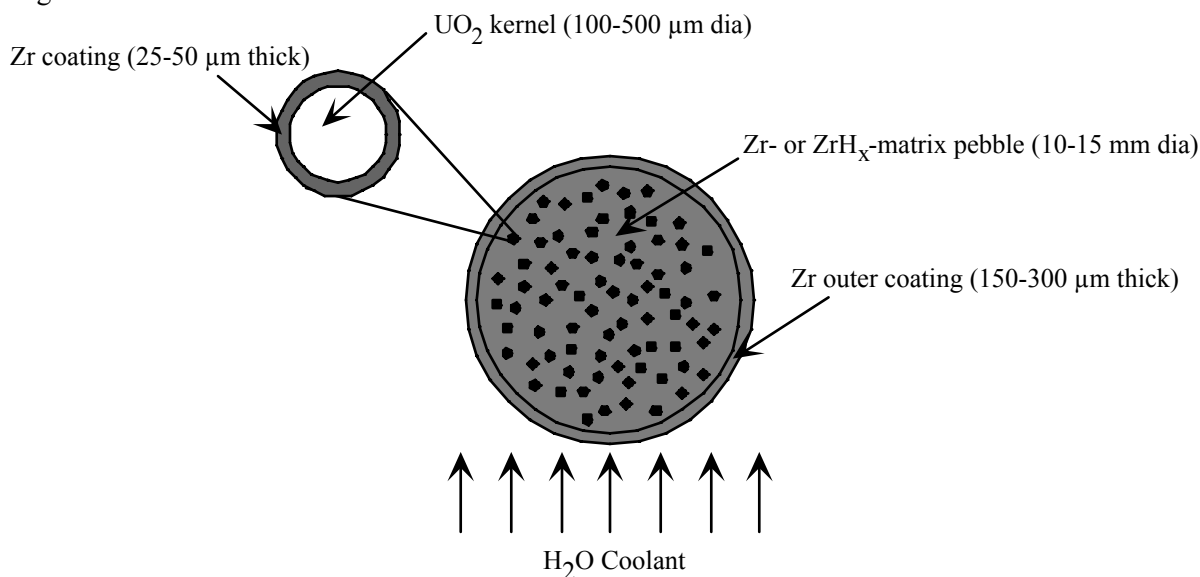


Figure 2.1. Schematic representation of the AFPR pebble fuel concept.

2.1 Materials Selection

The use of UO_2 as the reference fuel is based on the vast experience with this material, as well as the existing technology to produce spherical UO_2 kernels in the size range 100–500 μm . Previous experience with cermet fuels (although not Zr/ UO_2 cermets) and gas reactor pebble fuels suggests that kernel packing fractions¹ of 0.3 to 0.5 are reasonable. The Zr pebble matrix was selected primarily on the basis of low neutron absorption and minimal transmutation. Similarly, the Zr kernel coating and Zr outer coating were selected to maximize materials compatibility with the fuel, matrix, and coolant. The thickness of the Zr kernel coating will ultimately be determined by the kernel packing fraction and the desired minimum

¹ Packing Fraction – Defined as the volume of a kernel, times the number of kernels in a pebble, divided by the volume of the uncoated pebble.

kernel separation. The thickness of the outer coating will be determined by the acceptable material loss due to corrosion and wear during the life of the pebble. Using Zr or a Zr-base alloy for the outer coating will minimize regulatory concern, as this is a commonly-used material in a reactor environment with many years of data supporting its viability. To provide more moderation, a radiation-stable $ZrH_{1.6}$ matrix (Mueller et al. 1968) is also considered. Although more brittle than Zr and susceptible to corrosion in 300°C water, the $ZrH_{1.6}$ matrix has a higher thermal conductivity than Zr and could accommodate larger pebbles while retaining the desired thermal characteristics.

A wide range of candidate materials were initially considered as possible protective outer coatings, including metals such as Ti and V, alloys such as stainless steel and Zircaloy, ceramics such as carbides (SiC, TiC, ZrC, NbC, TaC, WC), nitrides (AlN, TiN, CrN, NbN), oxides (Y_2O_3 -stabilized ZrO_2 and $MgAl_2O_4$), CVD diamond, and nanolayered composites incorporating multiple ceramic coating layers. A study was completed early in 2006 to identify the requirements of the protective outer layer in order to function adequately in the AFPR environment (Painter et al. 2006). This allowed a targeted down-selection of material candidates for this application. Most metals and alloys are inadequate to protect the fuel particles for their projected lifetimes (~20 years) due to the loss of material through corrosion over time. A Zr or Zr-base alloy outer protective coating would lose approximately 100 μm of its thickness due to corrosion in 300°C water over 20 years based on empirical data obtained from LWR industry experience; however, the fuel cladding temperatures and heat flux in AFPR fuel are less than typically found in commercial fuel and therefore this should be a conservative upper estimate. This might be acceptable for outer coating thicknesses of 300 μm or more. Thus, because of its well-characterized properties and likely regulatory acceptance, Zr (or Zr-base alloys such as Zr-1Nb) were adopted as the reference outer protective coating.

Other materials continue to merit consideration for the outer coating. In the event that there is a problem with manufacturing the desired thick Zr or Zr-base alloy coating on the outer surface of the pebble, or if 100 μm of material loss over 20 years is determined to be too severe, an alternate outer coating material will be needed. The carbide ceramics and CVD diamond all exhibit swelling behavior similar to SiC, which would result in coating failure and potential fission product release early in life (Geelhood et al. 2006). The nitride ceramics have very little data on irradiation swelling, and exhibit other problems such as low toughness, high neutron absorption and high transmutation. The oxide ceramics, particularly Y_2O_3 -stabilized ZrO_2 , are very resistant to irradiation swelling, and exhibit acceptable mechanical, thermal, and nuclear properties. However, very little corrosion data are available for this material. As a result, it is likely that any credible alternate outer coating material will be a metal or alloy. After eliminating elements with unsatisfactory activation/transmutation characteristics, and focusing on metals with reasonably high melting points, the most likely candidates are Ti, V, or alloys such as Ti-6Al-4V or V-4Cr-4Ti. Metallurgically, these metals and alloys should be reasonably compatible with the Zr pebble matrix, and their thermal properties should not prove detrimental relative to Zr.

2.2 Proposed Fuel Fabrication Method

2.2.1 Kernel

There is considerable experience fabricating UO_2 kernels with the dimensions and properties envisioned for AFPR fuel. For example, fuel manufacturing for the Pebble Bed Modular Reactor (PBMR), currently under development in South Africa, uses a sol-gel process to produce kernels (PBMR 2001). Essentially the same process is used by Nuclear Fuel Industries in Japan to manufacture fuel kernels for the High

Temperature Test Reactor (Kato et al. 1998). This process, typically referred to as gel precipitation and shown schematically in Figure 2.2, is based on a German process originally developed during the 1970s. First, a uranyl nitrate solution is prepared by dissolving UO_2 powder in nitric acid. Next, the solution is conditioned by the addition of organic compounds. Gelled particles are then produced by reacting droplets of the solution with ammonia vapor and ammonium hydroxide solution. The gelled particles are aged, washed, dried, and then calcined (reduced) at $400^\circ C$ for one hour. Finally, the particles are sintered at $1700^\circ C$ for two hours. Dimensional and density controls are achieved by varying process parameters such as the sintering conditions.

A variation of the gel precipitation process, termed internal gelation, recently has been employed in the U.S. to produce UO_2 fuel kernels with diameters of 500 to 532 μm (Hunt and Collins 2004). In this approach, the starting solutions include acid-deficient uranyl nitrate and hexamethylenetetramine (HMTA) urea. These solutions are combined, chilled, and dispersed to form droplets in silicone oil. The silicone oil is heated to $60^\circ C$ to promote gelation. The gelled droplets are then aged, washed, dried, and sieved to eliminate non-spherical particles. Finally, the particles are calcined and sintered to produce the

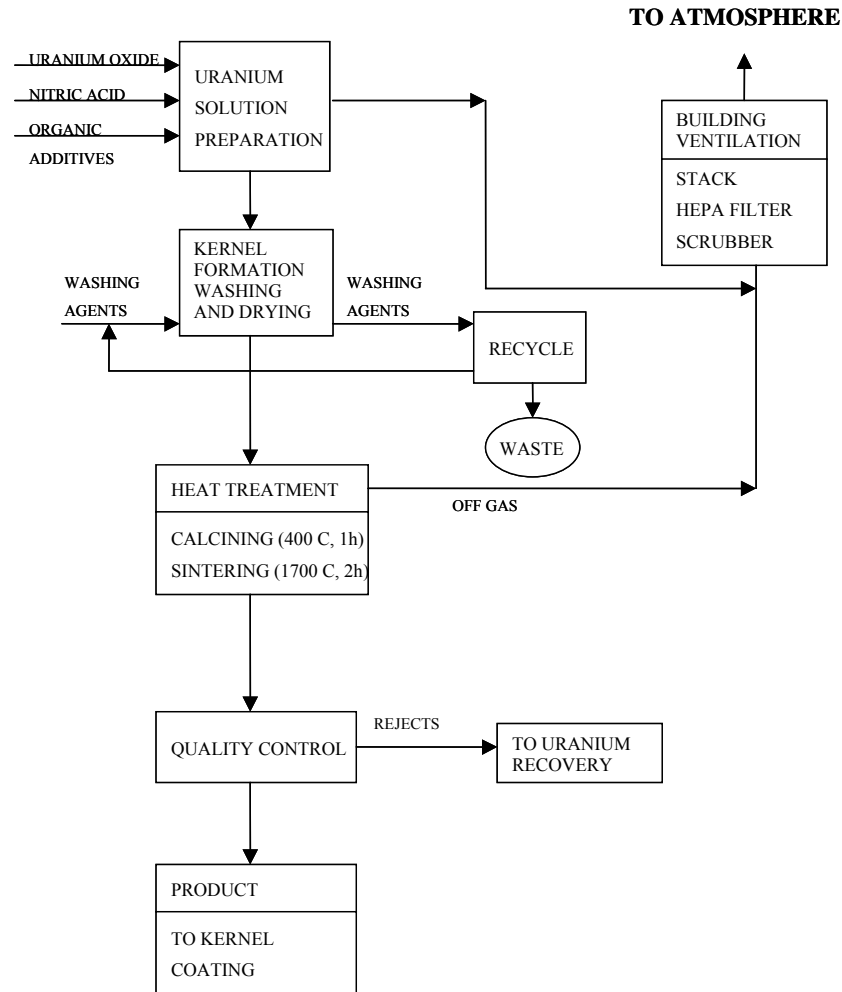


Figure 2.2. The gel precipitation process for producing UO_2 fuel kernels.

final kernels. One advantage of the internal gelation technique is the ability to homogeneously incorporate fine particles of other materials (e.g., ThO₂ or burnable absorbers) in the starting solution. However, the internal gelation process has not been demonstrated except in a laboratory setting. Because of the experience base associated with UO₂ kernel fabrication, further demonstration of this process for the purpose of establishing feasibility of the spherical cermet fuel element form is not necessary. Development work on the remainder of the fuel pebble manufacturing process can begin using surrogate materials such as ZrO₂ that reasonably mimic the relevant properties of UO₂.

2.2.2 Zr Kernel Coating

The Zr coating on the surface of the fuel kernel can be produced by chemical vapor deposition (CVD). Probably the most straightforward approach allowing the deposition of high purity zirconium involves CVD using thermal decomposition of a zirconium halide. This method was first developed to produce high-purity crystal bar Zr in the 1950s (Powell et al. 1966). The process is similar to methods used for commercial refining of chromium, titanium, thorium and hafnium. The process as used for crystal bar Zr fabrication involves the use of a resistively-heated filament (typically W or another refractory metal) in vacuum, into which a zirconium feedstock (typically impure) and iodine gas are introduced. The feedstock reacts with the iodine to form metal iodide vapors. When the filament is heated to the appropriate temperature (approximately 1200°C), only the ZrI₄ thermally decomposes on the hot surface and pure Zr metal is deposited. The volatile impurity iodides do not decompose at this temperature and are exhausted from the system. The Zr deposits produced by this method are relatively porous and brittle, and must be subsequently melted before any forming operations can be conducted. Deposition efficiencies of approximately 32% have been commercially demonstrated (Kodas and Hampden-Smith 1994).

The use of ZrI₄ as a precursor for conventional CVD processes is limited because of its relatively low volatility. Typically the precursor material must be vaporized by pressure reduction or heating before it can be introduced into the CVD reactor. More attractive zirconium precursors from the volatility perspective are the zirconium bromide and chloride salts. However, the byproducts of the decomposition reactions of the bromides and chlorides are more corrosive in nature than those of the iodides, requiring the use of corrosion-resistant materials in the CVD reactor and associated components. The temperatures required for clean dissociation of the zirconium halide also tend to be higher for the lower molecular weight halide species (e.g., ~1400°C for the bromide). Metallo-organic zirconium-containing precursors are also available that offer high volatility and relatively low decomposition temperatures. However, deposits produced by the metallo-organic CVD (MOCVD) approach tend to have high rates of impurity incorporation and are thus not commonly suitable for applications demanding the production of high purity metal coatings.

Application of a uniform CVD coating to the surfaces of small particles requires the use of a fluidized bed (FBCVD) in which a flowing gas imparts fluid-like properties to the particles, causing them to move relative to each other and be uniformly exposed to a coating precursor and to a heated zone. A nonreactive fluidizing gas is used in sufficient flow to allow movement of the particles within the bed without causing them to be blown out of the bed. Along with the nonreactive gas, a reactant precursor gas is introduced that will chemically produce the desired coating on the surface of the particles by the thermal decomposition process. Heating of the fluidized bed of particles is commonly accomplished using an inductive heating coil around the fluidized bed assembly. A stylized drawing of a fluidized bed CVD reactor is shown in Figure 2.3. Fluidized bed reactors have previously been used to apply pyrolytic

carbon, silicon carbide, alumina, and beryllia coatings on uranium oxide nuclear fuel particles for the purpose of containing nuclear fission products (Oxley, 1966).

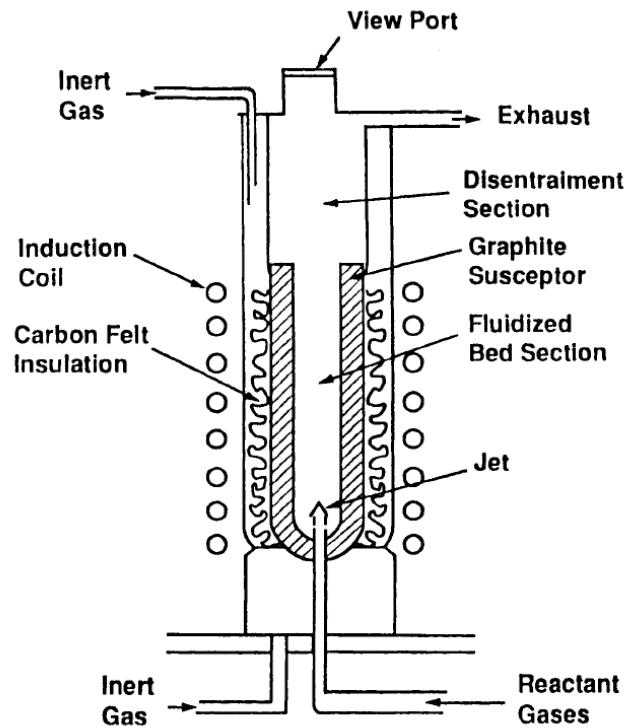


Figure 2.3. Cross sectional drawing of a FBCVD reactor for coating particle surfaces. (Pierson, 1999)

The proposed approach for producing Zr-coated UO_2 fuel kernels will be to utilize a ZrBr_4 precursor in a fluidized bed CVD reactor. In this scenario, a fluidized bed of fuel kernels would be inductively heated to the appropriate decomposition temperature and ZrBr_4 vapor would be passed through the fluidized bed by an inert carrier gas. Fluidizing the UO_2 kernels is an established process used during CVD coating of TRISO fuel particles, and should pose no significant technical coating problems (Kato et al. 1998). However, establishing an effective induction couple with the fluidized particles will require some demonstration, as will controlling the process to ensure uniform kernel temperatures and therefore uniform Zr deposition. Process development will be performed using surrogate kernels of the appropriate size fabricated from an alternative ceramic material (e.g., ZrO_2)

The primary issues related to the production of Zr coatings using the proposed approach will be 1) the high temperatures needed for reaction of the precursor to a fully metallic film, requiring a core particle having thermal stability to temperatures in excess of 1600°C (this should not be an issue for UO_2) and CVD reactor materials capable of handling such temperatures, 2) the production of corrosive byproducts, requiring the use of high temperature corrosion-resistant materials, and 3) the pyrophoric nature of the freshly deposited Zr coatings (Sherman, 2006). An additional consideration will be the use of a surrogate material in place of the UO_2 kernel in the coating process development. Inherent differences in material density between the surrogate and actual UO_2 fuel kernel will likely require some degree of process adaptation when the coating processing conditions are finalized.

2.2.3 Pebble Fabrication

Pebbles for the PBMR and other similar pebble bed reactors are produced by hot pressing. The TRISO particles are mixed with an appropriate quantity of graphite powder, and the spheres are hot pressed in a die. After the fuel-bearing portion of the pebble is pressed, a 5 mm fuel-free layer of graphite is added by hot pressing graphite powder around the pebble in a larger die. Finally, the pressed sphere is heat treated at 1950°C for 9 hours to produce the desired properties in the pebble matrix and the fuel-free graphite coating on the exterior of the pebble. Figure 2.4 shows a schematic process flow for PBMR pebble fabrication (excluding the fuel-free graphite layer on the surface of the pebble).

A similar approach (although at lower temperatures) could be used to produce pebbles for the AFPR, even though PBMR pebbles are somewhat larger than the proposed AFPR pebbles (60 mm versus 10-15 mm). For Zr-matrix pebbles, Zr powder could be mixed with the Zr-coated fuel kernels and hot pressed in a die to the desired dimensions. The resulting pebble would likely have some porosity, and this would need to be characterized along with other microstructural features for prototypic dimensions and processing conditions. If ZrH_x -matrix pebbles are needed to provide extra moderation in the AFPR core, the hydriding likely would be performed after the pebbles were pressed. This approach has been used before when fabricating ZrH_x and other metallic hydrides for nuclear service (e.g. the nuclear airplane program during the 1960s – Mueller et al. 1968). The matrix integrity and dimensional distortion of the hydriding process would need to be characterized, as would the resulting microstructure of the matrix. The most likely candidate stoichiometry for the ZrH_x matrix is $x=1.6$, which produces the face-centered cubic δ -phase at projected AFPR operating temperatures (300-400°C). At these temperatures, the $ZrH_{1.6}$ should be thermodynamically stable, thereby suffering little hydrogen loss and not requiring hydrogen barrier coatings.

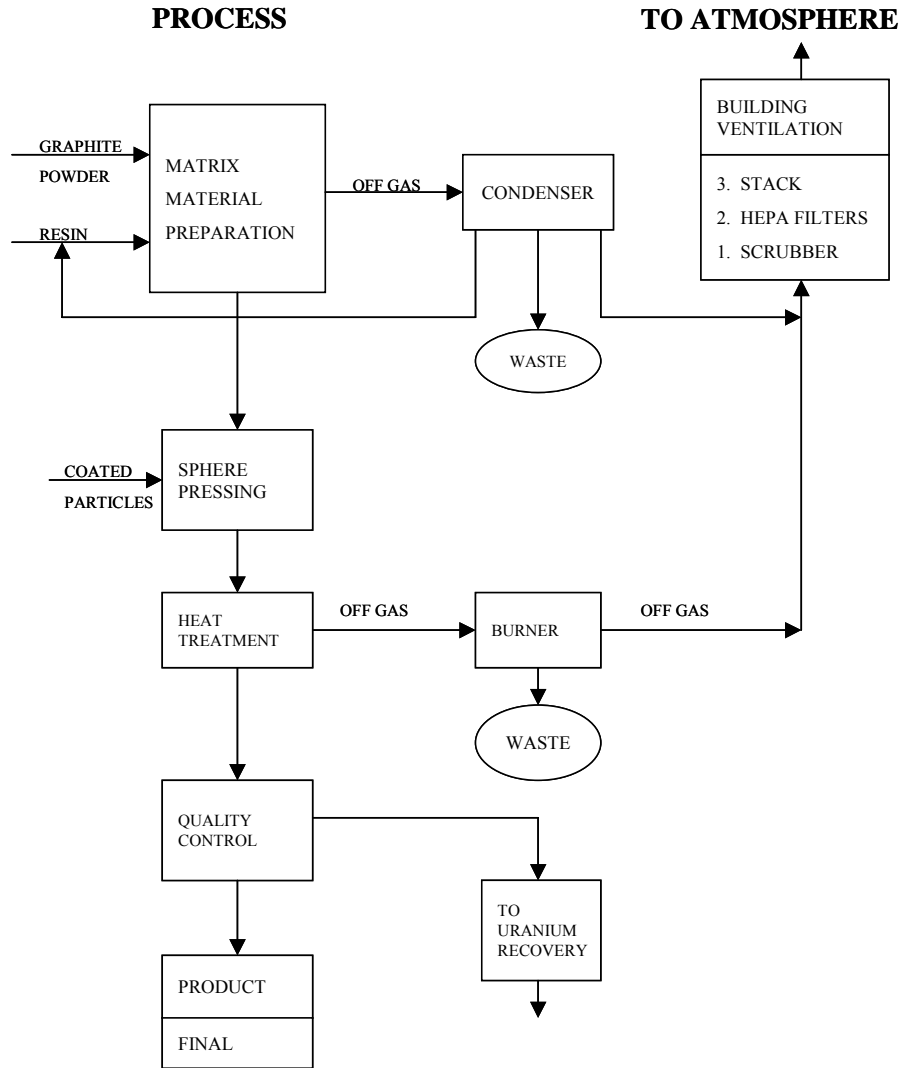


Figure 2.4. PBMR pebble manufacturing process.

2.2.4 Pebble Outer Coating

Regardless of which matrix material is used, the pebble will require an outer coating to serve as an additional fission product barrier and as a protective layer to protect the pebble and fuel kernels from the primary coolant. Although a Zr pebble matrix would be reasonably corrosion resistant in AFPR water conditions, the matrix will likely have some porosity. To prevent interaction between the primary coolant water and the fuel kernels, a protective coating will be required. If a ZrH_x material is used as the pebble matrix, a protective outer coating will be needed to prevent rapid corrosion of the matrix material itself. The thickness of the outer protective coating is therefore a function of its expected corrosion rate and the projected lifetime of the pebble in the primary coolant.

For maximum materials and coolant compatibility, a Zr or Zr alloy outer protective layer is the most desirable material. A thickness of 150-300 μm should provide up to 30 years of corrosion protection (ignoring the effects of defects) in 300°C liquid water, based on literature data for Zr corrosion rates (Fiero, 1987). Because of the thickness required for the outer coating layer, the CVD method proposed

for the kernel coating step is not a viable coating process. However, a low temperature spray process combined with a liquid phase sintering step to fully densify the resulting pebble coating will provide an acceptable approach to production of the outer protective layer (Fig. 2.5). Coatings will be applied to the pebbles in a fluidized or vibratory bed to ensure initial uniform coverage prior to the sintering step. This method offers many advantages for application of the outer coating, including the ability to apply thick and/or multiple layers of the coating material and the ability to produce intricate alloys by appropriate preparation of the spray suspension mixture.

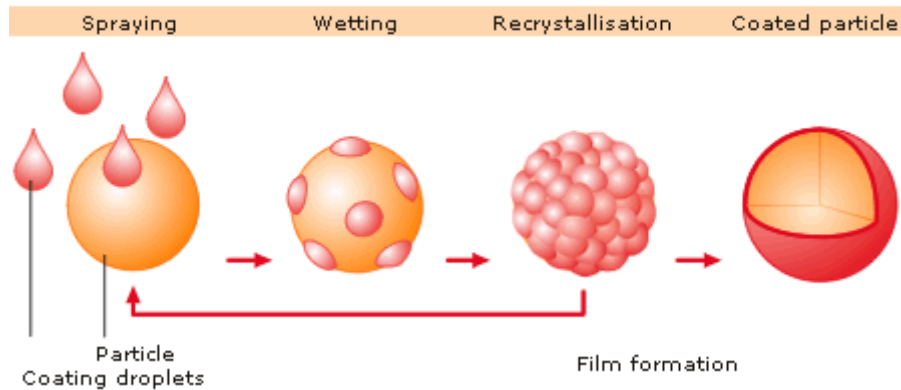


Figure 2.5. Stylized representation of the spray process proposed for applying an outer coating to the pebble. Note that for thicker coatings, multiple spray/recrystallization cycles may be required.

Potential issues related to the development of the spray coating process are primarily related to the selection of the proper sintering aids in the recrystallization/sintering part of the process. Careful consideration will need to be made to ensure minimal coating defect formation, optimization of the ductility/strength coating properties for the fuel application, and the potential for incorporation of minor components that may be detrimental in a nuclear application (Sherman, 2006).

2.3 Alternative Outer Coating Materials

Seven outer coating material candidates were exposed to conditions typical of a water cooled reactor in an autoclave to investigate their corrosion rates. The candidate materials included were CVD β -SiC, Y_2O_3 -stabilized ZrO_2 (YSZ), titanium foil (Ti), tungsten foil (W), molybdenum foil (Mo), vanadium (V), and V-4Cr-4Ti alloy in an as-rolled condition. No Zr or Zr-based alloys were included in the test because these materials are quite well characterized under AFPR-relevant water conditions. The V, V-base alloy, Ti, and YSZ were included in the experiment as possible alternatives to Zr or Zr-base alloys as the pebble outer coating. If it is later determined that the corrosion resistance of Zr or Zr-base alloys is inadequate, or there are problems with the deposition of Zr or Zr-base alloys as the outer protective coating, these are the most attractive alternative materials based on the earlier materials selection process as described in Section 2.1. Silicon carbide was included in the test due to general interest and lack of available literature data for corrosion in 300°C water, even though it is not being considered for an outer coating material because of its unacceptable low-temperature swelling behavior described in Geelhood et al. (2006).

The autoclave was operated at 1100 psi (7.5 MPa) with the following water chemistry:

- pH @ room temperature 5.2
- O_2 concentration ≤ 10 ppb (maintained by using 20 psig H_2 overpressure),
- Resistivity > 0.7 Mohm/cm
- Fluoride < 0.2 ppm
- Chloride < 0.3 ppm
- Nitrite < 0.7 ppm
- Nitrate < 1.0 ppm
- Phosphate < 3.0 ppm
- Sulfate < 3.0 ppm

The first set of samples (SiC, YSZ, Mo, W, and Ti) were exposed for 1011 hours at 288°C, removed, and examined. Further testing on selected samples (SiC, YSZ, Ti, V, V-4Cr-4Ti) was performed for 1826 hours at 300°C with the same water chemistry. All the samples in the second series of tests were new corrosion samples and none were continued from the first test due to the change in temperature.

The first test resulted in weight gains (losses) due to corrosion or due to specimen interaction since several pieces came into contact during the testing as shown in Table 2.1. After the first test both W and Mo were removed from the candidate test matrix as a result of their poor performance and V and V-4Cr-4Ti were added. The second test resulted in minor weight changes for all tested materials after 1826 hours at 300°C. The weight changes are listed in Table 2.2. Photographs of the as tested materials are provided in Figure 2.6.

Table 2.1. Weight Gain Data Associated from 1011 hours of Autoclave testing at 288°C

| Sample Material | Initial Weight (g) | Final Weight (g) | Change (g) | Visual Observations |
|------------------------|---------------------------|-------------------------|-------------------|--|
| Molybdenum#1 | 0.6406 | 0.5478 | -0.0928 | Severe Corrosion |
| Molybdenum#2 | 0.6413 | 0.5603 | -0.0810 | Severe Corrosion |
| Tungsten #1 | 35.6749 | 35.5052 | -0.16970 | Severe Corrosion |
| Tungsten #2 | 36.4264 | 36.3532 | -0.07320 | Severe Corrosion |
| CVD-SiC #1 | 7.0919 | 7.0921 | 0.0 | No change |
| CVD-SiC #2 | 7.0923 | 7.0923 | 0.0 | No change |
| Ti #1 | 1.2224 | 1.2254 | +0.0030 | Discoloration |
| Ti #2 | 1.2215 | 1.2249 | +0.00340 | Discoloration |
| YSZ #1 | 3.1690 | 3.1851 | +0.01610 | Discoloration (contact with other materials) |
| YSZ #2 | 1.0180 | 1.0203 | +0.00230 | Discoloration |

Table 2.2. Weight Gain Data Associated 1826 hours of Autoclave testing at 300°C

| Sample | Initial Weight (g) | Final Weight (g) | Change (g) | Visual Observations |
|--------------------------|---------------------------|-------------------------|-------------------|----------------------------|
| V-4Cr-4Ti (As Rolled) #1 | 2.6409 | 2.6409 | 0.0 | No change |
| V-4Cr-4Ti (AS Rolled) #2 | 2.5644 | 2.5644 | 0.0 | No change |
| V-1 | 1.8618 | 1.8621 | +0.0003 | No change |
| V-2 | 1.8579 | 1.8575 | -0.0004 | No change |
| CVD-SiC #3 | 7.0813 | 7.0813 | 0.0 | No change |
| CVD-SiC #4 | 7.0228 | 7.0228 | 0.0 | No change |
| Ti #3 | 1.3552 | 1.3575 | +0.0023 | Slight film |
| Ti #4 | 1.2496 | 1.2510 | +0.00140 | Slight film |
| YSZ #3 | 3.1001 | 3.1265 | +0.0264 | No change |
| YSZ #4 | 3.1369 | 3.1693 | +0.03240 | No change |

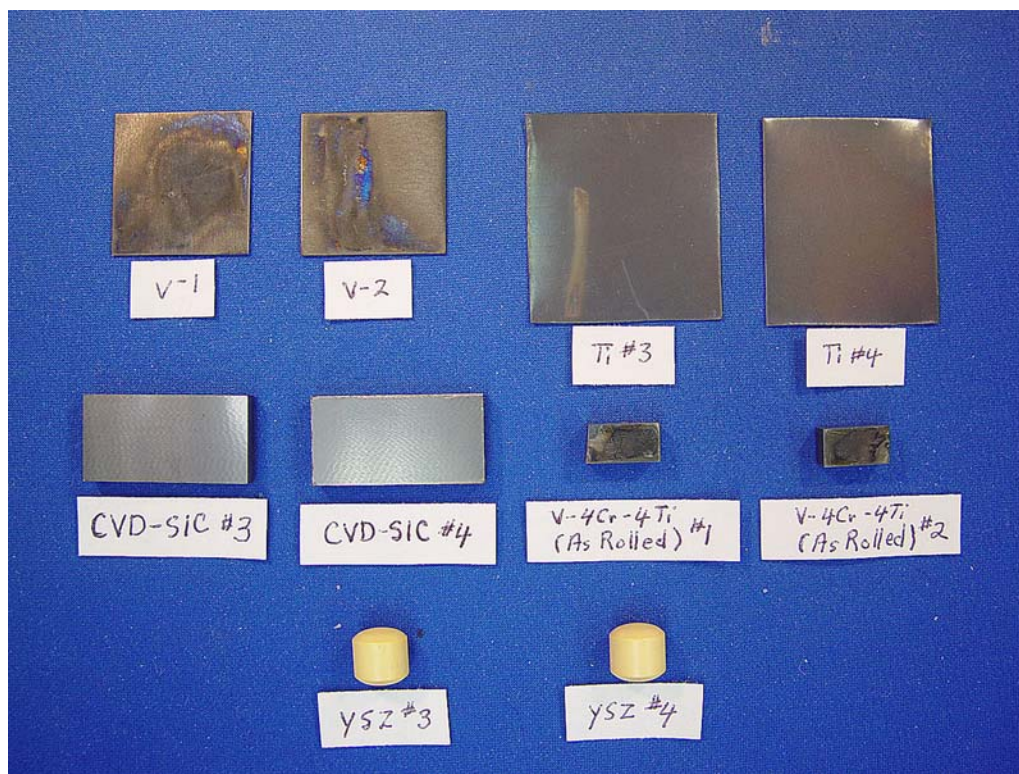


Figure 2.6. Photographs of samples after 1826 hours at 300°C. The metals are lightly corroded with oxide films but the ceramics are visually unaffected. However, the YSZ materials did exhibit weight gains.

3.0 Fuel Performance Modeling

Fuel and material property models associated with the spherical cermet fuel elements are presented in this section. Fuel swelling, growth, and fission gas release estimates are provided.

3.1.1 Uranium Dioxide (UO₂)

Performance models used to predict irradiation swelling and thermal-mechanical properties associated with the UO₂ kernels over the range of conditions described in Table 1.2 are summarized in this subsection. These models have been taken from the NRC fuel performance code FRAPCON-3 (Berna et al. 1997 and Lanning et al. 2005) and are well verified. In addition to the models, plots are provided showing the model predictions over the applicable ranges. The models provided in this section will be irradiation swelling, elastic modulus, thermal expansion strain, specific heat, thermal conductivity, and athermal fission gas release.

The theoretical density of UO₂ is 10.96 g/cm³. The density used in the equations given below is expressed as a percent of the theoretical density (T.D.).

Thermal Conductivity

The thermal conductivity of UO₂ is given in Equation 3.1 (Lanning et al. 2005). This model is a function of temperature and burnup and is valid between 293K and 1700K. This model has been validated up to a burnup of 62 GWd/MTU, but is expected to be valid up to 100 GWd/MTU. This model is for 95% T.D. fuel. The porosity correction is given in Equation 3.2 (Lanning et al. 2005) and can be used to adjust for different density.

$$K = \frac{1}{0.0452 + 2.46 \times 10^{-4} T + 0.00187 \cdot bu + (1 - 0.9 \exp(-0.04bu))(0.00187bu) \left(\frac{1}{1 + 396 \exp(-6380/T)} \right) + \frac{3.5 \times 10^9}{T^2} \exp(-16361/T)} \quad (3.1)$$

$$K_d = 1.0789 \cdot K_{95} \frac{d}{1 + 0.5(1 - d)} \quad (3.2)$$

where K = thermal conductivity, W/m-K
 T = temperature, K
 d = fraction of theoretical density.

Figure 3.1 shows the thermal conductivity for 95% T.D. fuel at various burnup levels.

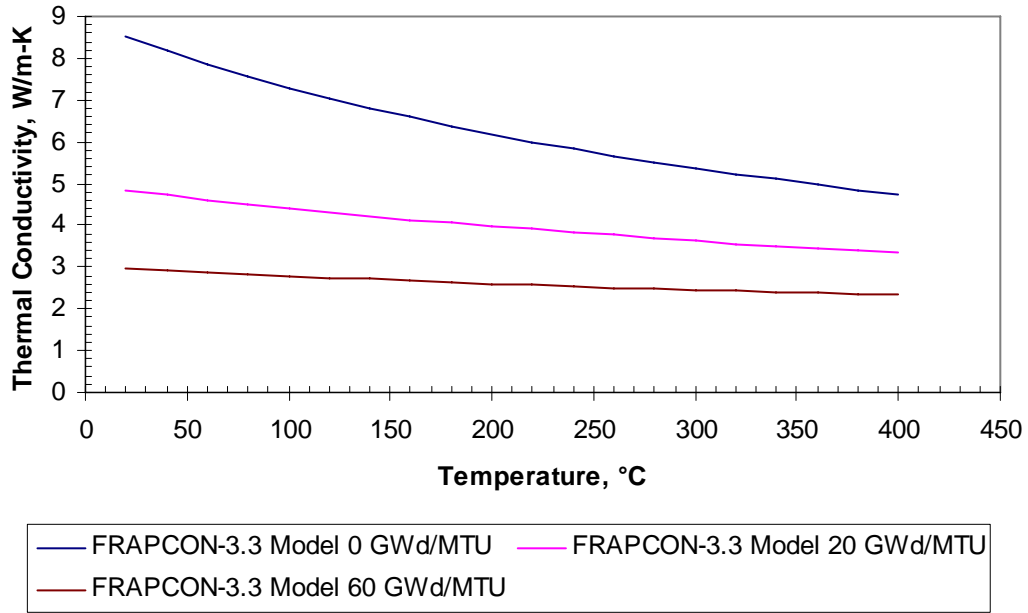


Figure 3.1. Thermal conductivity for 95% T.D. UO₂ fuel at various burnup levels

Specific Heat

The specific heat of UO₂ is given in Equation 3.3 (Berna et al. 1997). This model is a function of temperature and is valid between 293K and 1700K.

$$c_p = \frac{296.7 \cdot 535.285^2 \exp(535.285/T)}{T^2 (\exp(535.285/T) - 1)^2} + 2.43 \times 10^{-2} T + \frac{2.0 \cdot 8.745 \times 10^7 \cdot 1.577 \times 10^5}{2 \cdot 8.3143 \cdot T^2} \exp\left(\frac{-1.577 \times 10^5}{8.3143 \cdot T}\right) \quad (3.3)$$

where c_p = specific heat, J/kg-K
 T = temperature, K.

Figure 3.2 shows the specific heat for 95% T.D. fuel.

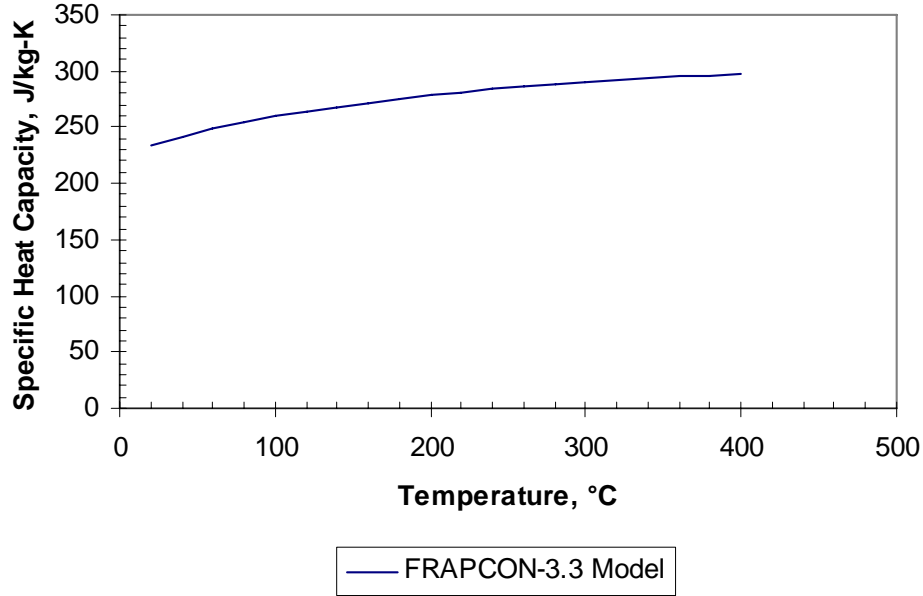


Figure 3.2. Specific heat for 95% T.D. UO₂ fuel.

Irradiation Swelling and Densification

The model for irradiation swelling in UO₂ is given in Equation 3.4 and Equation 3.5 (Lanning et al. 1997). This model is a function of fuel density and burnup. It has been validated up to a rod average burnup of 62 GWd/MTU, but is expected to be valid beyond 100 GWd/MTU. In addition, M. Kinoshita et al. (2004) found little temperature dependence in the range of 500°C to 1200°C; therefore, it would be reasonable to assume that there would be no temperature effect at 300°C. The model for UO₂ densification is given in Equation 3.6 (Berna et al. 1997). This model is a function of fuel density, burnup, and sintering temperature, and is valid for fuel temperature between 293K and 1000K.

Swelling

$$\frac{\Delta V}{V} = 0; \text{ burnup} < 6 \text{ GWd/MTU} \quad (3.4)$$

$$\frac{\Delta V}{V} = D \cdot (bu - 6) \cdot 8.0966 \times 10^{-4}; \text{ burnup} > 6 \text{ GWd/MTU} \quad (3.5)$$

where $\Delta V/V$ = volume change, fraction

bu = burnup, GWd/MTU

D = fraction of theoretical density

Densification

$$\frac{\Delta V}{V} = \left(\frac{\Delta L}{L_{\max}} + \exp(-3(bu + B)) + 2 \exp(-35(bu + B)) \right) \frac{3}{100} \quad (3.6)$$

where $\frac{\Delta L}{L_{\max}} = \frac{-22.2(100 - D \cdot 100)}{T_s - 1453}$

$\Delta V/V$ = volume change, fraction

Bu = burnup, GWd/MTU

D = fraction of theoretical density

T_s = Fuel sintering temperature, K (Typically $T_s=1873K$)

B = constant such that $\Delta V/V=0$ when $bu=0$.

Predicted UO_2 volume change as a function of burnup based on the above relationship can be seen in Figure 3.3 for a case with 95% T.D. fuel. It should be noted that these particles will likely be greater than 98% T.D. and most likely will exhibit no densification and swelling will begin at the rate seen below at beginning of life.

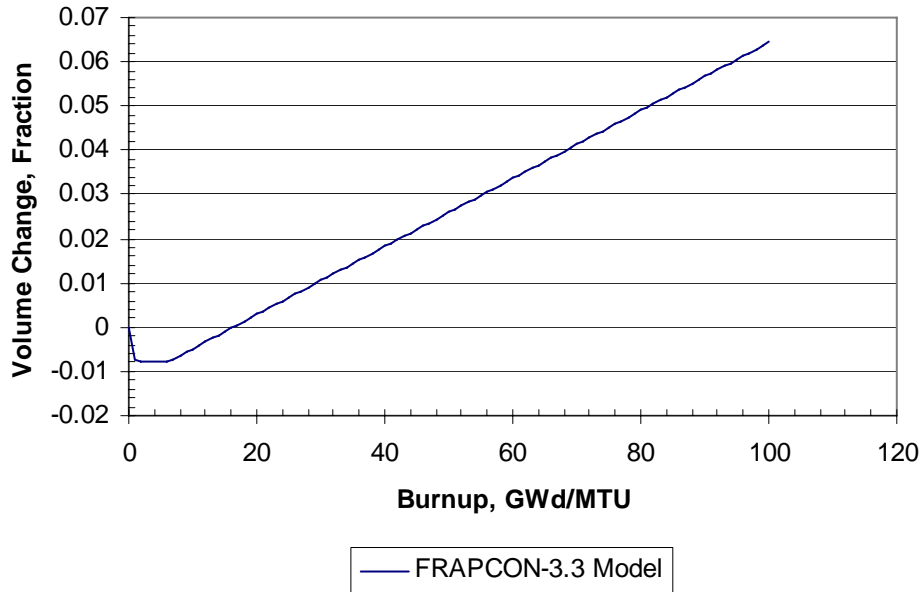


Figure 3.3. Fuel swelling and densification model predictions as a function of burnup for 95% T.D. fuel

Elastic Moduli

The Young's modulus, shear modulus and Poisson's ration for UO_2 are given in Equations 3.7–3.9, respectively (Berna et al. 1997). These models are valid from 293K to 1700K. These models do not change with fluence and are a function of temperature and density.

$$E = 2.334 \times 10^2 [1 - 2.752(1 - D)](1 - 1.0915 \times 10^{-4} T) \quad (3.7)$$

$$G = \frac{E}{2(1 + \nu)} \quad (3.8)$$

$$\nu = 0.316 \quad (3.9)$$

where E = Young's modulus, GPa
 G = shear modulus, GPa
 ν = Poisson's ratio
 T = temperature, K
 D = fraction of theoretical density

Figures 3.4 and 3.5 show the model predictions for Young's modulus and shear modulus of UO_2 as a function of temperature for the case with 95% T.D. fuel.

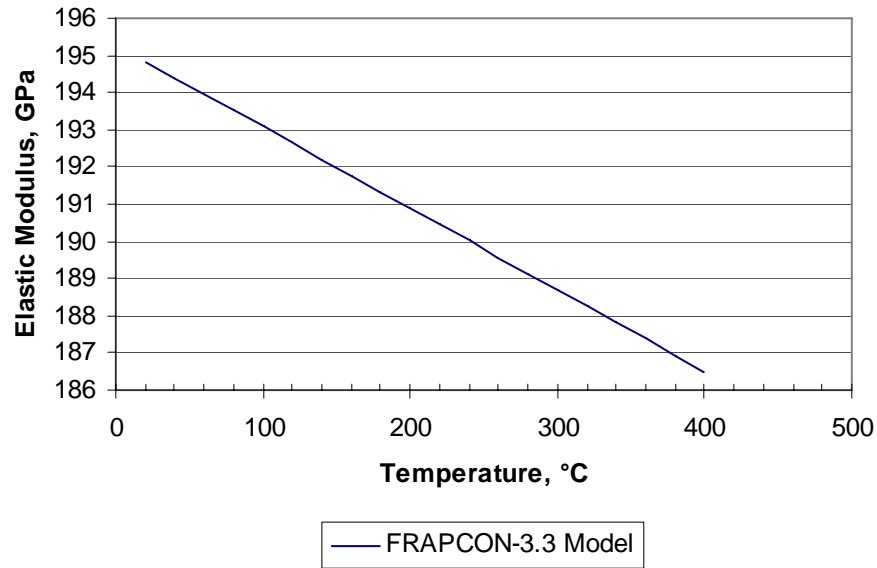


Figure 3.4. Young's modulus for UO_2 as a function of temperature for 95% T.D. fuel

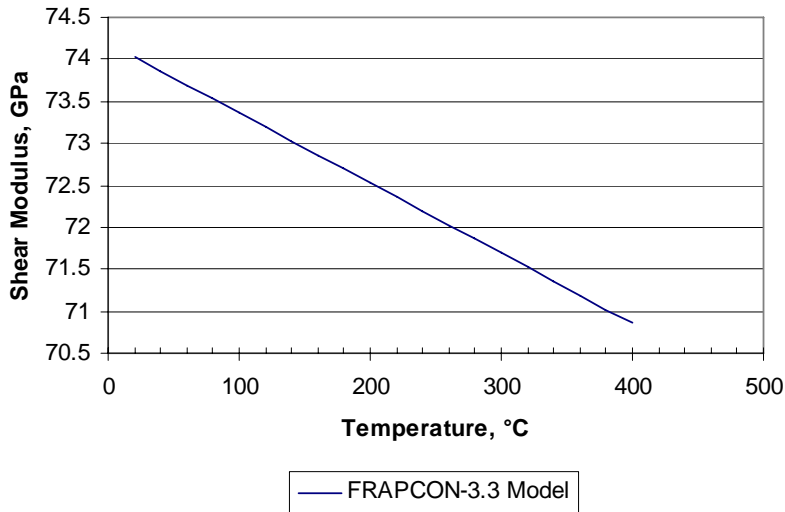


Figure 3.5. Shear modulus for UO_2 as a function of temperature for 95% T.D. fuel

Thermal Expansion Strain

The linear thermal expansion strain in UO_2 is given in Equation 3.10 (Berna et al, 1997). This model is a function of temperature and is valid between 293K and 1700K.

$$\varepsilon_{th} = 1.0 \times 10^{-5} T - 3.0 \times 10^{-3} + 4.0 \times 10^{-2} \exp\left(\frac{6.9 \times 10^{-20}}{1.38 \times 10^{-23} T}\right) \quad (3.10)$$

where ε_{th} = thermal expansion strain, in/in
 T = temperature, K

Figure 3.6 shows the thermal expansion strain for 95% T.D. fuel.

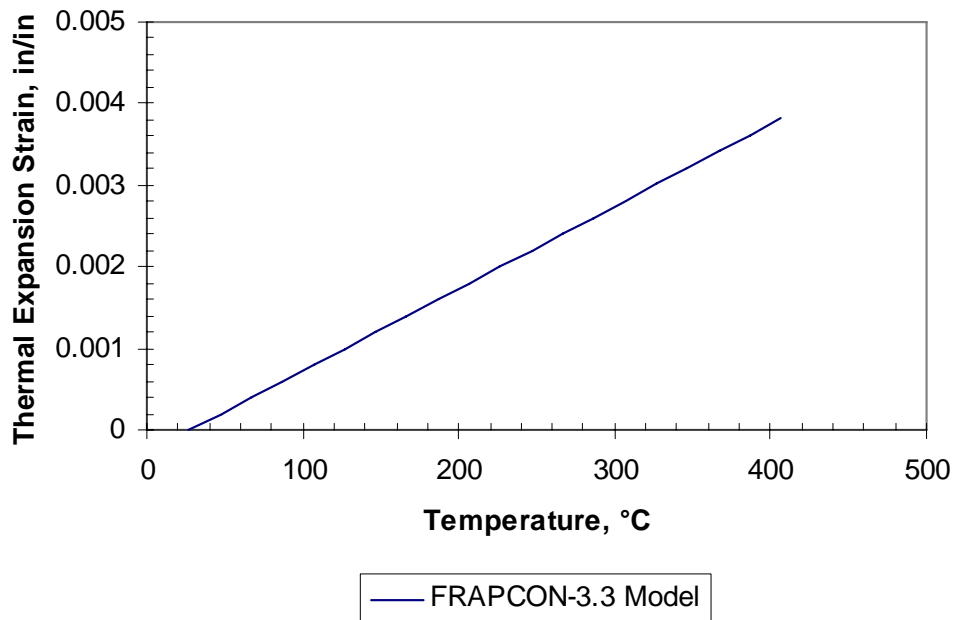


Figure 3.6. Thermal expansion strain for 95% T.D. UO_2 fuel

Athermal Fission Gas Release

The model for athermal fission gas release is given in Equation 3.11 (Berna et al, 1997). This model is a function of burnup and is valid up to a burnup of 62 GWd/MTU. However, it is expected to provide reasonable predictions of the athermal release up to 100 GWd/MTU. The athermal gas release is the xenon and krypton that is released from the UO_2 matrix by recoil and knockout. At temperatures below 400°C it is not expected that any gas will be released due to gas diffusion from the UO_2 matrix. The models provided here give fission gas release as a percent of the total gas produced. Equation 3.12 gives the gas produced as a function of burnup and density.

$$FGR = bu \cdot 7 \times 10^{-3} \quad (3.11)$$

where FGR = % fission gas released, of that produced
 bu = burnup, GWd/MTU.

$$G_{prod} = bu \cdot D \cdot 13.336 \quad (3.12)$$

where G_{prod} = gas atoms produced, moles/m³ UO₂
D = fraction of theoretical density.

Figure 3.7 shows the athermal fission gas release as a function of burnup.

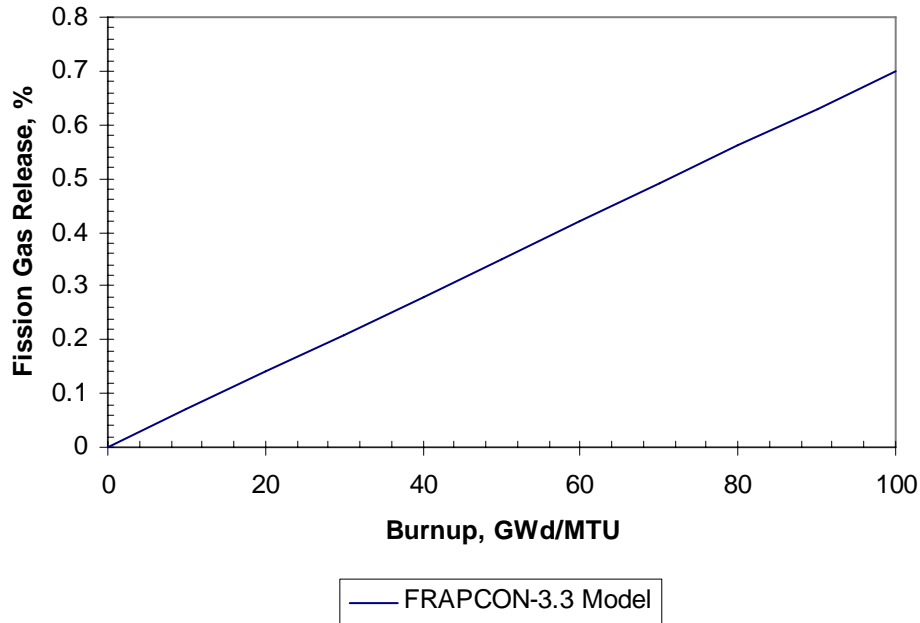


Figure 3.7. Athermal fission gas release model

3.1.2 Zirconium

The following section describes the thermal and mechanical properties of zirconium. Zirconium was selected as the prime candidate for the material to be used for both the matrix and the outer coating on the pebble. Zirconium has low cross section for neutrons and good dimensional stability in neutron flux. Typically alloys of zirconium (Zircaloy-2, Zircaloy-4, ZIRLO™ and M5™) are used in commercial reactors as the cladding for the fuel rods.

For this application, pure zirconium was selected. The primary reason to use one of the alloys mentioned above is to provide increased strength. It is not expected that strength will be a major issue for this fuel design. In addition, since these pebbles will likely be processed using various CVD methods, it may be significantly easier to use pure zirconium than an alloy with many alloying elements. An alloy may be considered for the outer coating material if improved corrosion resistance over pure zirconium can be obtained.

Thermal Conductivity

The thermal conductivity of zirconium is given in Equation 3.13. This model is a fit to data provided by Finnk and Leibowitz (1995) and Ho et al. (1972). This model is a function of temperature and is valid between 293K and 1000K.

$$k = -2.525 \times 10^{-8} T^3 + 7.0253 \times 10^{-5} T^2 - 5.5911 \times 10^{-2} T + 33.781 \quad (3.13)$$

where k = Thermal conductivity, W/m-K
 T = temperature, K.

Figure 3.8 shows the thermal conductivity for zirconium as a function of temperature.

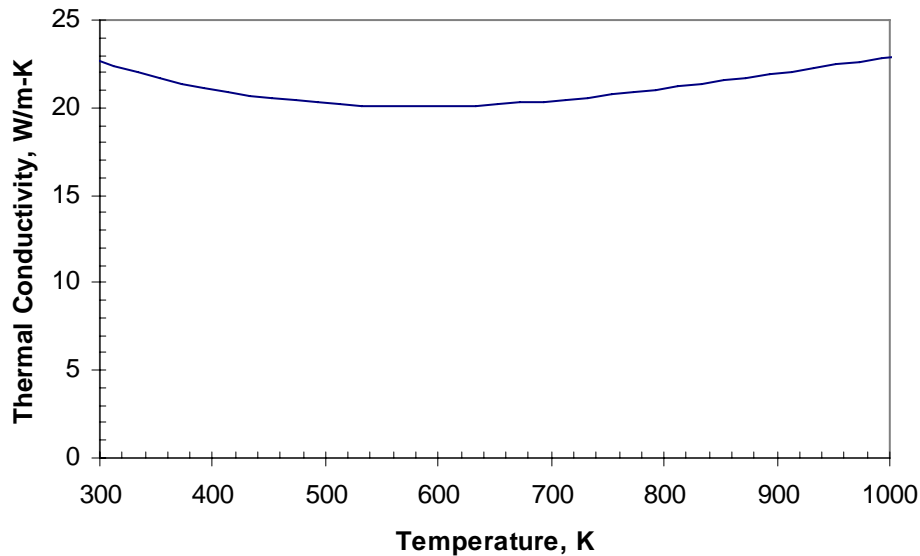


Figure 3.8. Thermal conductivity for zirconium.

Specific Heat

The specific heat of zirconium is given in Equation 3.14. This model is a fit to data provided by McBride et al. (1993). This model is a function of temperature and is valid between 293K and 1000K.

$$c_p = 0.0894 \cdot T + 247.34 \quad (3.14)$$

where c_p = specific heat, J/kg-K
 T = temperature, K

Figure 3.9 shows the specific heat for zirconium as a function of temperature.

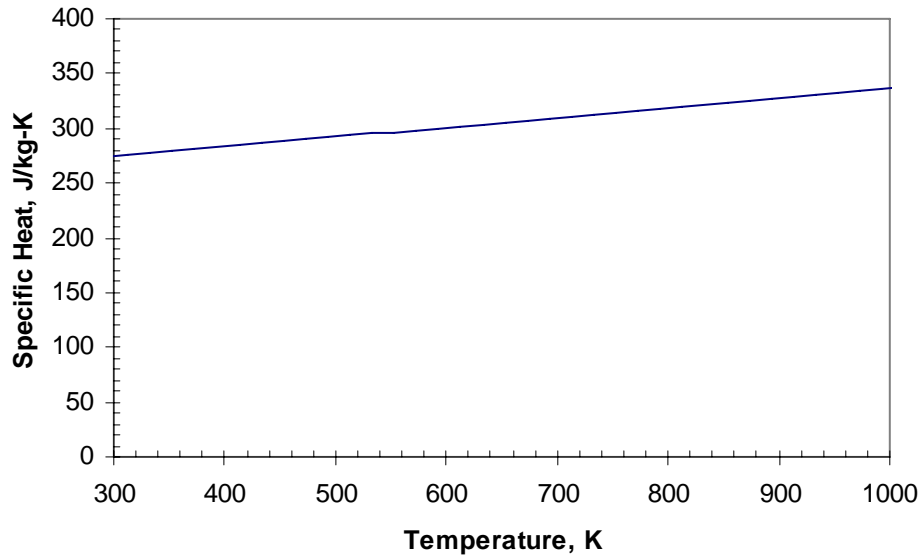


Figure 3.9. Specific heat for zirconium.

Density

The density of zirconium is 6,490 kg/m³ (6.49 g/cm³) (Sargent-Welch Scientific Company, 1979). This value will not change with burnup.

Irradiation Swelling and Densification

Zirconium and its alloys have been used for many years as cladding for nuclear fuel rods. Zirconium is chosen because it has a very low cross section of neutrons and is dimensionally stable in neutron flux. Zirconium will exhibit no dimensional changes due to irradiation swelling in AFPR.

Elastic Moduli

The Young's modulus of zirconium is given in Equation 3.15. This model is a fit to data provided by Armstrong (1964). This model is a function of temperature and is valid between 293K and 1000K. This model is valid for unirradiated, fully annealed zirconium. For Zircaloy, cold work will decrease Young's modulus and fast neutron fluence will increase Young's modulus (Hagrman et al. 1981). It is expected that the effect of cold work and fast neutron fluence on zirconium will be similar to Zircaloy. The adjustments from MATPRO (Hagrman et al 1981) for cold work and fast neutron fluence are shown in Equations 3.16 and 3.17. These may be applied for zirconium. The Young's modulus and the shear modulus can be related using Equation 3.18 given Poisson's ratio. For zirconium, Poisson's ratio is 0.34 (MatWeb, 2006).

$$E = 4.1524 \times 10^{-6} T^2 - 6.4149 \times 10^{-2} T + 1.1621 \times 10^{-2} \quad (3.15)$$

$$E = E_{annealed} - 26 \cdot CW \quad (3.16)$$

$$E_{irrad} = \frac{E_{unirrad}}{0.88 + 0.12 \exp(-\Phi / 10^{25})} \quad (3.17)$$

$$G = \frac{E}{2(1 + \nu)} \quad (3.18)$$

$$\nu = 0.34 \quad (3.19)$$

where E = Young's modulus, GPa
 CW = cold work, unitless ratio of areas
 Φ = fast neutron fluence, n/m²
 G = shear modulus, GPa
 ν = Poisson's ratio
 T = temperature, K.

Figures 4.10 and 4.11 shows the Young's Modulus and shear modulus, respectively, for zirconium as a function of temperature.

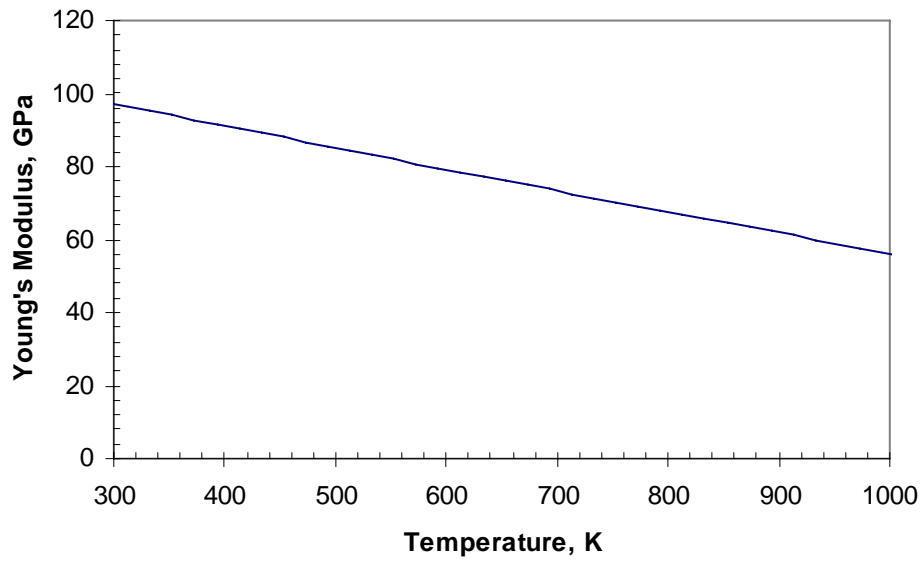


Figure 3.10. Young's modulus for unirradiator, fully annealed zirconium.

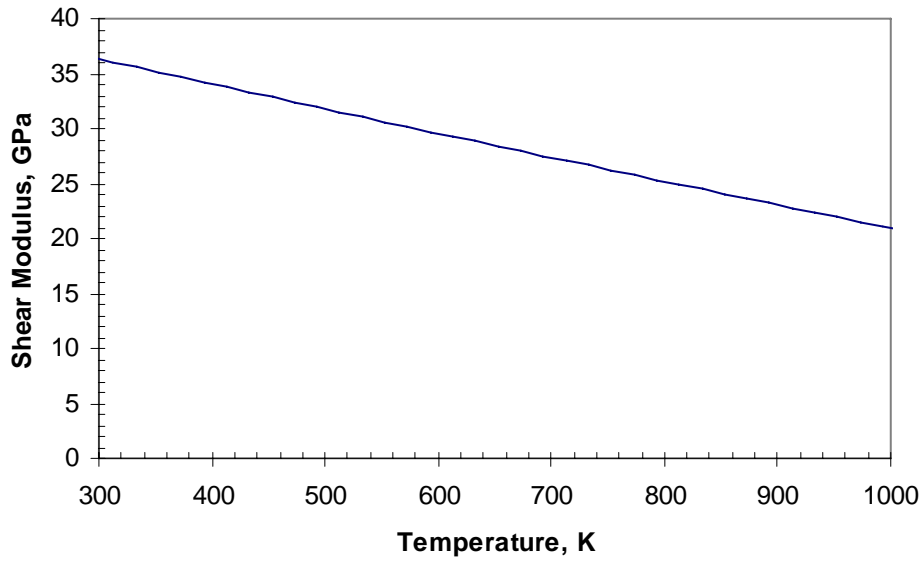


Figure 3.11. Shear modulus for unirradiated, fully annealed zirconium.

Thermal Expansion Strain

The thermal expansion strain of zirconium is given in Equation 3.20. This model is a fit to data provided by Petukhov (2004) and Erling (1939). This model is a function of temperature and is valid between 293K and 1000K.

$$\varepsilon_{th} = 1.4694 \times 10^{-9} T^2 + 4.9560 \times 10^{-6} T - 1.5682 \times 10^{-3} \quad (3.20)$$

where ε_{th} = thermal expansion strain, m/m

T = temperature, K.

Figure 3.12 shows the specific heat for zirconium as a function of temperature.

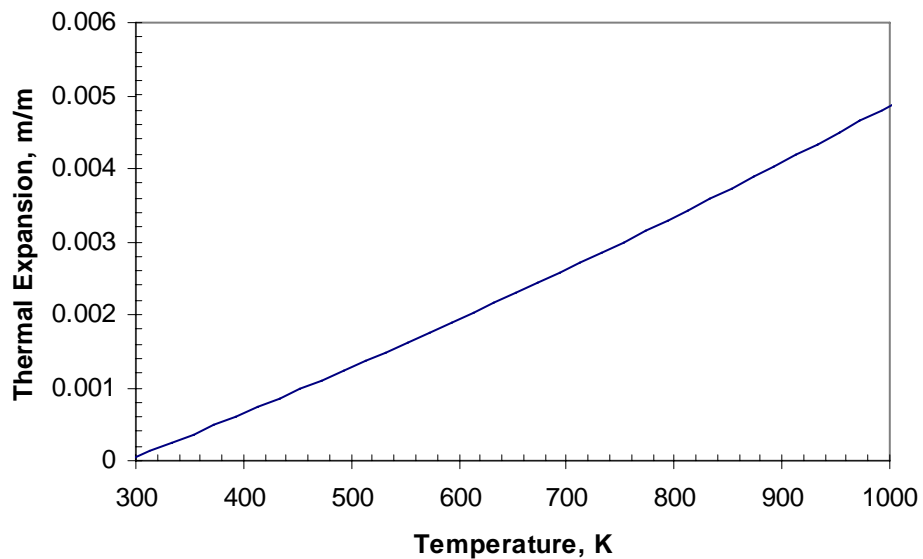


Figure 3.12. Thermal expansion strain for zirconium.

3.1.3 Zirconium Hydride (ZrH_{1.6})

The following section describes the thermal properties for zirconium hydride. This material was initially selected to provide extra moderation for the reactor because the initial fuel concept was under-moderated. However, the results of the neutronic analysis in Section 4 show that the extra moderation is not necessary to achieve the desired burnup levels. In addition, it will be shown in this section that the zirconium hydride provides small benefit to the thermal calculations.

It is well known that zirconium hydride is a very brittle material. From a mechanical point of view, it would not be desirable to fabricate these pebbles with a zirconium hydride matrix. Because of the severe limitations of zirconium hydride from a mechanical standpoint and the limited benefits from a thermal and neutronic standpoint, it is not likely that zirconium hydride will be used as a matrix material in the final design. Because of this, it will not be attempted to qualify the mechanical properties of zirconium hydride in this section, other than to state that this material is very brittle and has a fracture toughness value of less than 1 MPa-m^{1/2}.

Thermal Conductivity

The thermal conductivity of zirconium hydride can be calculated based on the diffusivity, specific heat and density. The equation that relates these properties is given in Equation 3.21.

$$k = \alpha \cdot c_p \cdot \rho \quad (3.21)$$

where k = Thermal conductivity, W/m-K

α = Thermal diffusivity, m²/s

c_p = specific heat, J/kg-K

ρ = density, kg/m³

The thermal diffusivity of zirconium hydride is a function of temperature and hydrogen content and is given by Equation 3.22 (Tsuchiya et al. 2002). The specific heat and density of zirconium hydride are given in the following sections.

$$\alpha = \left(\frac{67.9}{T + 1.62 \times 10^3 (2 - x) - 1.18 \times 10^2} - 1.16 \times 10^{-2} \right) \cdot 10^{-4} \quad (3.22)$$

Figure 3.13 shows a plot of the thermal conductivity of zirconium hydride as a function of temperature for various hydrogen concentrations.

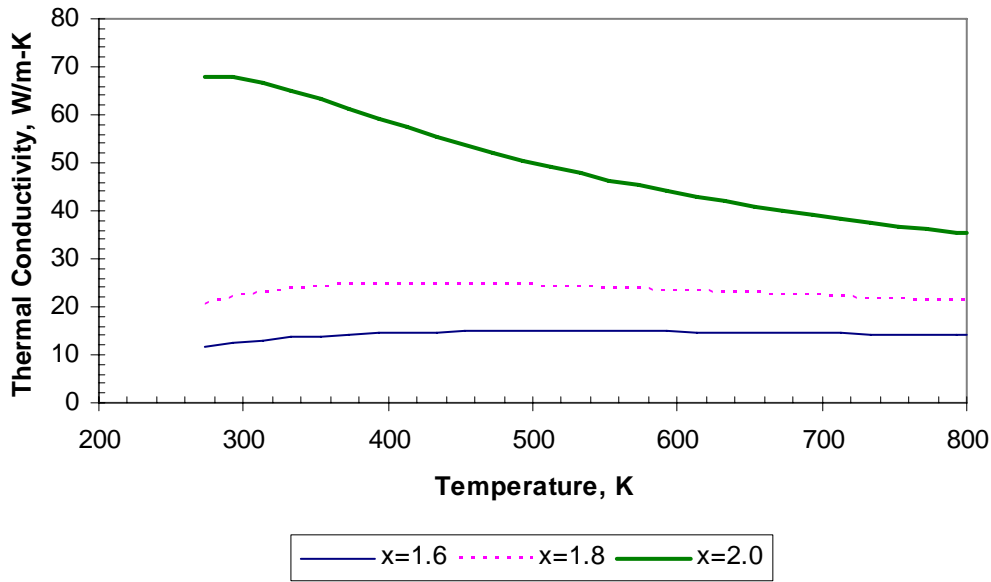


Figure 3.13. Thermal conductivity of ZrH_x for various hydrogen concentrations

Specific Heat

The specific heat of zirconium hydride is a function of temperature and hydrogen content. The specific heat is given by Equation 3.23 (Yamanaka et al. 1999).

$$c_p = [25.02 + 4.746 \cdot x + (3.103 \times 10^{-3} + 2.008 \times 10^{-2} \cdot x)T - (1.943 \times 10^5 + 6.358 \times 10^5 x) / T^2] / 93220 \quad (3.23)$$

where c_p = specific heat, J/kg-K
 x = ratio of H to Zr
 T = Temperature, K.

Figure 3.14 shows a plot of specific heat as a function of temperature for various hydrogen levels.

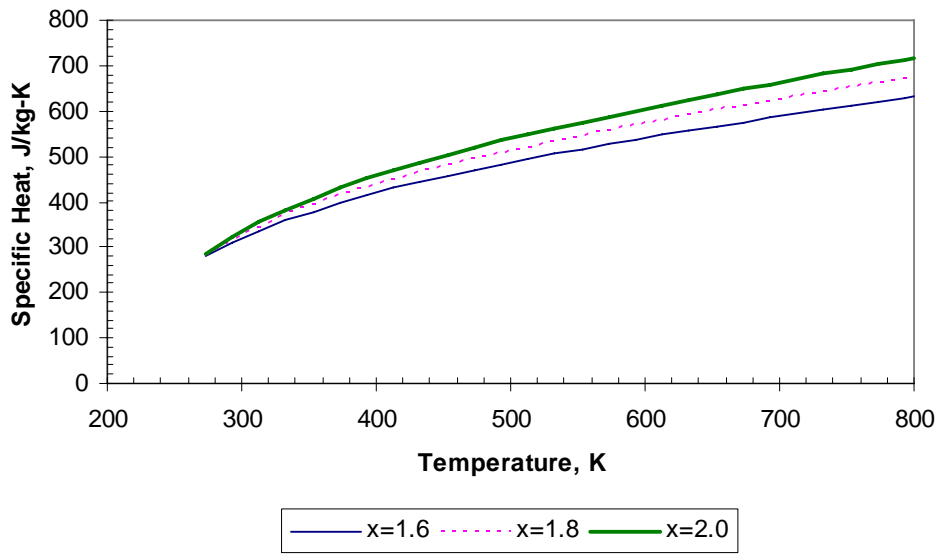


Figure 3.14. Specific heat of ZrH_x for various hydrogen concentrations

Density

The density of zirconium hydride is a function of the hydrogen content. The density is given by the Equations 3.24 and 3.25 (Simnad 1981).

$$\rho = \frac{1000}{0.1541 + 0.0145x}; 1 < x < 1.6 \quad (3.24)$$

$$\rho = \frac{1000}{0.1706 + 0.0042x}; 1.6 < x < 2 \quad (3.25)$$

where ρ = density of ZrH_x, kg/m³
 x = ratio of H to Zr.

Figure 3.15 shows a plot of the density of ZrH_x as a function of hydrogen content, x .

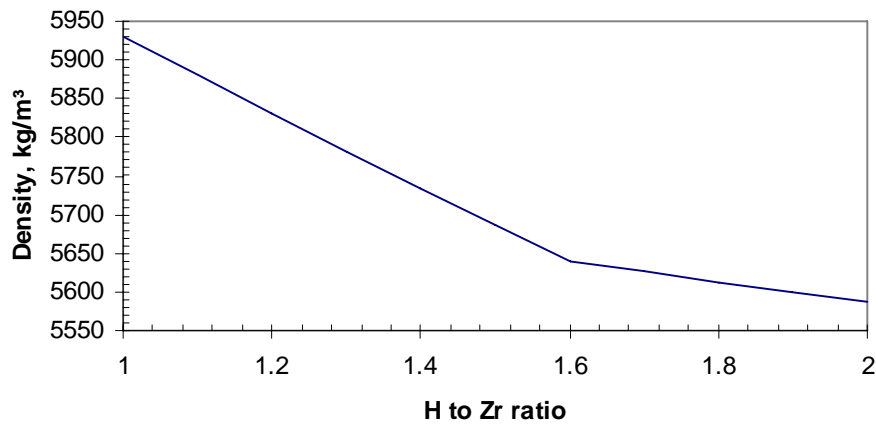


Figure 3.15. ZrH_x density as a function of hydrogen content

3.2 Spherical Cermet Fuel Effective Thermal Conductivity and Specific Heat

The Rayleigh derivation of effective thermal conductivity (Rayleigh, 1892) is used to determine the effective conductivity for the fuel kernels in the matrix. This equation is shown in Equation 3.26.

$$\frac{k_{eff}}{k_0} = 1 + \frac{3\phi}{\left(\frac{k_1 + 2k_0}{k_1 - k_0}\right) - \phi + 1.569\left(\frac{k_1 - k_0}{3k_1 - 4k_0}\right)\phi^{10/3}} \quad (3.26)$$

where k_{eff} = effective thermal conductivity of matrix containing fuel kernels

k_0 = thermal conductivity of fuel kernels

k_1 = thermal conductivity of matrix material

The Maxwell derivation of effective thermal conductivity (Maxwell, 1873) is used to determine the effective conductivity for the coated pebble. This equation is shown in Equation 3.27.

$$\frac{k_{eff}}{k_0} = 1 + \frac{3\phi}{\left(\frac{k_1 + 2k_0}{k_1 - k_0}\right) - \phi} \quad (3.27)$$

The effective specific heat for the spherical cermet fuel element is found by combining the specific heat for the individual materials based on their mass fraction in the pebble. This is acceptable since none of the materials are expected to form new compounds, so the overall heat capacity of the kernel should be the sum of its parts. Likewise, the density of the spherical cermet fuel element is found by combining the densities for the individual materials based on their volume fraction in the pebble. Table 3.1 shows the effective thermal conductivity, heat capacity, and density for a pebble with a zirconium and zirconium hydride matrix for normal operating conditions, and for accident conditions. The effective thermal conductivity of the spherical cermet material (16 W/m-K at 300°C with Zr matrix) compares very favorably to the thermal conductivity of traditional UO₂ pellets used in commercial LWRs (approximately 2-3 W/m-K at LWR operating temperatures).

Table 3.1. Effective thermal properties for Spherical Cermet Fuel Element at normal and accident conditions.

| Property | Normal Conditions, 300°C | | Accident Conditions, 600°C | |
|----------------------|--------------------------|--------------------------|----------------------------|--------------------------|
| | Zirconium Matrix | Zirconium Hydride Matrix | Zirconium Matrix | Zirconium Hydride Matrix |
| Thermal Conductivity | 15.6 W/m-K | 28.2 W/m-K | 16.1 W/m-K | 21.9 W/m-K |
| Specific Heat | 296 J/kg-K | 431 J/kg-K | 320 J/kg-K | 520 J/kg-K |
| Density | 7470 kg/m ³ | 6940 kg/m ³ | 7470 kg/m ³ | 6940 kg/m ³ |

3.3 Spherical Cermet Fuel Transient Thermal Analysis

Understanding the temperature transient response time associated with nuclear fuel as a result of postulated reactivity insertion accidents, potential loss of coolant accidents, loss of flow conditions, or other transient conditions is important in designing fuel that is inherently safe. The time it takes for fuel to reach steady state temperature from a cold start if the neutron flux is suddenly raised, the time it takes to reach fuel melting temperatures after a complete loss of coolant accident, and the time it takes for the coolant to reach equilibrium temperatures when the fuel temperature is suddenly raised are equally important to understanding the behavior of a reactor. Time constants associated with the thermal response time of a fuel element should be kept low—on the order of 0.1 to 1 s—to ensure an inherently safe fuel design.

A scoping parametric study was performed to identify the upper limit on pebble diameter for Zr and $ZrH_{1.6}$ matrices using the models described in Section 3.1 and the techniques described in Section 3.2. The limiting factor in determining maximum pebble size was taken to be the thermal time constant. The goal was to keep the time constant below 1 s. The scoping parametric study considered only normal operating coolant temperatures of 300°C, a 500 μm diameter kernel that is consistent with TRISO fuel manufacturing practice, a 0.3 kernel packing fraction that is consistent with past cermet fuel practice, a 300 μm outer Zr coating, and the upper limit of 20% enrichment. Figures 3.16 and 3.17 show the results of this preliminary effort for the pebble time constant and pebble ΔT , respectively. The results indicated that a maximum pebble diameter of 10 mm for the Zr matrix and 15 mm for the $ZrH_{1.6}$ matrix would achieve time constants less than 1 s and peak fuel temperatures less than 350°C. These values were taken as the reference pebble dimensions for more detailed assessments of the time constant under both normal and accident conditions.

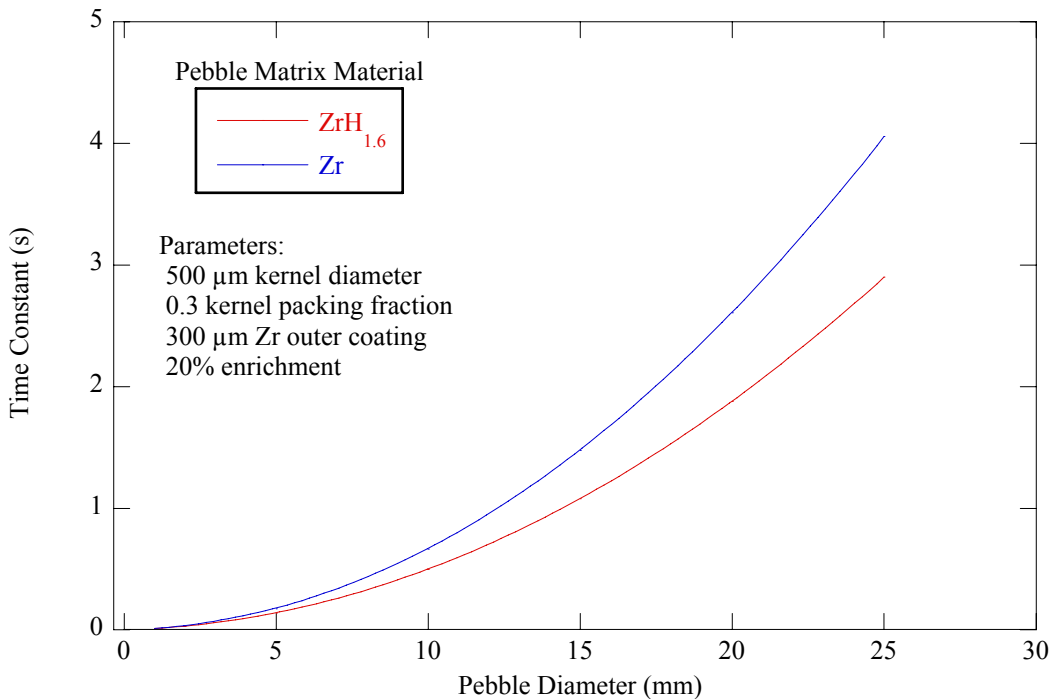


Figure 3.16. Dependence of Pebble Time Constant on Pebble Diameter for Zr and $ZrH_{1.6}$ Pebble Matrices

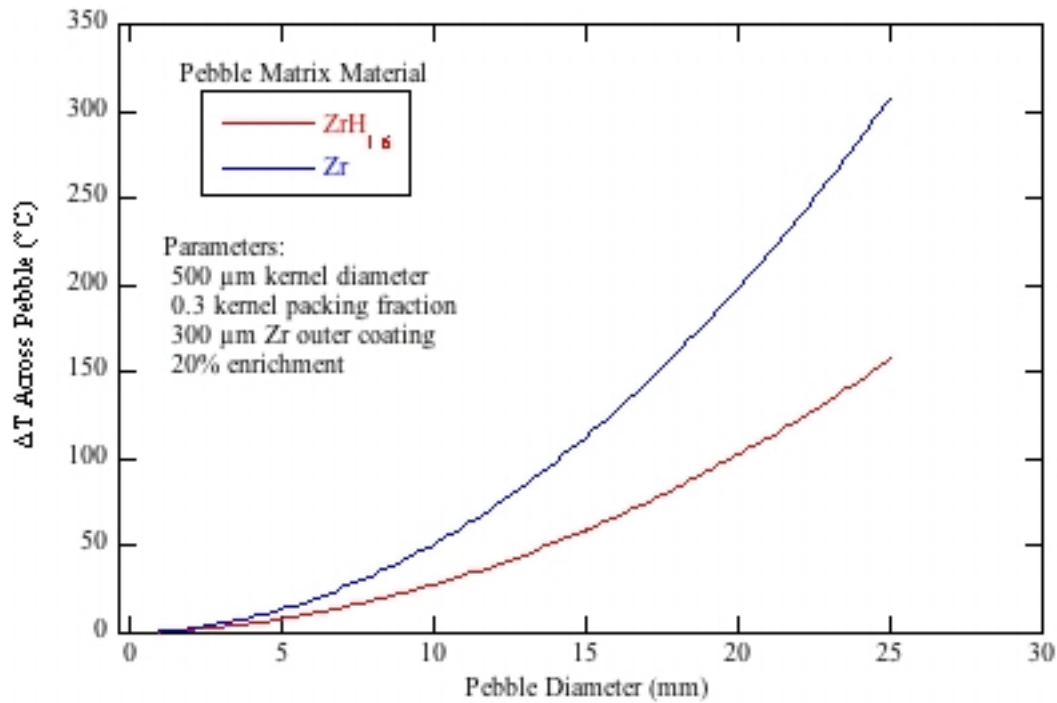


Figure 3.17. Dependence of Pebble ΔT on Pebble Diameter for Zr and ZrH_{1.6} Pebble Matrices

Two time constants can be calculated for the spherical cermet fuel concept. The first is a measure of how long it will take heat to leave the fuel element (Carslaw 1959). The second is a measure of how long it will take heat to be conducted out of the fuel element and into the coolant (El-Wakil 1978). Both of these time constants must be calculated and the larger of the two should be adopted as the time constant for the fuel element. Table 3.2 shows these time constants and the more limiting time constant for the normal and accident conditions for a zirconium matrix and a zirconium hydride matrix. It can be seen from this table that for both materials at normal and accident conditions, the time constant is less than 1 s.

Table 3.2. Time constants for Spherical CERMET Fuel Element at normal and accident conditions

| | Normal Conditions, 300°C | | Accident Conditions, 600°C | |
|-------------------------|--------------------------|--------------------------|----------------------------|--------------------------|
| | Zirconium Matrix | Zirconium Hydride Matrix | Zirconium Matrix | Zirconium Hydride Matrix |
| t1 (heat out of pebble) | 0.52 s | 0.39 s | 0.55 s | 0.61 |
| t2 (heat to coolant) | 0.24 s | 0.32 s | 0.26 s | 0.39 s |
| Limiting constant | 0.52 s | 0.39 s | 0.55 s | 0.61 s |

Using the effective thermal properties for the fuel element and assuming the heat production in the fuel is uniform, the center temperature was calculated for the spherical CERMET fuel elements. Table 3.3 shows these center temperature values for both normal and accident conditions for a zirconium matrix and a zirconium hydride matrix.

Table 3.3. Peak Center Temperatures for Spherical CERMET Fuel Element during normal and accident conditions

| | Normal Conditions, 300°C | | Accident Conditions, 600°C | |
|--------------------------------|---------------------------------|---------------------------------|-----------------------------------|---------------------------------|
| | Zirconium Matrix | Zirconium Hydride Matrix | Zirconium Matrix | Zirconium Hydride Matrix |
| ΔT (Coolant to Center) | 29.2°C | 20.2°C | 28.5°C | 23.3°C |
| Center Temperature | 329.2°C | 320.2°C | 628.5°C | 623.3°C |

The results indicate that the fuel will indeed have a fast thermal response time during temperature transients. This translates into a reactor which will be more passively safe than existing LWRs which have thermal response times on the order of 20 seconds, normal centerline temperatures on the order of 1,500°C, peak fuel temperatures on the order of 2,100°C during Anticipated Operational Occurrences, and can reach fuel melting temperatures (2,840°C) during a loss of coolant accident. In fact, it is apparent from the results in Tables 3.2 and 3.3 that the maximum pebble dimensions determined during the scoping parametric study are in fact conservative, and could be increased to simplify fuel manufacturing and fuel handling, if desired.

4.0 Neutronics Analysis

The primary objective of the neutronics analysis was to determine the feasibility of the new spherical cermet fuel element as it relates to AFPR reactor physics performance parameters. New analyses were needed because the current concept of zirconium metal matrix fuel pebbles with subcooled water coolant is significantly different from the previous AFPR physics studies with the SiC coated micro-fuel elements and two-phase coolant flow (Tsiklauri et al. 2005).

The assessment of reactor physics parameters is necessarily an iterative process since the physics parameters, thermal-hydraulics parameters, and fuel element materials properties are all interrelated. The approach taken for this study was to first perform some initial parametric studies, followed by more detailed analysis of reference core configurations, and then an evaluation of the impact of a few key variations of core parameters on the reference cases. The parametric studies fed into the preliminary choice of fuel properties for the reference cases, such as fuel pebble matrix material, fuel enrichment, fuel kernel packing fraction, and fuel pebble size. Preliminary choices of basic core parameters such as core size, geometry, configuration, power level, etc., were also made. The results of the parametric studies were used to define two reference cases with different fuel pebble matrix materials, zirconium and zirconium hydride. These reference cases were then evaluated in terms of the reactor physics performance of core lifetime, burnup reactivity, power distributions, and spent fuel isotopic composition. Several reactivity coefficients related to safety performance were also evaluated. Finally, the effect of selected variations in core parameters on the core physics parameters were evaluated, including the use of burnable poisons, adding radial reflectors, increasing core size, adding enrichment zoning, and adding moderator rods.

4.1 AFPR Core Specifications for Analysis

Table 4.1 summarizes the AFPR reactor core parameters that were specified as the initial conditions or assumptions for the physics analysis. The basic envelope of core power and volume was kept the same as the previous micro-fuel element study. The major difference from the previous study (other than the fuel form) was the uniform coolant density with no in-core boiling.

Table 4.1. AFPR Core Specifications

| Core Parameter | Value |
|---------------------------------|------------------|
| Thermal Power, MW _t | 300 |
| Core Height, m | 3.00 |
| Core Diameter, m | 3.06 |
| Core Volume, m ³ | 21.1 |
| Pebble Bed Porosity | 0.35 |
| Fuel Zones | 4 |
| Control Rods, number | 128 |
| Control Rods, material | B ₄ C |
| Coolant | water |
| Average Coolant Temperature, °C | 266 |
| Average Coolant Density, g/cc | 0.774 |

4.2 Methods

The Monte Carlo N-Particle code MCNP5 was used for static three-dimensional analysis of the reactor physics parameters. A full three-dimensional model of the reactor core was constructed with explicit treatment of the heterogeneous nature of the pebble fuel with dispersed fuel kernels and an outer buffer coating. The fuel pebbles were modeled as close-packed array using the lattice features of MCNP5. The overall core dimensions were derived from previous studies with the micro-fuel element concept. This model allowed easy variation of the materials and dimensions of the fuel and core. The MONTEBURNS code was used to couple MCNP5 with the ORIGEN2 burnup-depletion code to allow burnup calculations. The WIMS8 code was also used for core physics analyses and the evaluation of reactivity coefficients. A comparison of the WIMS8 and MCNP5 outputs showed agreement within 1% on keff for the base case. Figure 4.1 shows a cross section of the MCNP reactor core model. The fuel pebbles and fuel kernels are not shown in this figure for clarity. A 1/8th core slice was used since the core has azimuthal symmetry. Four fuel regions are separated by steel partitions. Each fuel region was divided into four subsections, allowing separate fuel compositions in each of the different fuel regions. Power and burnup in each of the sixteen radial fuel regions were tracked over the core life. Control rods were included in four radial fuel regions based on previous micro-fuel studies, but they were modeled as fully withdrawn so that the control rod channels (5.2 cm inner diameter) were filled with coolant water. Extra moderator channels in the previous micro-fuel study were removed. A 5 cm thick steel reactor vessel surrounded the core. Table 4.1 shows the radial dimensions of the different regions in the model.

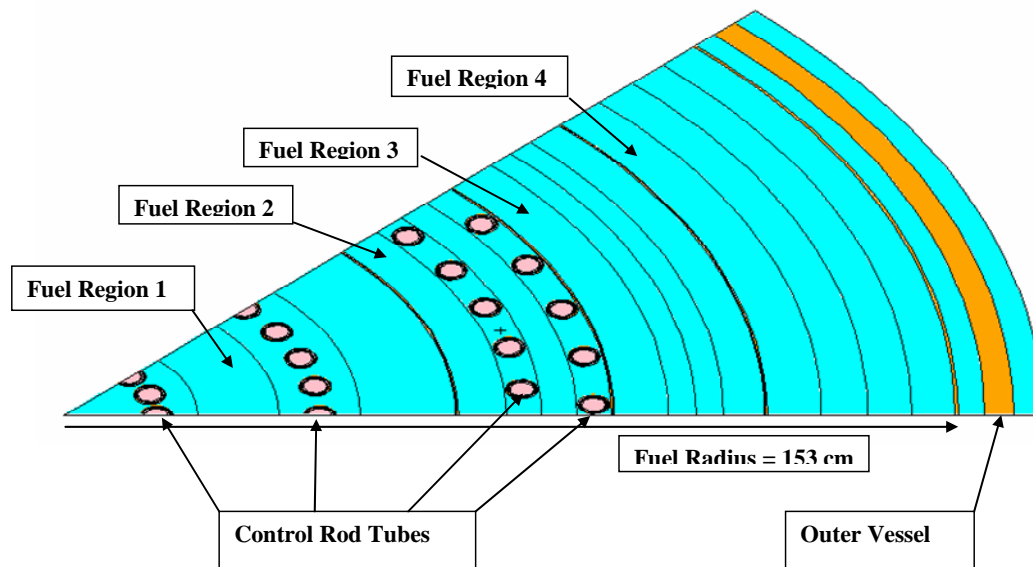


Figure 4.1. AFPR 1/8th Core Model Horizontal Slice

Table 4.2. AFPR Core Model Radial Dimensions

| Region | Outer Radius (cm) |
|---------------|--------------------------|
| fuel 1-1 | 23.00 |
| fuel 1-2 | 37.00 |
| fuel 1-3 | 51.00 |
| fuel 1-4 | 67.25 |
| wall | 67.75 |
| fuel 2-1 | 76.00 |
| fuel 2-2 | 82.00 |
| fuel 2-3 | 88.00 |
| fuel 2-4 | 94.00 |
| wall | 94.50 |
| fuel 3-1 | 103.75 |
| fuel 3-2 | 108.50 |
| fuel 3-3 | 113.25 |
| fuel 3-4 | 120.25 |
| wall | 120.75 |
| fuel 4-1 | 130.00 |
| fuel 4-2 | 138.00 |
| fuel 4-3 | 145.50 |
| fuel 4-4 | 153.00 |
| wall | 153.50 |
| water | 158.00 |
| wall | 163.00 |
| water | 168.00 |

4.3 Parametric Studies

As mentioned in the fuel fabrication section, the proposed spherical cermet fuel element design has a number of parameters that may be varied, including fuel enrichment, fuel kernel size, pebble size, matrix type, and kernel packing fraction. A number of calculations for beginning of life conditions were made to determine the sensitivity of k_{eff} to variations in these parameters.

Figure 4.2 shows the effect on k_{eff} of varying the kernel packing fraction and enrichment, and also shows the difference in Zr and $ZrH_{1.6}$ matrix materials. Figure 4.3 shows the effect of varying the pebble size and enrichment. Figure 4.4 shows the effect of varying the kernel size and enrichment. Most of these calculations were fairly short runs so that the uncertainty on the calculated k_{eff} would be on the order of 2%. The conclusions from these sensitivity studies were that

- Beginning of life (BOL) k_{eff} is not very sensitive to kernel packing fraction, kernel size, or pebble size
- Adequate initial reactivity could be attained with either Zr or $ZrH_{1.6}$ matrix
- $ZrH_{1.6}$ adds approximately 0.1 in k_{eff} compared to Zr for the same enrichment.

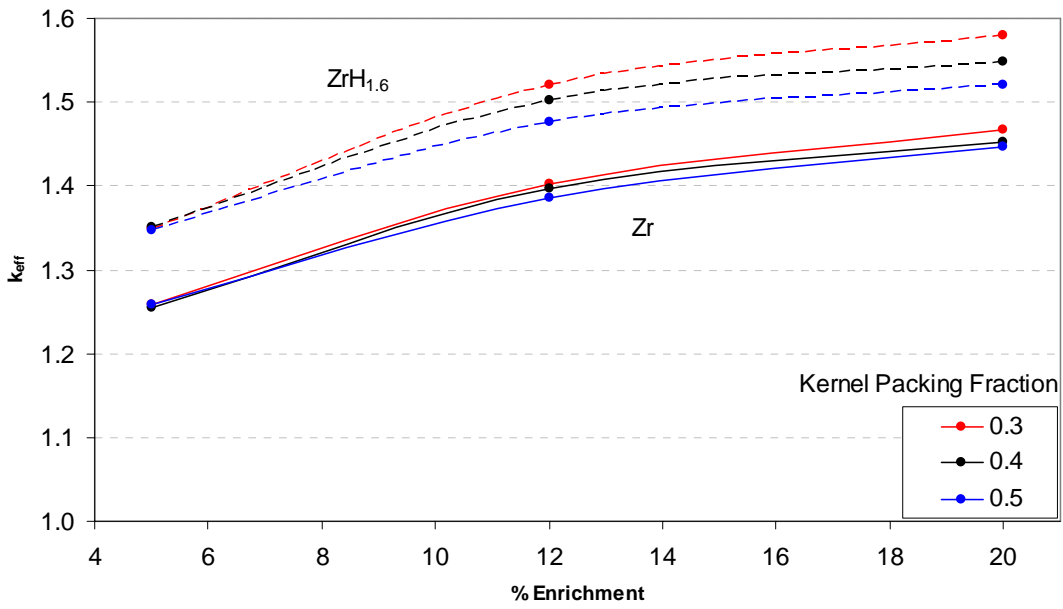


Figure 4.2. Variation of kernel packing fraction with Zr and $ZrH_{1.6}$ matrix

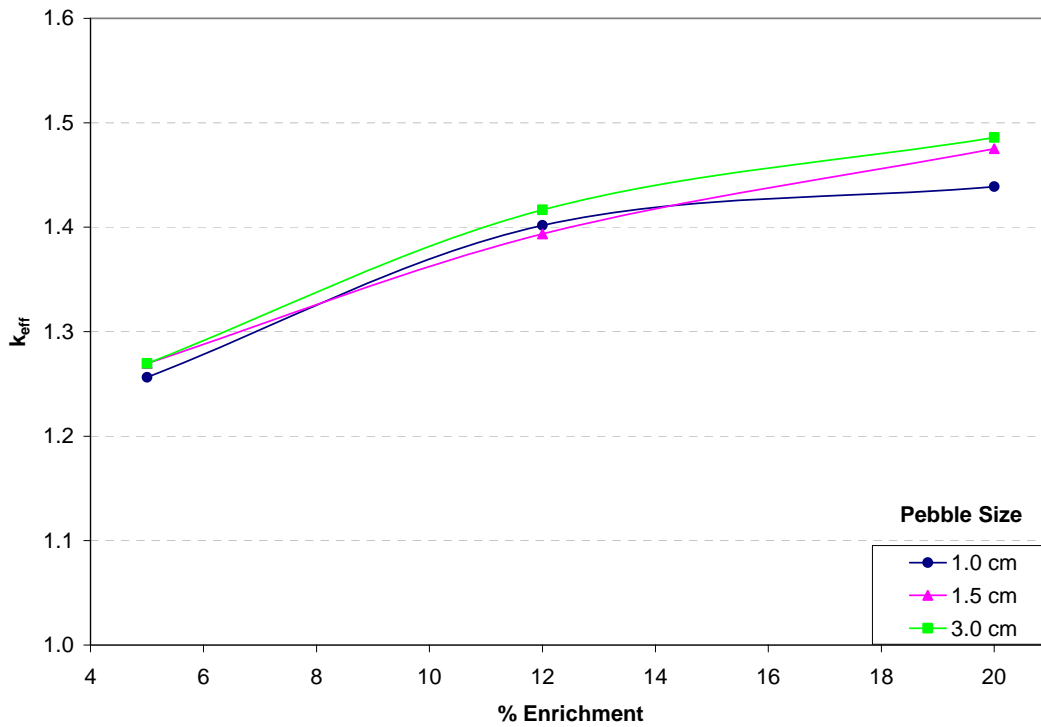


Figure 4.3. Variation of pebble diameter for Zr matrix

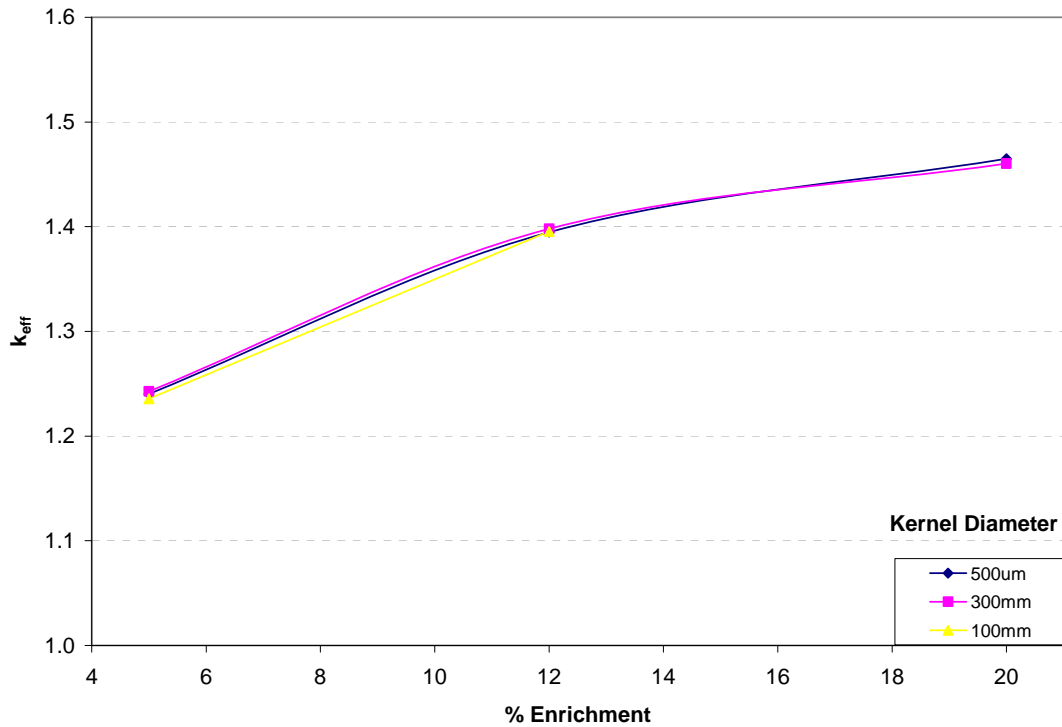


Figure 4.4. Variation of fuel kernel diameter for Zr matrix

The parameters shown in Table 4.3 were fixed for the subsequent burnup analyses. Both Zr and ZrH_{1.6} matrix cores were selected for further analysis.

Table 4.3 Fuel Parameters Selected for Burnup Analysis

| Fuel Parameter | Value |
|---|-------------------|
| Fuel Kernel diameter | 500 μm |
| Pebble diameter | 10 mm |
| Fuel kernel packing fraction | 0.3 |
| ²³⁵ U Enrichment for Zr matrix | 12% |
| ²³⁵ U Enrichment for ZrH _{1.6} matrix | 9% |

4.4 Analysis of Zr Base Case

4.4.1 Description

Based on the parametric studies, a Zr matrix base case configuration was defined for additional burnup analyses. The specifications for this case are shown in Table 4.4.

Table 4.4. Fuel Specifications for Zr base case

| Fuel Parameter | Value |
|--|-----------------|
| Pebble Matrix Material | Zr |
| Pebble Coating Material | Zr |
| Fuel Kernel Material | UO ₂ |
| Fuel Kernel Density, g/cm ³ | 10.7 |
| Kernel Packing Fraction | 0.3 |
| Pebble Coating Thickness, cm | 0.03 |
| Kernel Diameter, μm | 500 |
| Pebble Diameter, mm | 10 |
| Enrichment, % | 12 |
| UO ₂ mass, Mt | 36.1 |

4.4.2 Burnup Analysis

The MCNP5, ORIGEN2, and MONTEBURNS codes were used to model the irradiation of the Zr base case core at a full power of 300 MWt for 20 years. The control rods were fully withdrawn and no burnable poisons were used.

4.4.2.1 Burnup Reactivity Loss

Figure 4.5 shows the change in k_{eff} due to the reactivity loss related to burnup for this case. The fresh fuel enrichment of 12% provided a (BOL k_{eff} of 1.4, which was sufficient initial reactivity to maintain criticality after 20 years of operation.

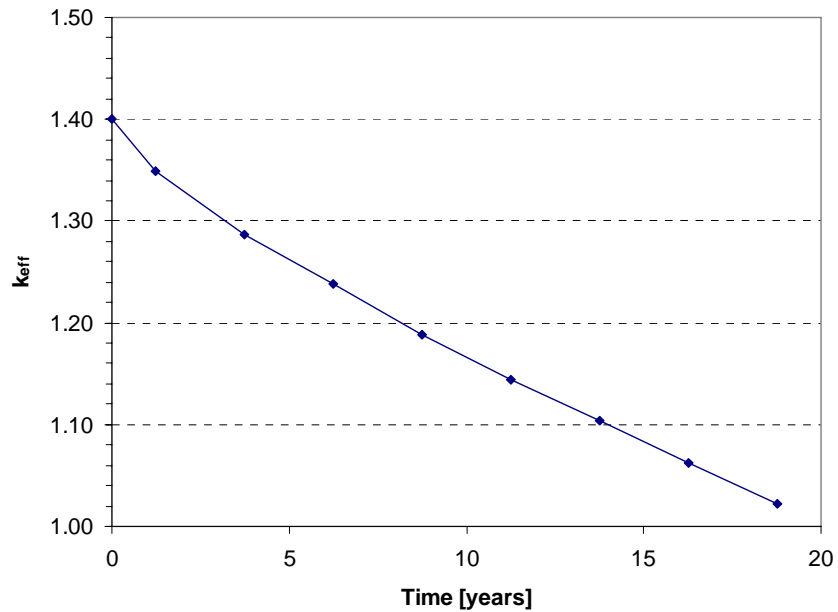


Figure 4.5. Burnup reactivity loss over 20 years for Zr base case

4.4.2.2 Burnup

The average burnup for the core for a 20 year irradiation would be $(300\text{MW})(7305\text{ days})/(41\text{MTU})= 53.4$ GWD/MTU. This equates to 5.7% fissions per initial metal atom (FIMA). Figure 4.6 shows the change in burnup (MW days per metric ton of U) for each of the sixteen radial fuel regions (cells) in the model. The burnup increases almost linearly after the first year and at 20 years the burnup for the various regions range from 40 to 100 GWD/MTU. In comparison, the US NRC has currently licensed commercial nuclear fuel to a 62 GWd/MTU rod average burnup level. The burnup range could be narrowed and the peak lowered by flattening the radial power distribution.

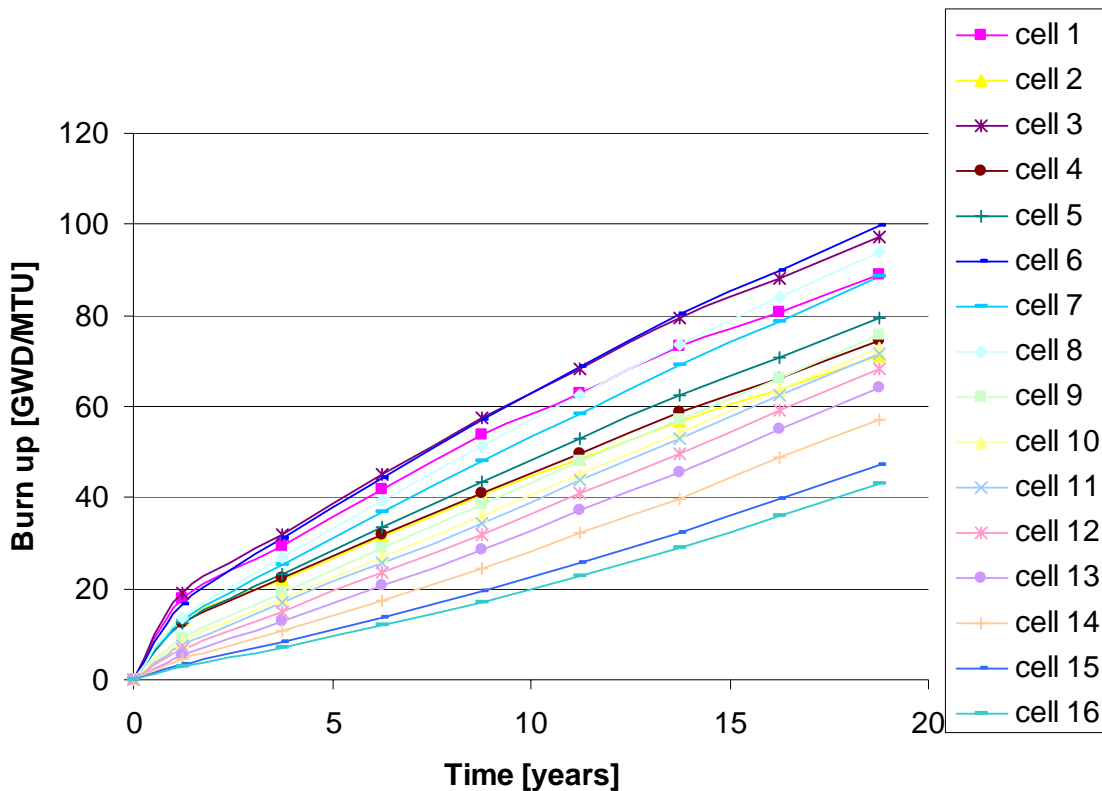


Figure 4.6. Burnup in each fuel region over 20 years for Zr base case

4.4.2.3 Power Distribution

Figure 4.7 shows the fuel kernel power density generated in each of the sixteen radial fuel regions during the 20 year irradiation with no refueling or fuel movement. The MCNP statistical uncertainty in the power in each fuel region was less than 1% in each time step. At BOL there is a factor of almost ten difference in power densities from the core center to the core edge, while at EOL this range has been reduced to about a factor of two. This illustrates the need for flattening the radial power distribution, which could be accomplished through enrichment zoning or burnable poisons. The goal would be to achieve average fuel power densities well below existing commercial fuel power densities (e.g., average fuel power density for a BWR is ~ 290 W/cc and that for a PWR is ~ 320 W/cc).

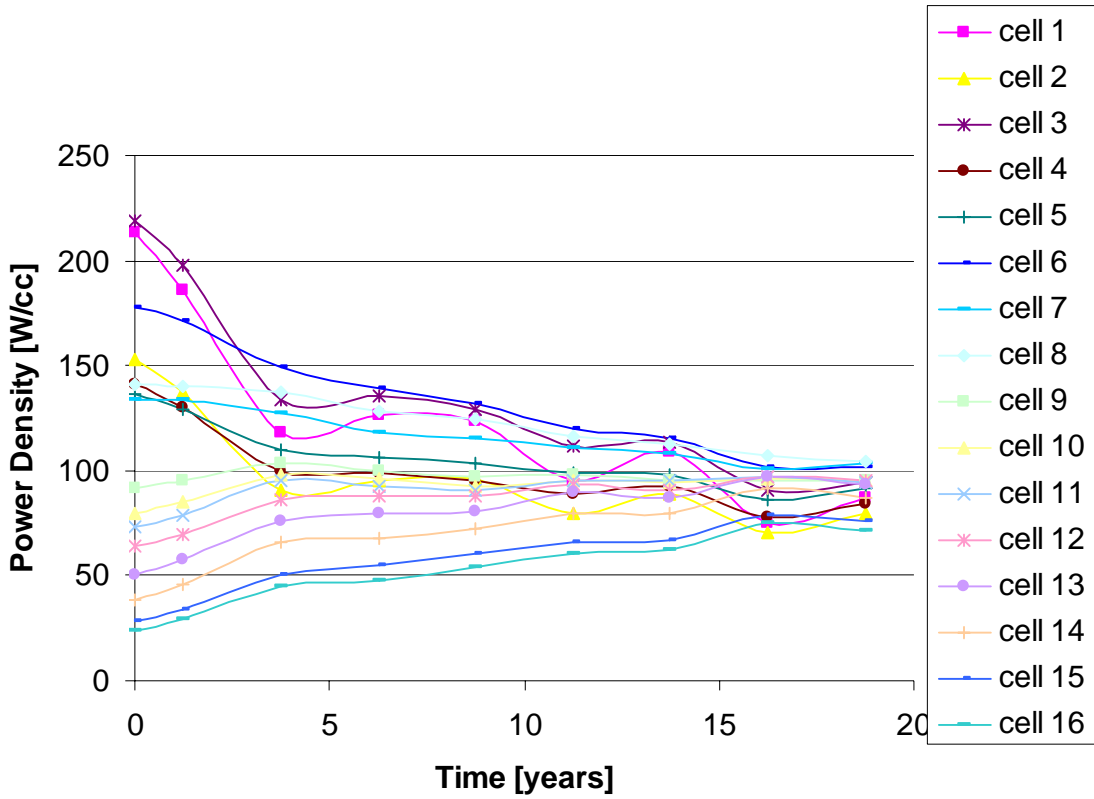


Figure 4.7. Fuel kernel power density in each fuel region for 20 year irradiation for Zr base case

4.4.3 Decay Heat

Figure 4.8 shows the decay power for the AFPR core as a function of time after shutdown. The values are based on an infinite irradiation of the initial fuel at the initial operating power of 300 MW. Values were derived from the ANS decay heat standard for light water reactors.

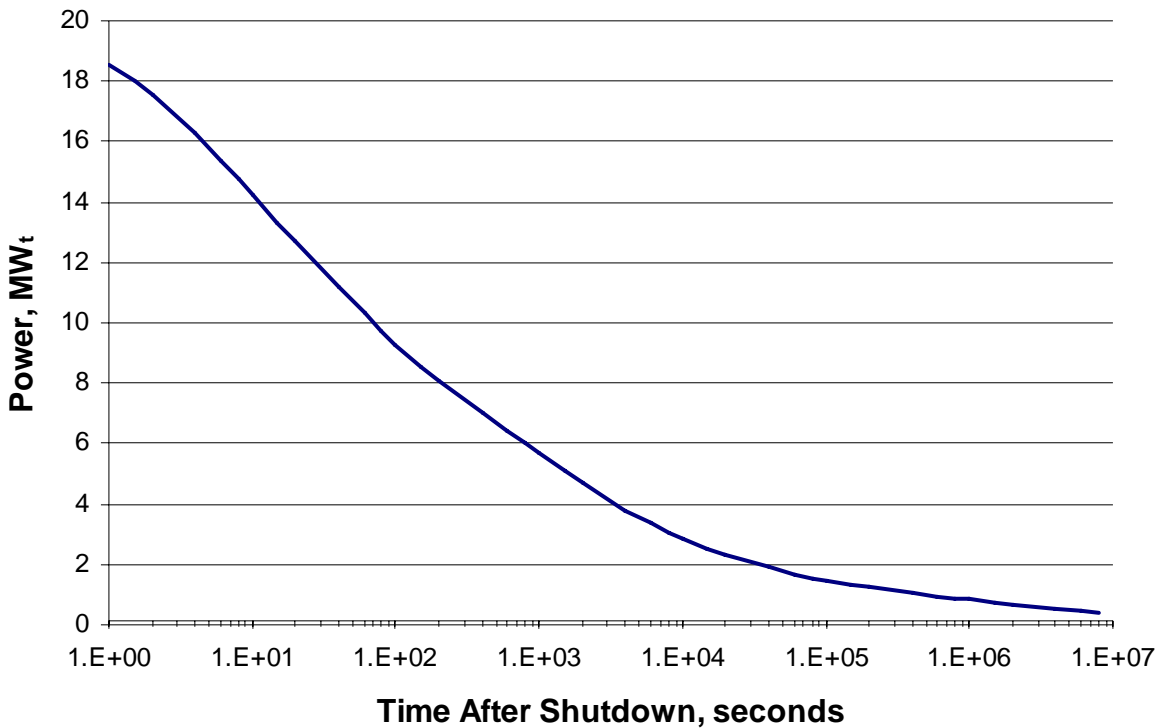


Figure 4.8. Decay power for the AFPR core as a function of time after shutdown

4.4.4 Fuel Isotopics

Table 4.5 shows the core average isotopics of the spent fuel after 20 years of operation for the Zr base case. The uranium has been reduced from the initial enrichment of 12 percent to an average of 5.1 percent. The plutonium isotopic composition is similar to that contained in commercial light water reactor spent fuel.

Table 4.5. Core average isotopics of spent fuel after 20 years of operation for Zr base case

| Pu/(U+Pu) | ²³⁵ U/U | ²³⁹ Pu/Pu | ²⁴⁰ Pu/Pu | ²⁴¹ Pu/Pu | ²⁴² Pu/Pu |
|-----------|--------------------|----------------------|----------------------|----------------------|----------------------|
| 0.015 | 0.051 | 0.638 | 0.188 | 0.132 | 0.0419 |

4.4.5 Reactivity Coefficients

The reactivity coefficients were calculated using the WIMS code. The calculations were performed at the beginning of life (no xenon or fission products) with europium burnable poison at hot operating conditions. The fuel temperature and void reactivity coefficients are -2.44 pcm/K and -168 pcm/%void, respectively. Typical LWR values are -4 to -1 pcm/K and -200 to -100 pcm/%void.

4.5 Analysis of ZrH_{1.6} Base Case

4.5.1 Description

Based on the parametric studies and the Zr base case results, a ZrH_{1.6} matrix base case configuration was defined for additional burnup analyses. The specifications for this case are shown in Table 4.6.

Table 4.6. Fuel Specifications for ZrH_{1.6} base case

| Fuel Parameter | Value |
|--|--------------------|
| Pebble Matrix Material | ZrH _{1.6} |
| Pebble Coating Material | Zr |
| Fuel Kernel Material | UO ₂ |
| Fuel Kernel Density, g/cm ³ | 10.7 |
| Kernel Packing Fraction | 0.3 |
| Pebble Coating Thickness, cm | 0.03 |
| Kernel Diameter, μm | 500 |
| Pebble Diameter, mm | 10 |
| Enrichment, % | 9 |
| UO ₂ mass, Mt | 36.1 |

4.5.2 Burnup Analysis

The MCNP5, ORIGEN2, and MONTEBURNS codes were used to model the irradiation of the ZrH_{1.6} base case core at a full power of 300 MWt for 20 years. The control rods were fully withdrawn and no burnable poisons were used.

4.5.2.1 Burnup Reactivity Loss

Figure 4.9 shows the change in k_{eff} due to the reactivity loss related to burnup for this case. The fresh fuel enrichment of 9% provided a BOL k_{eff} of 1.46, which was sufficient initial reactivity to maintain criticality for nearly 20 years of operation.

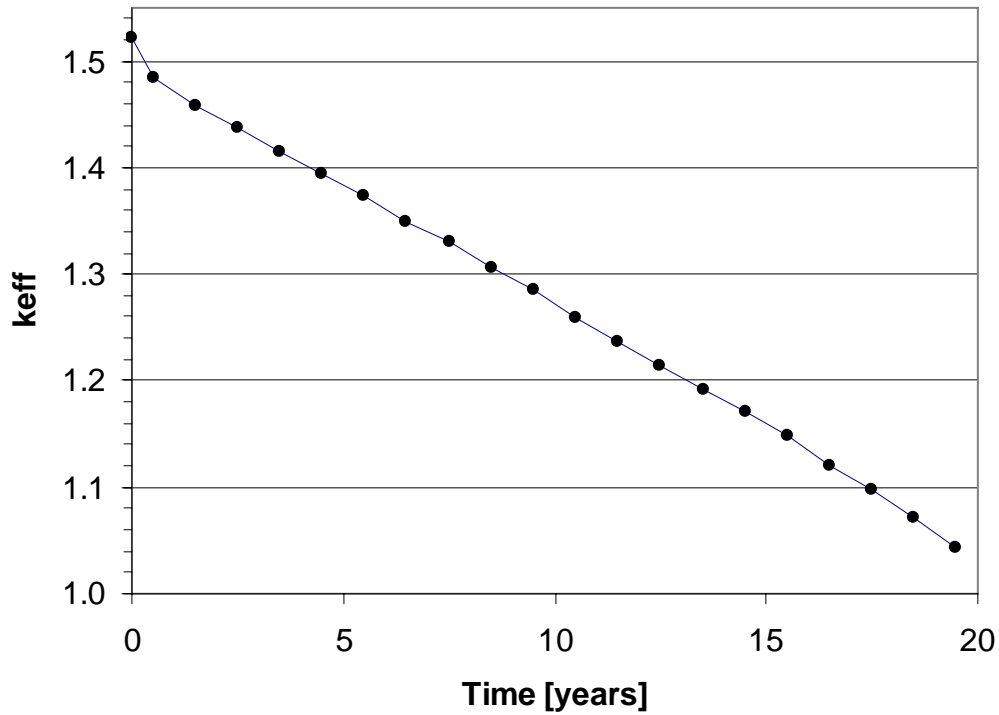


Figure 4.9. Burnup reactivity loss over 20 years for $ZrH_{1.6}$ base case

4.5.2.2 Burnup

The average burnup for the core for a 20 year irradiation would be the same as for the Zr matrix base case, 53.4 GWD/MTU, which again equates to 5.7% FIMA. Figure 4.10 shows the change in burnup (MW days per metric ton of U) for each of the sixteen radial fuel regions (cells) in the model. The burnup increases almost linearly after the first year and at 20 years the burnup for the various regions range from 47 to 80 GWD/MTU. The peak and the range of burnup values are significantly lower than that for the previous Zr case because the radial power distribution is much flatter. Again, existing commercial fuel is currently licensed to 62 GWD/MTU rod average burnup limit and the burnup range could be further narrowed, and the peak lowered, by additional flattening of the radial power distribution.

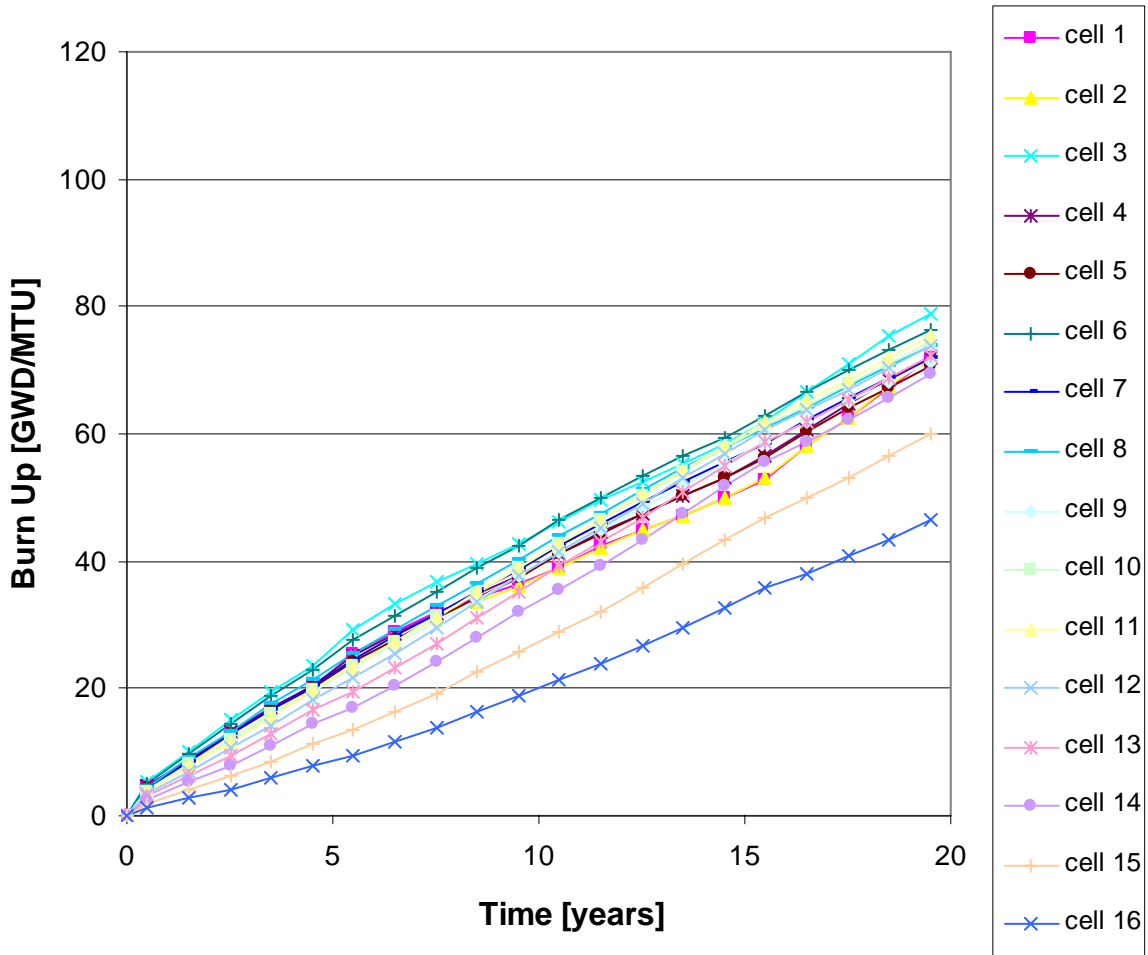


Figure 4.10. Burnup in each fuel region over 20 years for ZrH1.6 base case

4.5.2.3 Power Distribution

Figure 4.11 shows the power generated in each of the sixteen radial fuel regions during the 20 year irradiation with no refueling or fuel movement. At BOL there is still almost a factor of ten difference in power densities from the core center to the core edge, while at EOL this range has been reduced to less than a factor of two. This illustrates the need for flattening the radial power distribution, which could be accomplished through enrichment zoning or burnable poisons.

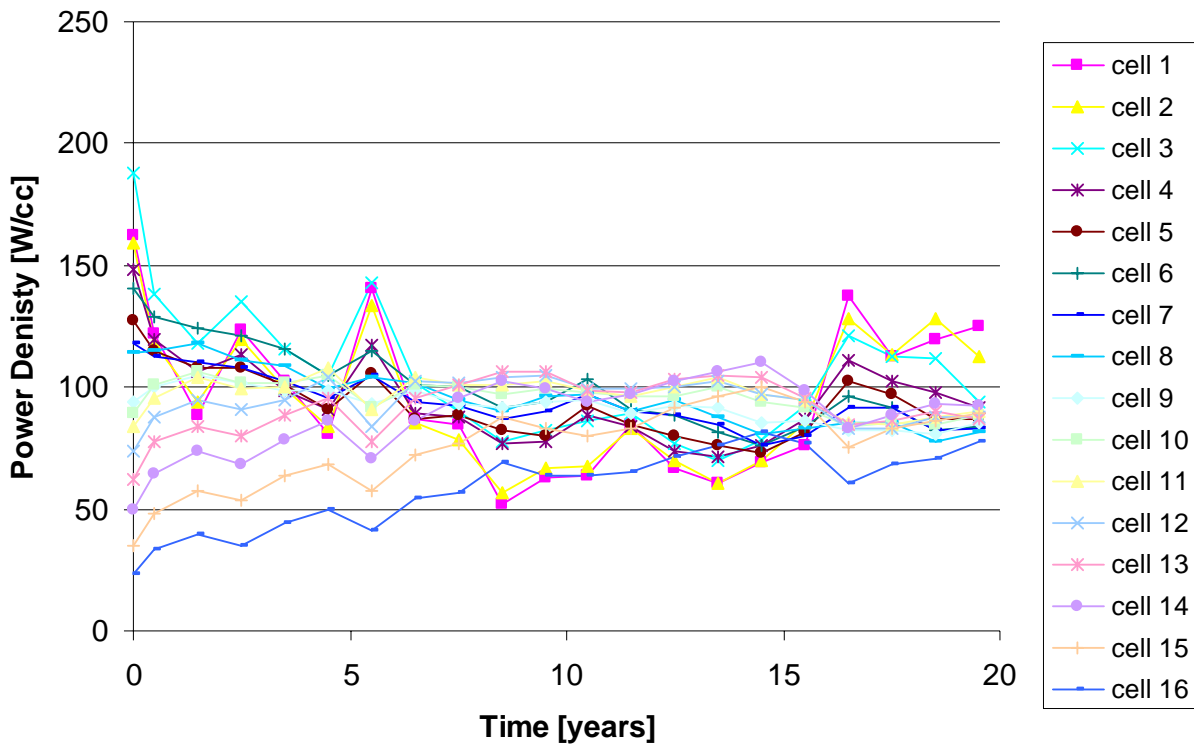


Figure 4.11. Power density in each fuel region for 20 year irradiation for ZrH_{1.6} base case

4.5.3 Decay Heat

The BOL decay heat for the ZrH_{1.6} base case would be essentially the same as for the Zr base case since both are based on predominantly ²³⁵U fission. After substantial burnup, the fuel isotopics will be different, causing differences in the decay heat.

4.5.4 Fuel Isotopics

Table 4.7 shows the core average isotopics of the spent fuel after 20 years of operation for the ZrH_{1.6} base case. The uranium has been reduced from the initial enrichment of 9 percent to an average of 2.4 percent. The plutonium isotopic composition is similar to that contained in commercial light water reactor spent fuel.

Table 4.7. Core average isotopics of spent fuel after 20 years of operation for ZrH_{1.6} base case

| Pu/(U+Pu) | ²³⁵ U/U | ²³⁹ Pu/Pu | ²⁴⁰ Pu/Pu | ²⁴¹ Pu/Pu | ²⁴² Pu/Pu |
|-----------|--------------------|----------------------|----------------------|----------------------|----------------------|
| 0.011 | 0.024 | 0.532 | 0.260 | 0.137 | 0.071 |

4.6 Analysis Alternatives

4.6.1 Radial Power Distribution Sensitivities

Fuel enrichment zoning is one way of flattening the radial power distribution, thereby increasing core lifetime and fuel utilization efficiency. Figure 4.12 shows the effects of two fuel enrichment zoning

schemes on the radial power distribution compared to the Zr base case with a single 12% enrichment. The first case reduced the enrichment in the innermost six fuel subregions to 5%. The second case used three enrichment zones, with innermost six subregions at 8%, the middle 4 at 12%, and the outer six at 16%. For the Zr base case there is almost a factor of ten difference in power density between the core center and core edge. The enrichment zoning can be seen to flatten the radial power distribution significantly by increasing the outer fuel power density and reducing the central power density. Because burnable poisons are required to reduce the BOL excess reactivity and power densities change dramatically with burnup over a 20 year irradiation, enrichment zoning will need to be examined jointly with the use of burnable poisons to determine the true impact. However, these studies do illustrate some of the potential benefits of considering enrichment zoning.

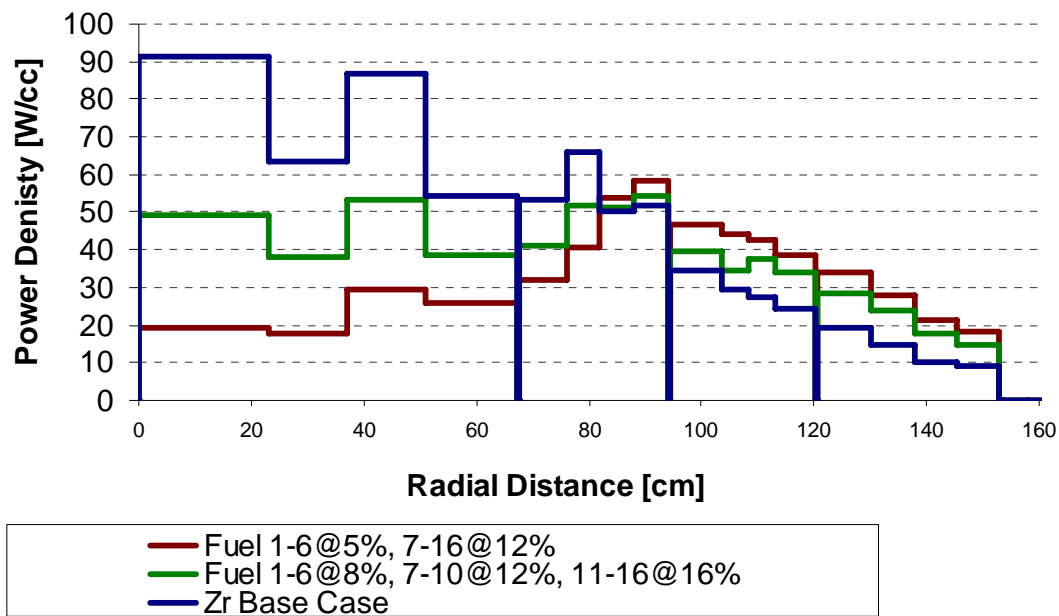


Figure 4.12. Impact of fuel enrichment zoning on radial power distributions

Another series of calculations looked at the impact on the radial power distribution of adding moderator rods, adding a radial reflector, and adding boron burnable poison to the Zr base case. The results are shown in Figure 4.13. For the moderator tube case 584 water-filled 2 cm diameter steel tubes were distributed throughout the core, displacing fuel pebbles. The central power density was reduced and the outer power density was increased slightly. For the reflector case a 20 cm beryllium reflector was added beyond the last radial fuel zone. This increased the outermost power density by about a factor of two, with some decrease in the inner fuel zones. For the burnable poison case, boron was added to the fuel material at 0.4% concentration in the inner eight fuel subregions and at 0.1% concentration in the outer eight fuel subregions, with a constant 12% fuel enrichment. This can be seen to dramatically flatten the radial power distribution.

From these studies, it appears that a combination of fuel enrichment zoning and burnable poison zoning could potentially be very effective in flattening the radial power profile.

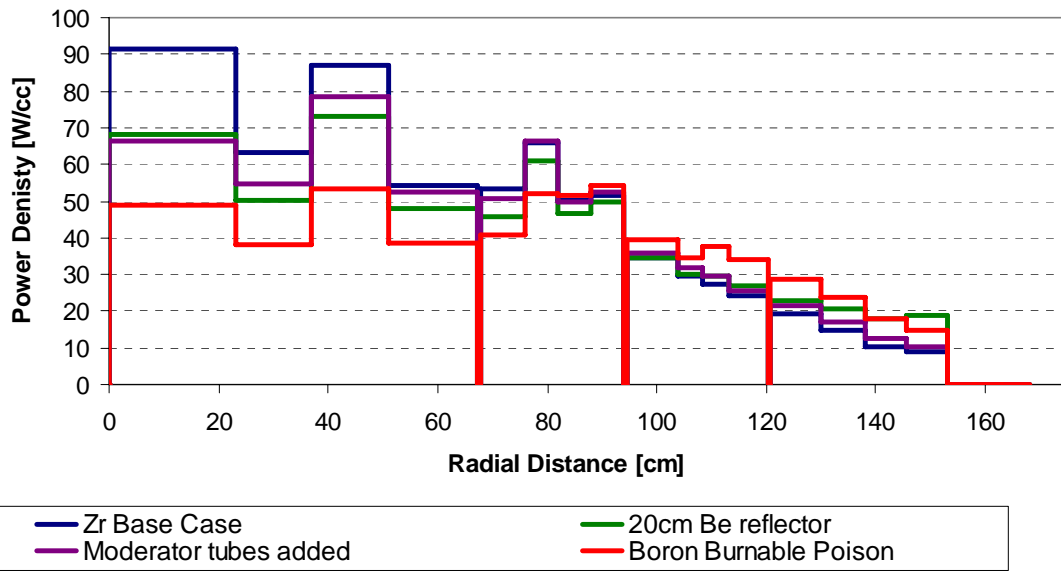


Figure 4.13. Impact of moderator rods and radial reflector on radial power distributions

While the previous studies were done based on the Zr base case, at least one variation on the ZrH base case was worth mentioning. Figure 4.14 shows that adding a 20 cm beryllium reflector significantly flattened the radial power distribution for a ZrH core.

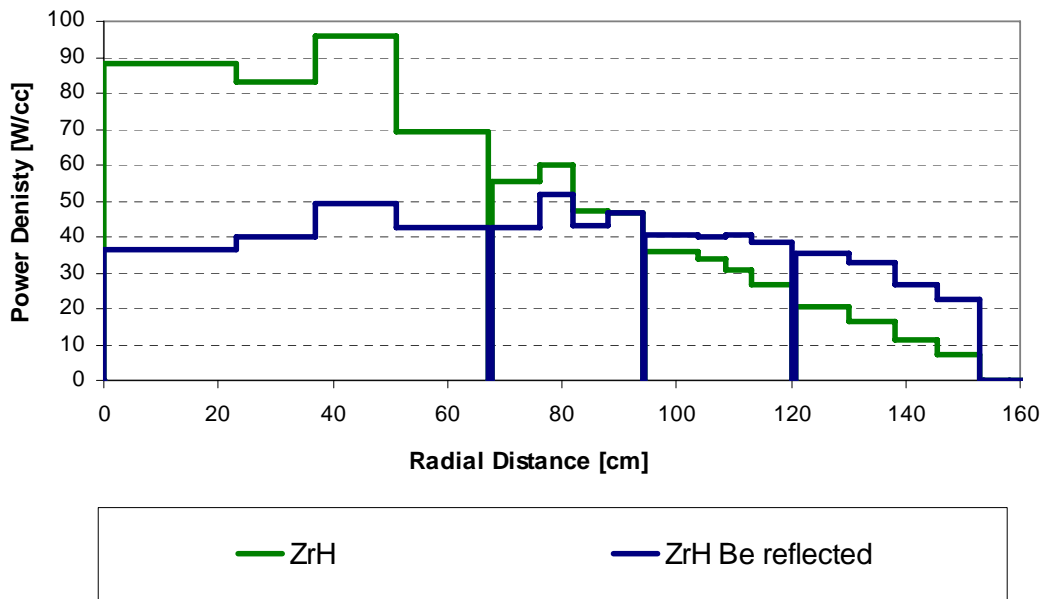


Figure 4.14. Impact of adding a radial reflector on the radial power distribution in the ZrH core

4.6.2 Burnable Poison Studies

The incorporation of a burnable poison into the AFPR core design is required to handle the amount of initial excess reactivity needed to maintain criticality in the core for 20 years without refueling. The desirable properties of a burnable absorber are

- The material should be compatible with the fuel, matrix, structural, and coolant materials
- The material should not produce undesirable transmutation products
- The material should have a neutron absorption level such that it completely burns out over the core lifetime without leaving significant residual negative reactivity.

A survey of potential burnable absorbers was made. Figure 4.15 shows the results of using no burnable poison, gadolinium, erbium, boron, and europium using the WIMS8 code. All burnable absorbers except boron were mixed with the UO_2 material. Boron was mixed in the Zr coating. It can be seen from the figure that gadolinium absorber is prematurely depleted, causing about 18% rise in reactivity. This huge reactivity increase makes it difficult to provide adequate shutdown margin (1% to 2% below critical). Boron, erbium, and europium depletions caused about 5%, 2%, and 1% rise in reactivity, respectively. Boron has a small residual absorption at the end of the cycle. Erbium appears to be more attractive than boron, but erbium has a higher hot-to-cold reactivity swing which would require more control rods to maintain adequate shutdown margin. Europium has the smallest reactivity increase, but it has more residual absorption than boron at the end of the cycle. Thus, the cycle length would be reduced. The burnable absorber of choice is narrowed down to boron and europium. It may be possible to control the reactivity increase when using boron by using different boron concentrations in the core (discussed later). The cycle length may be increased using europium by increasing fuel enrichment and/or increasing the fuel packing fraction.

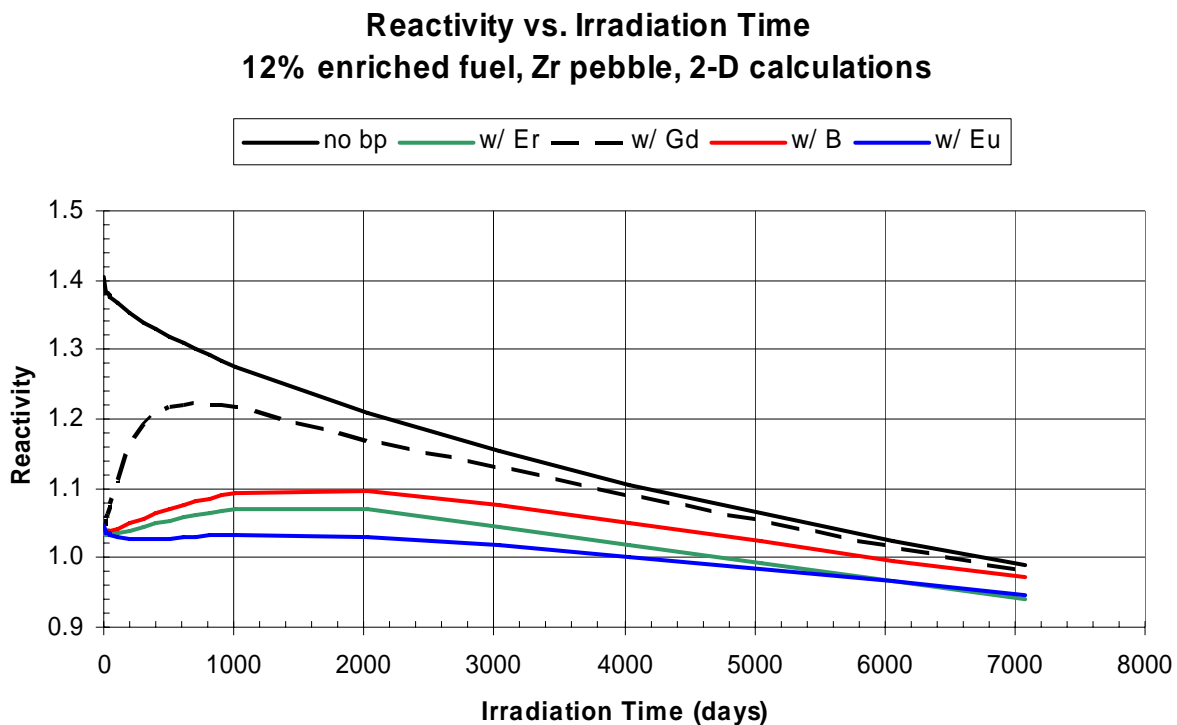


Figure 4.15. WIMS results using different burnable absorbers

One case that illustrates the feasibility of using boron as a burnable poison was a modification of the Zr base case where two different boron concentrations were added to the fuel material. In fuel subregions 1 through 8 a natural boron concentration of 0.4% was added, while in fuel subregions 9 through 16 a natural boron concentration of 0.1% was added. The fuel enrichment was kept the same constant 12% in all fuel regions. This case was burned for 20 years in MONTEBURNS. The reactivity loss with burnup over the 20 years is shown in Figure 4.16. The core k_{eff} was maintained between 1.04 and 1.1 over the 20 years. Figure 4.17 shows the power distribution changes with burnup over the core life. The boron in the central fuel regions starts to completely burn out after 15 years and the power in those regions starts to rapidly increase. Other than the central three regions, the power density distribution exhibits an orderly transfer between the outer fuel regions dominating at BOL to the inner fuel regions dominating at EOL. The problem with the central fuel zone can likely be resolved by further adjustment of the fuel enrichment and burnable poison zoning.

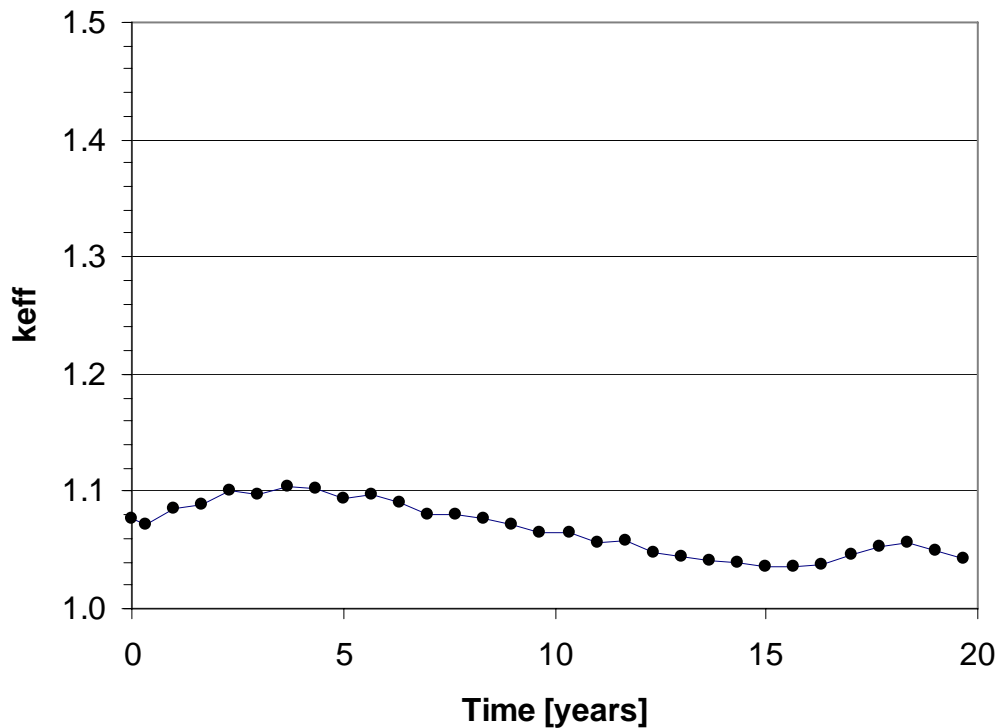


Figure 4.16. Burnup reactivity loss over 20 years for Zr case with 2 zone boron burnable poison

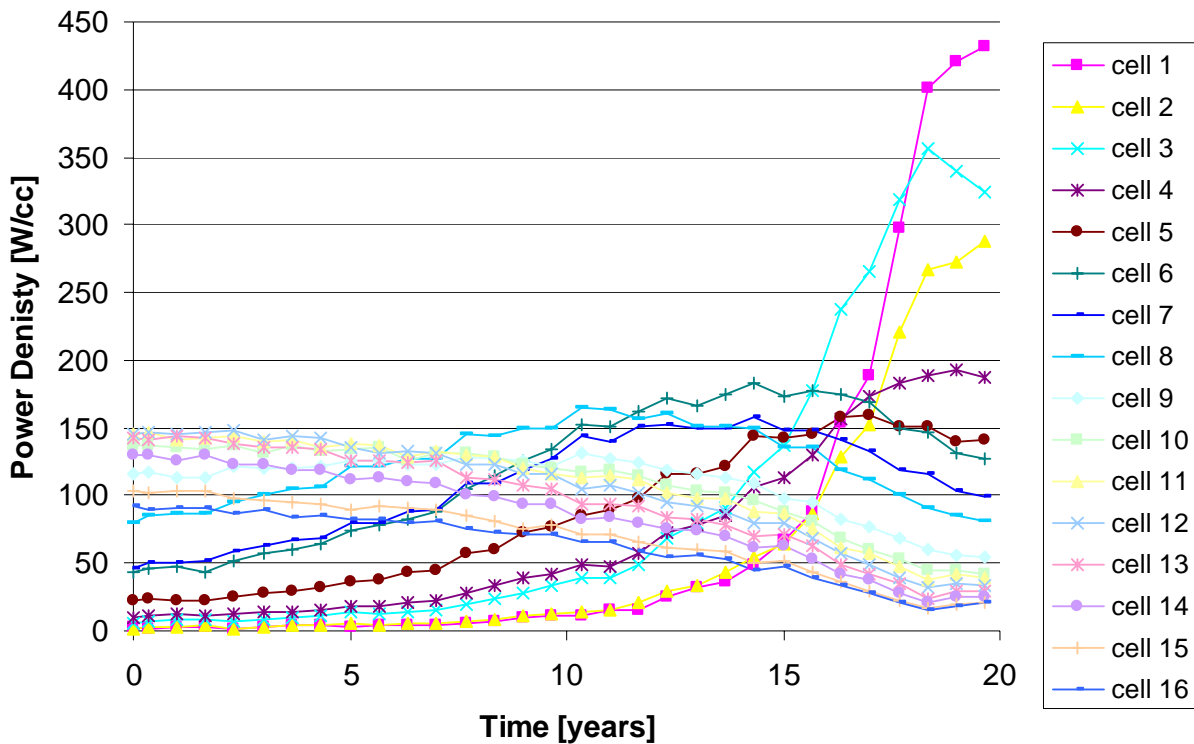


Figure 4.17. Power density changes over 20 years for Zr case with 2 zone boron burnable poison

4.6.3 Core Lifetime Studies

Two studies were made of ways of extending the core lifetime by increasing the amount of fuel in the core. One was to increase the fuel kernel packing fraction and the other was to increase the core size. The Zr base case was first modified by increasing the kernel packing fraction from 0.3 to 0.4 and 0.5. This effectively increased the uranium fuel loading in the core (displacing Zr) without changing the coolant or moderator volume or the core size. These cores were then burned for 20 years. Figure 4.18 shows the core reactivity at BOL was not impacted, but the reactivity loss rate due to burnup was decreased significantly with the higher kernel packing fractions. The burnup in the fuel will also be reduced proportional to the increase in MTU. These cases indicate that core lifetimes significantly beyond 20 years are possible. Alternately, the fuel enrichment could be lowered for a 20 year lifetime. The second variation involved modifying the Zr base case by increasing the core radius while keeping the same core height such that the core volume was increased by a factor of two. This case was then burned for 20 years. Figure 4.19 shows the core reactivity at BOL was not impacted, but the reactivity loss rate due to burnup was decreased significantly with the increase in core volume and fuel mass. The results are very similar to the case above with a fuel kernel packing fraction of 0.5. Figure 4.20 shows the burnup in each fuel region for this case. It can be seen that the peak burnup decreased by about a factor of two compared to the Zr base case, proportional to the change in MTU.

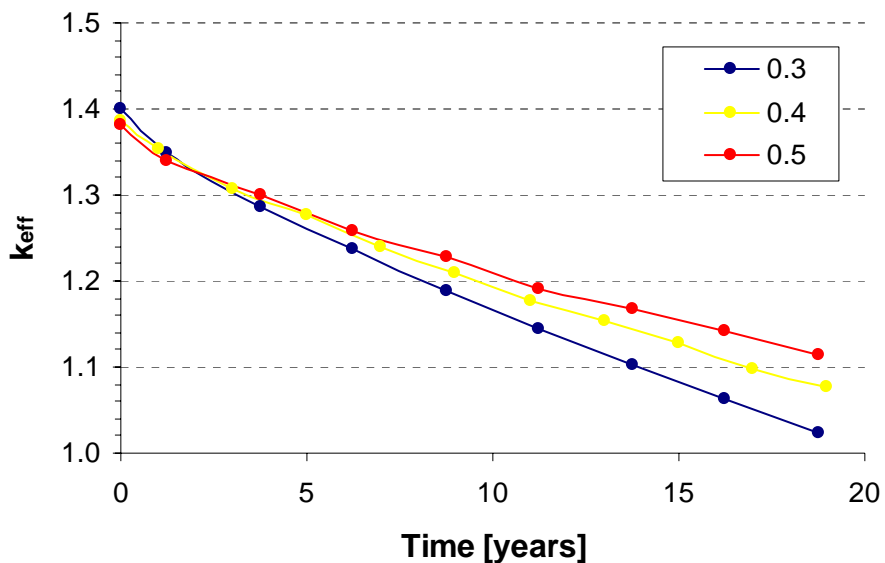


Figure 4.18. Effect of increasing kernel packing fraction on burnup reactivity loss for Zr base case

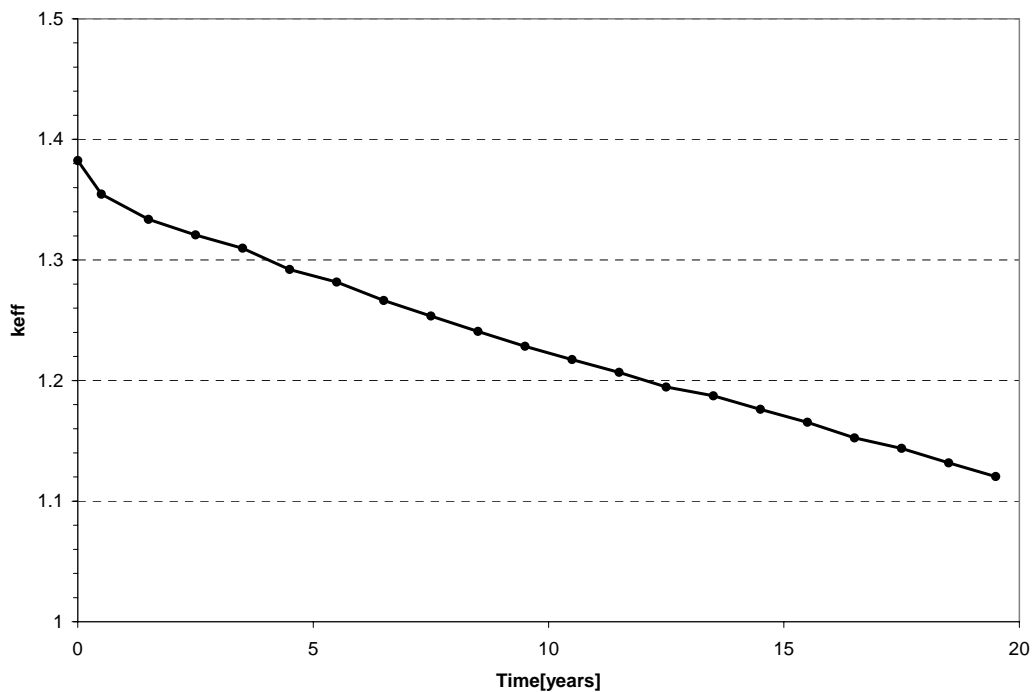


Figure 4.19. Burnup reactivity loss over 20 years for Zr case with core volume doubled by increasing the core radius

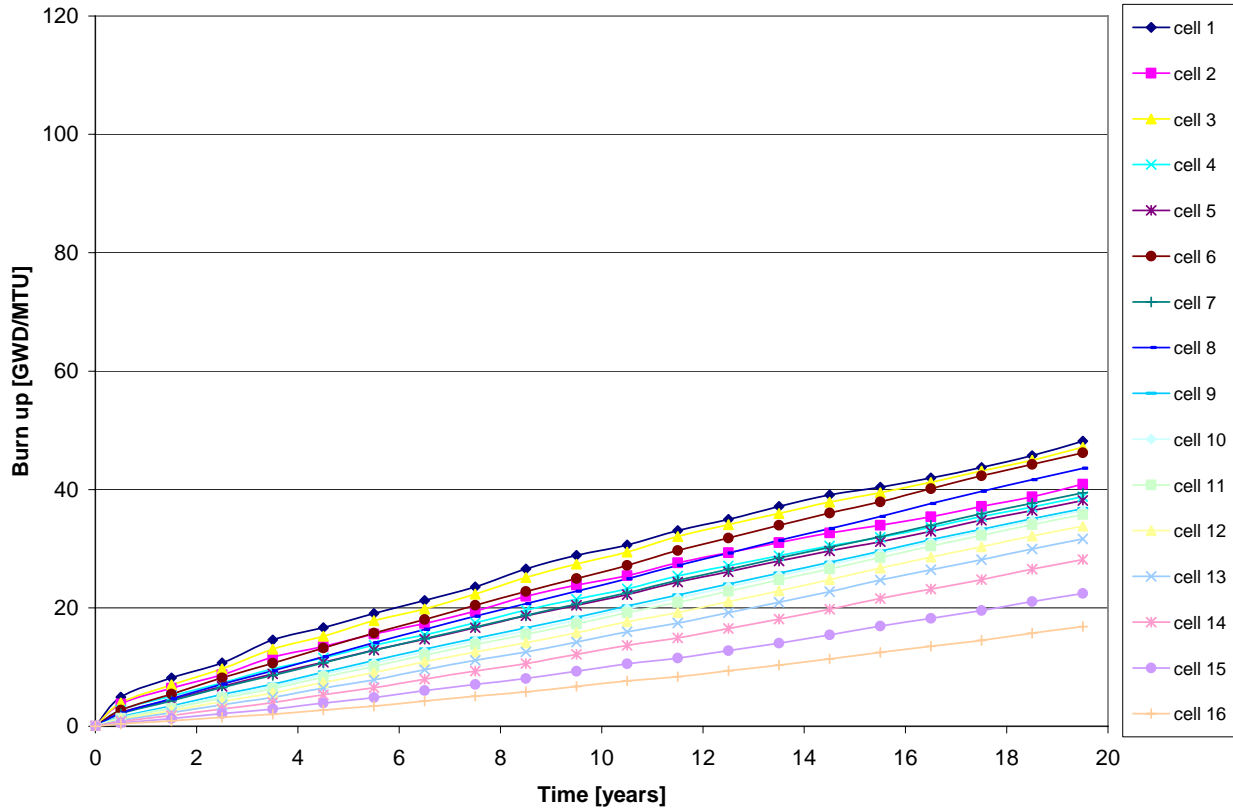


Figure 4.20. Burnup for each fuel region over 20 years for Zr case with core volume doubled by increasing the core radius

4.7 Spectral Comparisons

Figure 4.21 compares the core average neutron spectrum for the fuel pebbles for the Zr base case, the ZrH_{1.6} base case and the Zr case with boron burnable poison. As expected the main differences are in the thermal part of the spectrum, with the highest thermal flux in the ZrH case and the lowest for the boron burnable poison case. The spectra over the rest of the energy range are very similar.

**AFPR Fuel Particle Neutron Flux Spectrum
(Normalized to a total of 1.0)**

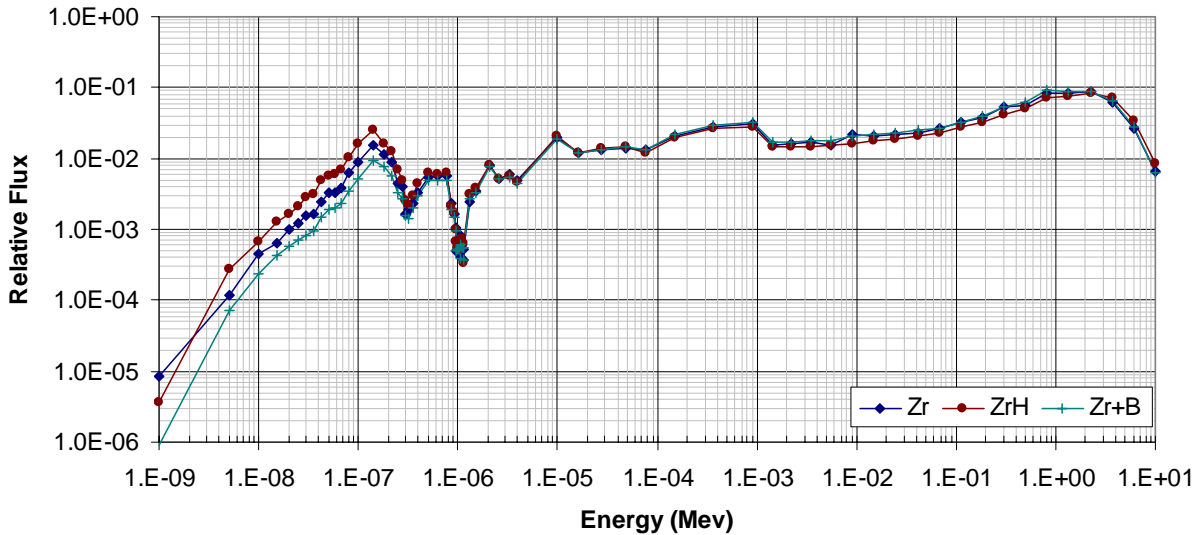


Figure 4.21. Neutron spectrum comparison between Zr base case, ZrH base case, and B burnable poison case

For reference, Figure 4.22 compares these same spectra with the spectra from the previous micro-fuel core concept that had SiC pebbles and varying coolant densities. Spectra from four different regions with coolant densities ranging from 0.055 to 0.607 g/cc are shown. The low coolant density regions have lower thermal flux components than the boron burnable poison case.

Dr. Larry Greenwood used the SPECTER code (Greenwood 1985) along with the fast fluence values arrived from the neutron spectrum to predict irradiation damage in 316SS in terms of displacements per atom and Helium production. The results are provided in Table 4.8.

Table 4.8. Radiation Damage and Helium Production Estimates

| Full Power Years | 1 | 20 | 30 | 40 |
|--------------------------------|----------|-----------|-----------|-----------|
| Fluence, n/cm ² | 3.51E+21 | 7.02E+22 | 1.05E+23 | 1.40E+23 |
| Radiation Damage in 316SS, dpa | 1.7 | 34.5 | 51.9 | 69.2 |
| Total Helium in 316SS, appm | 5.7 | 154.8 | 257.2 | 371.2 |

AFPR Fuel Particle Neutron Flux Spectrum (Normalized to a total of 1.0)

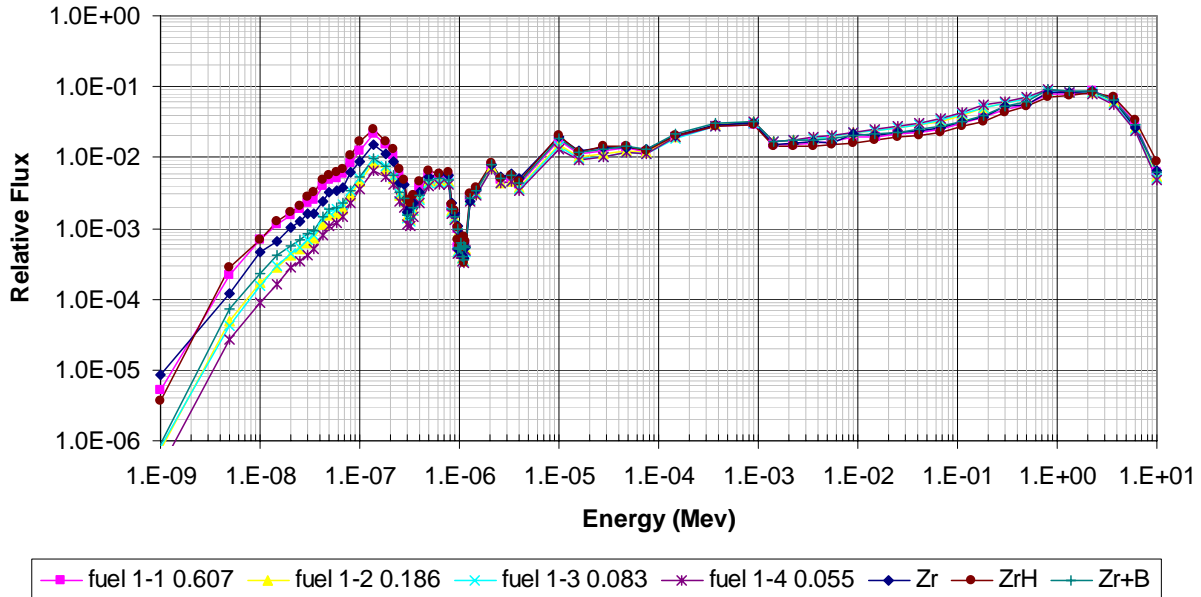


Figure 4.22. Comparison of neutron spectra for current cermet fuel cases with previous micro-fuel concept

4.8 Conclusions

From a physics perspective, the AFPR cermet fuel concept appears feasible. These preliminary scoping studies have examined the physics aspects of the AFPR cermet fuel and provided the following conclusions:

- Feasible nuclear core configurations based on the proposed Zr or ZrH cermet fuel concept are defined for further studies.
- Both fuel temperature and void reactivity coefficients are negative and are comparable with the LWR reactivity coefficient values.
- The Zr or ZrH cermet fuel concept allows for a higher moderator/fuel ratio (i.e., better moderation of neutrons) which translates to improvements over the previous micro-fuel concept in fuel usage and irradiation dose to structural materials.
- A 20+ year core lifetime is achievable based on neutronic analysis and options for extending core lifetimes in excess of 20 years were identified. These options include increasing the diameter of the core and using integral burnable poisons in the fuel. Such modifications would be beneficial in terms of lowering the peak and average power densities and fuel burnup.
- Fuel performance parameters of burnup and power density were within expected acceptable ranges.
- Burnable poison is needed to handle the initial excess reactivity and schemes for including this in the fuel design were identified.

5.0 Thermal Hydraulics Analysis

The basic concept of the AFPR core design is a water-cooled, fixed-particle bed, randomly packed with spherical fuel elements approximately 10 mm in diameter. The overall size and shape of the core is a right circular cylinder 3 m in height and 3 m in diameter, consisting of a series of four annular rings containing the fuel particles. As discussed in some detail in Sections 3 and 4, this basic configuration is well suited to achieving the desired fuel performance and core neutronics for the reactor. It does, however, present some interesting challenges to core thermal-hydraulics that are quite different from those usually encountered in existing commercial light water reactor (LWR) designs.

As discussed previously this concept evolved from an earlier proposal which utilized TRISO fuel (~1 mm diameter) and core cooling was achieved by means of two-phase flow within the particle bed. Because of the extremely high pressure drop expected in two-phase flow conditions over the 3-m height of the core, the concept required horizontal cross flow (rather than axial flow) through annular fuel sections containing the TRISO micro fuel elements. The annular fuel sections containing fuel particles were separated by annular open flow channels for inlet flow of single-phase coolant (water) and exit flow of the two-phase steam–water mixture. Radial flow through the fuel channels reduces the boiling flow length to a relatively small distance, compared to the axial height of the core, and consequently much smaller drag and friction losses might be expected. Uniform inlet flow distribution along the axial length of the core would be obtained by manifold orificing along the inner wall of each radial ring containing fuel particles (but at the price of additional pressure losses.) Orificing would be required on the outer wall of a given ring, as well, to vent the steam–water coolant mixture into an open annular channel where steam separation would occur, presumably with only minimal carryover.

While in theory, the initial concept appeared to be a solution to the high pressure drop across the core (assuming traditional axial flow), realizing such an arrangement in a functioning reactor is highly problematic. From the standpoint of designing inlet and outlet orificing on the annular fuel channels that would achieve the desired flow distribution in the core without unacceptable pressure losses and without allowing fuel pebbles to fall or be carried into the coolant channels could be a real engineering challenge for such small diameter fuel element (i.e., TRISO outer diameter ~1mm). Even without these mechanical design issues, the thermal-hydraulic behavior of two-phase flow in a particle bed presents a number of difficult challenges:

- Pressure drops are very high, compared to single-phase flow, and flow distribution patterns are difficult or impossible to control, which can result in local hot spots within the bed, local “chugging” of the flow as steam bubbles form and collapse at low qualities, and at higher qualities, it is very difficult to prevent phase separation and flow stratification. This behavior can cause steep temperature gradients within the bed, particularly for relatively deep beds (as would be the case with the AFPR core, with a 3-m height relative to a radial flow length of no more than about 0.3 m for a given annular ring.)
- Boiling within the particle bed will deposit any dissolved or suspended impurities in the coolant directly onto the fuel particles, which usually results in decreased surface heat transfer rates and increased local pressure drops. Depending on the chemical and physical properties of the deposited material, this could lead to direct damage to the fuel particles as a result of corrosion, cracking, or other physical changes in the material at the fuel particle surface.

- Engineering experience with two-phase flow in commercial-scale (i.e., large) particle beds is extremely limited, and very few useful empirical correlations exist for design and analysis of this configuration. Extensive experimental background work would be needed to verify and validate useful design correlations applicable to a large particle bed in two-phase flow.

The technical challenges of the two-phase core design could probably be overcome, with appropriate application of resources for research and development, but it is unlikely that the final result would easily meet the criteria of long life, mechanical stability, and passive safety that is envisioned for the AFPR. Therefore, for the thermal hydraulic analysis of a core filled with 10 mm diameter spherical cermet fuel elements single-phase flow in a fixed bed is assumed. Section 5.1 describes the main thermal-hydraulic features of single-phase flow in the core and assumes that steam will be generated by depressurization through a throttling nozzle configuration after the coolant exits the fuel region in order to eliminate the need for steam generators. Section 5.2 presents scoping calculations to determine the thermal-hydraulic characteristics of the core during normal operation. Section 5.3 discusses the important considerations of the design relative to performance in operational transients and accident conditions.

5.1 Core Design for Single-Phase Flow

Having determined that single-phase flow of the coolant through the core is a more desirable flow configuration than two-phase flow, there remains the question of the optimum orientation for the flow stream. Horizontal orientation has the advantage of not having the added component of head loss required to overcome gravity, but thermal stratification of the bed is an almost inevitable consequence, unless the flow rate is quite high. In a particle bed, the flow rate generally needs to be as low as possible, so that the pressure drop will be as low as possible, and to avoid problems associated with fluidizing the bed. Given these constraints, there is no inherent advantage in a horizontal orientation for the AFPR core, particularly since the gravity head loss due to the 3-m height of the core cannot be more than about 0.024–0.028 MPa (3.5–4.0 psi), depending on the coolant temperature. Vertical orientation of the flow has the decided advantage of assuring more radial uniformity across the core, and generally allows greater control over the inlet flow distribution.

With vertical flow, there is the matter of selecting the most advantageous flow direction; upflow or downflow. There is a great temptation to pick downflow, if only to realize the advantage of having gravity work *for* rather than *against* the desired flow direction. However, this is in practice only a rather small advantage, which is entirely obviated by the complications of accident conditions where the coolant may experience two-phase flow conditions. Boiling in a core with downflow is generally a very undesirable condition, as it can lead to severe flow instabilities, counter-current flow, liquid hold-up, and localized dryout below the boiling region. This flow configuration can, in some cases, make a severe accident out of what would with vertical upflow be only a minor operational transient.

The practical choice for the basic configuration of the AFPR, therefore, is vertical upflow through the core, in a manner similar to the design of current commercial LWRs. Figure 5.1 presents a very simple conceptual illustration of the core, showing a horizontal ‘slice’ through the annular rings of fuel channels.

In the thermal-hydraulic analyses presented in this section, the physical dimensions of the core are based on the fuel design and neutronics analyses, presented in Sections 3 and 4. The physical geometry of the core has been treated as fixed, and the operating parameters adjusted to obtain the desired performance characteristics. If the total thermal power remains at 300 MW and required core inlet and outlet

temperatures are unchanged, then the total flow rate in the core will not change. If the flow rate remains the same and the fuel particle geometry is unchanged, the core pressure drop can change only if there are changes in the core cross-sectional area and/or the core height. The effect on pressure drop can be summarized as follows:

- Increasing the core flow area will tend to decrease the pressure drop.
- Increasing the core height will tend to increase the pressure drop.

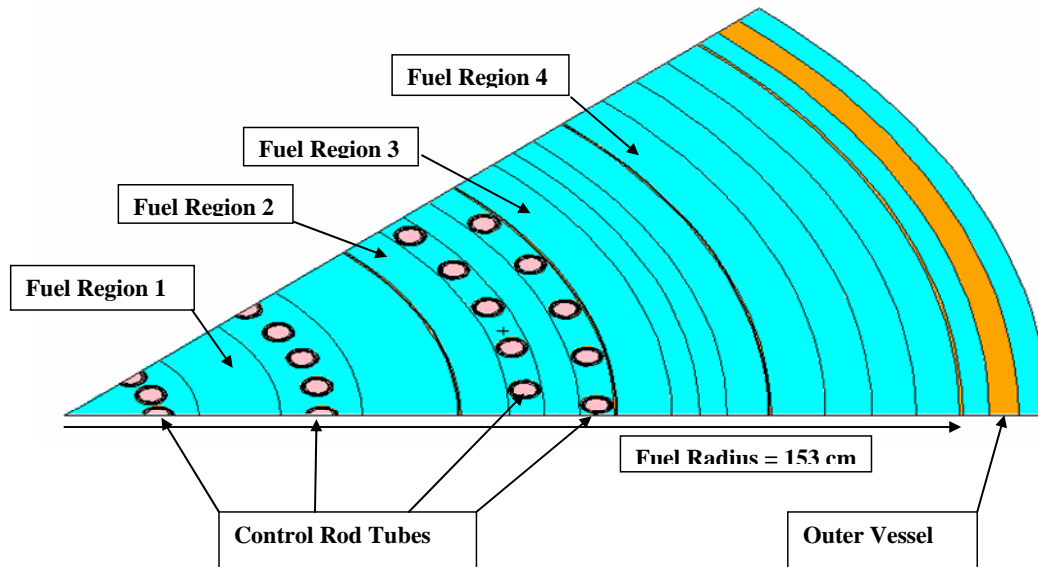


Figure 5.1. Conceptual Illustration of Packed Bed Core with Vertical Upflow Cooling

If changes in the core geometry result in changes in the total core volume, it will affect the number of fuel particles required to fill the core. This in turn will affect the power density in the fuel, and consequently the fuel temperatures. If the number of fuel particles increases, the power density will go down, and so would the fuel temperatures, all other things being equal. If the number of fuel particles decreases, power density will go up, and so would the fuel temperatures.

Two alternative variations in core geometry were evaluated to determine the effect on core thermal-hydraulics. One alternative concept doubled the volume of the core by expanding the radius to 4.8 m (but keeping the height at 3 m.) This change had no effect on core flow rate or pressure drop, but because of the reduced power density in the fuel, the predicted fuel temperatures were lower by approximately 15°C (27°F). The second alternative concept decreased the core volume by removing the first two fuel regions of the inner-most fuel channel, creating an annular configuration for the entire core. This change resulted in an 8% increase in core pressure drop and about a 2°C (1°F) increase in fuel temperature.

These results show that minor changes in the core geometry result in only minor changes in the core operating conditions. The behavior of the core remains essentially the same, assuming the same design constraints. Therefore, the results obtained with the current design assumptions can be treated as generally representative of core performance. Based on the analysis presented in Section 5.2, representative operating conditions in the core have been selected, as follows:

core exit pressure: 12.41 MPa (1800 psia)
 core inlet temperature: 204°C (400°F)
 core exit subcooling: 16.7°C (30°F) below saturation at core exit pressure
 core flow rate: 585 kg/sec (1290 lbm/sec), assuming 1.5% core bypass flow
 core power: 300 MW(thermal)

Figure 5.2 shows a plot of the coolant temperature as a function of pressure, from the core inlet to exit, and then to the point of steam generation. The coolant temperature rises from 204°C (400°F) at the core inlet to 310°C (590°F) at the core exit, in the process of absorbing 300 MW from the fuel. The friction pressure drop from core inlet to exit is only about 0.0336 MPa (4.9 psi), due to the relatively low velocity of the flow through the packed bed formed by the fuel pellets. Adding the gravity head loss increases the total pressure drop in the core to approximately 0.0564 MPa (8.2 psi).

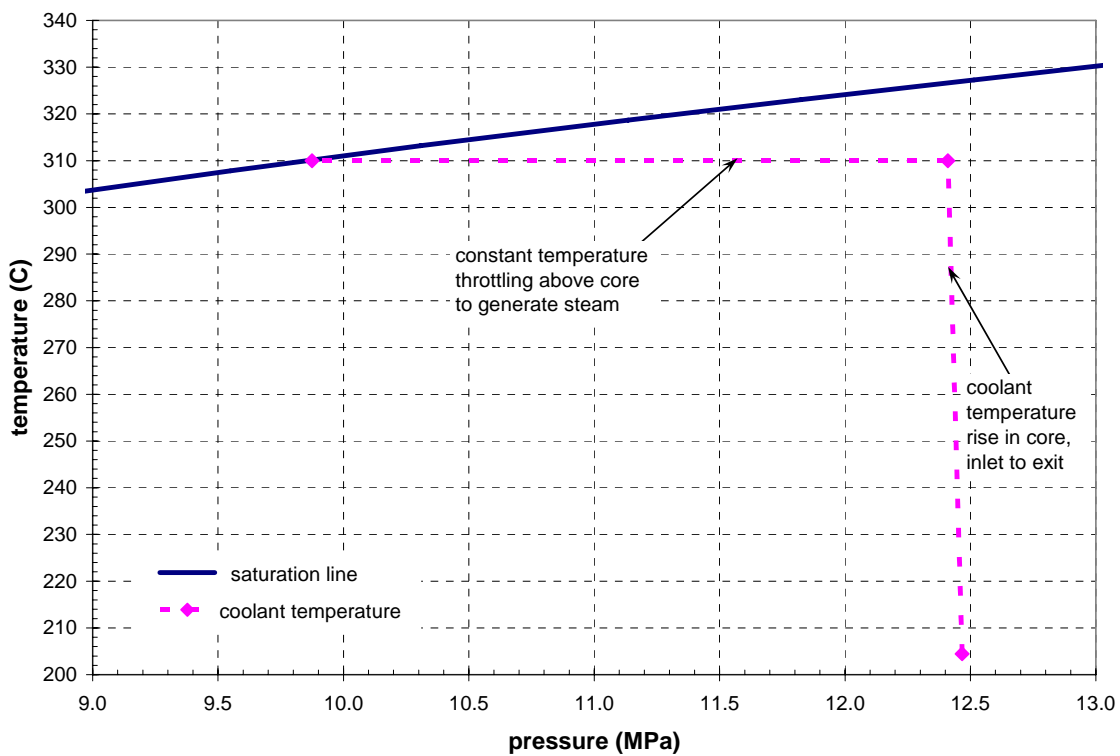


Figure 5.2. Estimated Operating Temperatures and Pressures in the AFPR at 300 MW(thermal)

The coolant is single-phase as it exits the core, at an average temperature that is 16.7°C (30°F) below the saturation temperature at the core exit pressure. Steam is generated by throttling the coolant to the saturation pressure corresponding to the core exit temperature—the efficiency associated with such an approach was not analyzed. In this case, the pressure must decrease to approximately 9.875 MPa (1432 psia) in the throttling process, which amounts to a pressure drop of approximately 2.5 MPa (368 psi) below the core exit pressure. By using a throttling process to generate steam, rather than nucleate boiling in the core, pumping power is not required in the steam generation step. Pumping power is needed only to overcome the pressure losses due to single-phase flow in the system, which are extremely small at the velocities expected. Based on one-dimensional calculations, pressure losses in the core are expected to be

about 0.0564 MPa (8.2 psi), and total losses in the single-phase flow system can probably be limited to less than 0.138 MPa (20 psi), by careful design of the overall flow loop.

5.2 Core Thermal-Hydraulics for Single-Phase Flow

As noted in Section 5.1, the physical dimensions of the core used in the thermal-hydraulic analysis are based on the neutronics analyses presented in Section 4. The physical geometry of the core has been treated as fixed, and the operating parameters adjusted to obtain the desired performance characteristics. Minor changes in the physical dimensions of the core (e.g., increase or decrease in core height, core diameter, number and radii of annular rings), will result in changes in the precise values predicted for flow rate, pressure drop, temperature rise, etc., but the general behavior of the core would be essentially the same, assuming the same design constraints were applied. Section 5.2.1 presents analyses of the thermal-hydraulics of the core flow, and Section 5.2.2 considers the material temperatures that might be obtained for postulated flow conditions.

5.2.1 Core Operating Conditions

At this conceptual design phase, meaningful analysis of detailed core thermal-hydraulic behavior would be extremely limited in scope, since many assumptions would have to be made regarding the physical structure of the flow paths, in effect pre-empting the mechanical design with manifold decisions on local dimensions, piping structures, size and shape of orifices, locations of structural support plates, etc. Fortunately, a detailed thermal-hydraulic analysis is not actually needed at this point in the process. The conceptual design needs to answer only three relatively simple questions regarding the thermal-hydraulic behavior of the system. Given the specified thermal output, these are

- can this core be cooled?
- at an acceptable pressure drop?
- with acceptable temperatures for the coolant and fuel material?

These questions can be answered by a fairly straightforward one-dimensional analysis applying the basic equations for conservation of energy, momentum, and mass in the system. As currently envisioned, the relevant system description of the AFPR core is shown in Table 5.1.

Table 5.1. AFPR Core Design Parameters Relevant to Thermal-Hydraulic Analysis

| | |
|---|---|
| power output (thermal) | 300 MW |
| acceptable range of core inlet temperature | 200-275°C (392-527°F) |
| acceptable range of peak fuel pebble center temperature | 350-375°C (662-707°F) |
| acceptable range of core exit subcooling | minimum: 5.6 °C (10 °F) maximum: 27.8 °C (50 °F) |
| nominal core geometry | 4 annular rings of channels containing randomly packed 10 mm fuel pebbles: overall height: 3 m nominal diameter: 3 m bed porosity: 0.4 |

The flow rate required to remove 300 MW from the core with a specified coolant temperature change inlet to outlet can be determined by a simple energy balance;

$$Q = m(h_{exit} - h_{inlet}) \quad (5.1)$$

where

$$\begin{aligned} Q &= \text{thermal power (MW)} \\ m &= \text{mass flow rate (kg/sec)} \\ h_{inlet} &= \text{coolant inlet enthalpy (kJ/kg)} \\ h_{exit} &= \text{coolant exit enthalpy (kJ/kg)} \end{aligned}$$

Just as the required flow rate can be determined from an energy balance on the core, the pressure drop through the core resulting from that flow rate can be determined from a momentum balance. For almost any fluid flow problem, a one-dimensional analysis of conservation of momentum can be obtained by means of the modified Bernoulli equation,

$$dP = \left(\frac{f(dL)}{D_h} \right) \left(\frac{\rho V^2}{2} \right) + \rho g dZ \quad (5.2)$$

where

$$\begin{aligned} dP &= \text{pressure change (Pa) over the flow length } dL \text{ (m)} \\ f &= \text{friction loss coefficient (dimensionless)} \\ D_h &= \text{hydraulic diameter of the flow channel (m)} \\ \rho &= \text{density of the flowing fluid (kg/m}^3\text{)} \\ V &= \text{fluid velocity (m/sec)} \\ g &= \text{gravitational acceleration (m/sec}^2\text{)} \\ dZ &= \text{vertical elevation change (m) of the flow path over flow length } dL \end{aligned}$$

The first term on the right-hand side of Eq. 5.2, which constitutes the pressure drop due to friction in a flowing system, is generally of the greatest interest, since this is usually the largest source of pressure loss. For flow in pipes and ducting, this term is extremely well characterized, both on a theoretical basis and in terms of models and correlations for practical engineering applications. For flow in a packed bed, the basic fluid flow behavior is considerably more complicated and is much more difficult to adequately characterize with a simple model. The theoretical approach generally used is to treat the packed bed as a bundle of crooked tubes of varying cross-sectional area, and the relatively simple model in Eq. 5.2, which was developed for a single straight tube, is used to develop a separate formulation for the bundle of crooked tubes that make up the packed bed.

In this approach, the velocity of the flow field within the particle bed is characterized using the superficial velocity, which is generally calculated as the volumetric flow through the system divided by the total cross-sectional area of the bed. The superficial velocity is related to the velocity field within the bed by means of the bed porosity, through the relationship

$$U_s = \varepsilon V \quad (5.3)$$

where

$$\begin{aligned} U_s &= \text{superficial velocity (m/s) for the packed bed} \\ \varepsilon &= \text{bed porosity (dimensionless)} \end{aligned}$$

The hydraulic diameter of the flow, which in pipes and tubes is normally characterized using the ratio of the flow cross-sectional area and the wetted perimeter of the flow channel, is characterized for a particle

bed as a function of the particle diameter and the bed porosity. The hydraulic diameter of the packed bed, therefore, can be expressed as

$$D_h = \frac{2\varepsilon}{6(1-\varepsilon)} D_p \quad (5.4)$$

where

$$\begin{aligned} \varepsilon &= \text{bed porosity (dimensionless)} \\ D_p &= \text{particle diameter (m)} \end{aligned}$$

Using these definitions, the friction component of the pressure drop relationship given by Eq. 5.2 can be expressed in terms of the superficial velocity and the bed porosity, both of which can be determined for a given system, even though the true fluid velocity and hydraulic diameter are essentially unknown. Substituting these relationships into Eq. 5.2, with appropriate definitions, yields the following relationship for the friction pressure drop:

$$\left(\frac{dP}{dL} \right)_f = \frac{3f(1-\varepsilon)\rho U_s^2}{\varepsilon^3 D_p} \quad (5.5)$$

where

$$\begin{aligned} (dP/dL)_f &= \text{pressure drop (Pa) due to friction in the particle bed over length } dL \\ \rho &= \text{fluid density (kg/m}^3\text{)} \end{aligned}$$

This is the basic formula for correlating pressure drop measurements in packed beds to obtain useful relationships for predicting pressure drop as a function of flow rate. Because of the relatively high flow rate required to remove the total heat load of 300 MW in the AFPR, the flow in the particle beds comprising the core (i.e., the annular fuel channels) is expected to be in the turbulent regime, rather than in laminar flow. For turbulent flow conditions, the relationship expressed in Eq. 5.5 was modified by Ergun (Ergun, 1952) to include a viscous dissipation term. The resulting friction pressure drop correlation for packed beds is

$$\left(\frac{dP}{dL} \right)_f = \frac{C_1(1-\varepsilon)^2 \mu U_s}{\varepsilon^3 D_p^2} + \frac{C_2(1-\varepsilon)\rho U_s^2}{\varepsilon^3 D_p} \quad (5.6)$$

where

$$\begin{aligned} C_1 &= \text{empirical constant, experimentally determined value of 150} \\ C_2 &= \text{empirical constant, experimentally determined value of 1.75} \\ \mu &= \text{fluid viscosity (kg/m-s)} \end{aligned}$$

Substituting the relationship for the friction pressure drop in Eq. 5.6 into the modified Bernoulli equation (Eq. 5.2) yields the following relationship for the total pressure drop in the AFPR core,

$$dP = \frac{C_1(1-\varepsilon)^2 \mu U_s (dL)}{\varepsilon^3 D_p^2} + \frac{C_2(1-\varepsilon)\rho U_s^2 (dL)}{\varepsilon^3 D_p} + \rho g dZ \quad (5.7)$$

With the energy balance from Eq. 5.1, the momentum balance in Eq. 5.7 provides a means of investigating the relationship between flow rate and pressure drop in the AFPR core. Figures 5.3 and 5.4 present the results of calculations with these two equations for the range of acceptable conditions given in Table 5.1. For these calculations, the core exit subcooling was fixed at the minimum acceptable value of 5.6°C (10°F) below the saturation at the core exit pressure.

The curves in Figure 5.3 show that the flow rate needed to remove the 300 MW is strongly affected by the system pressure and the core inlet temperature. At a given inlet temperature, the higher the pressure, the

lower the flow rate. With the core exit subcooling specified at a fixed value (specifically, 5.6°C (10°F) below the saturation at the core exit pressure in these calculations), the increase in saturation temperature with increasing pressure results in a corresponding increase in the core exit temperature. At any given inlet temperature, therefore, increasing the pressure yields a larger temperature rise across the core, and as a result, less flow is needed to remove 300 MW of thermal energy. Conversely, increasing the inlet temperature at a given pressure means that the temperature rise across the core must be smaller, and consequently a larger flow rate is needed to remove 300 MW of thermal energy.

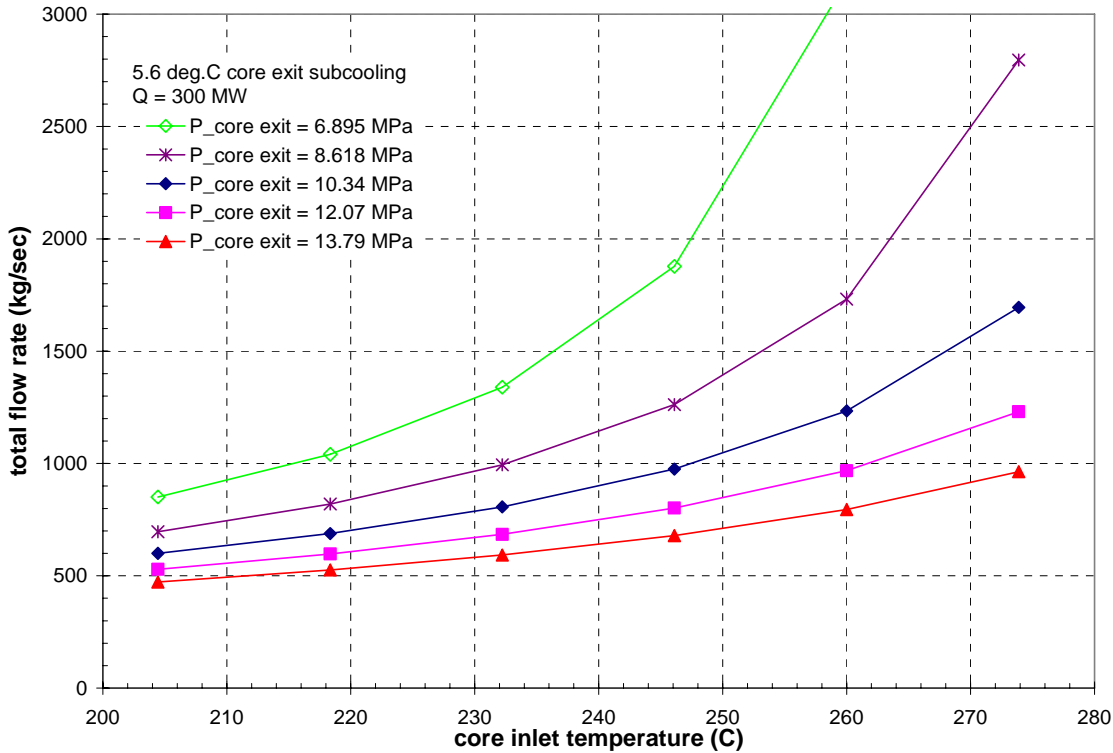


Figure 5.3. AFPR Core Flow Rate as a function of Inlet Temperature and Exit Pressure

The core pressure drop values resulting from these flow rates are presented in Figure 5.4. The curves in Figure 5.4 show that at any given pressure, the core pressure drop increases with increasing inlet temperature. Since increasing inlet temperature at a given pressure results in increasing core flow rate (as shown in Figure 5.3), the increase in pressure drop with increasing inlet temperature is to be expected. However, Figure 5.4 also shows that the higher the system pressure, the lower the core pressure drop at any given core inlet temperature. These results suggest that an acceptable core pressure drop can be obtained over a fairly large range of pressures and inlet temperatures.

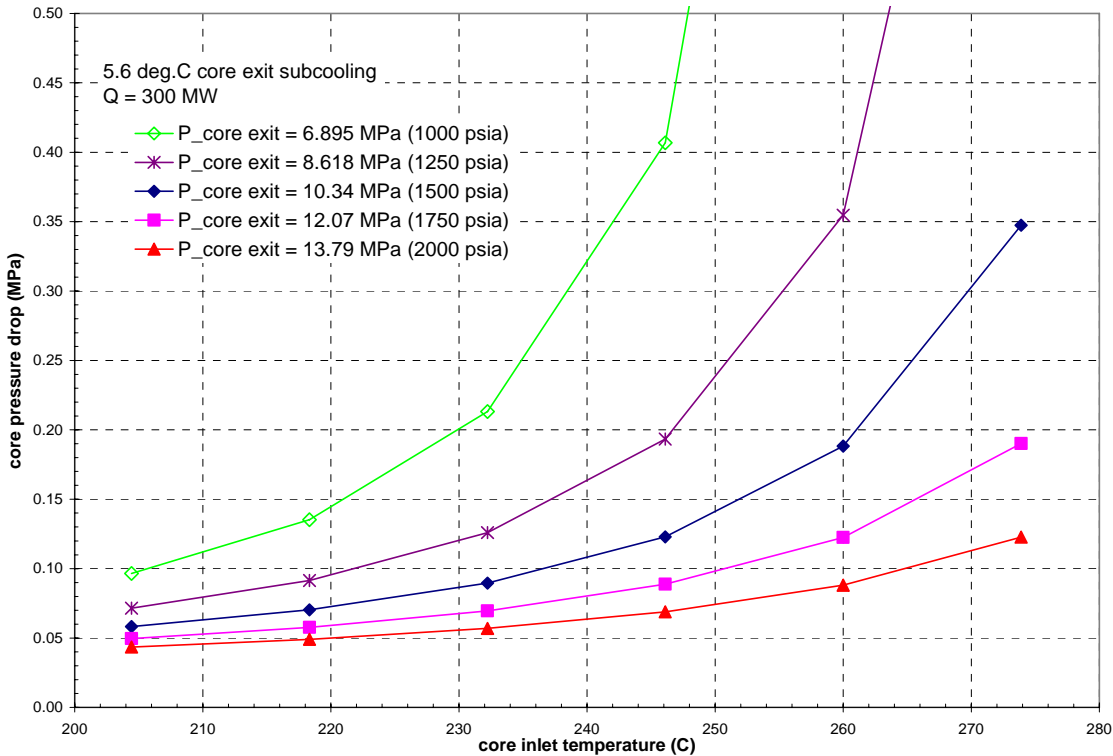


Figure 5.4. Core Pressure Drop as a function of Inlet Temperature and Exit Pressure

The results shown in Figures 5.3 and 5.4 suggest that there is considerable flexibility in acceptable operating conditions for the AFPR core. Single-phase vertical upflow through the core can remove 300 MW of heat at a reasonably low pressure drop for a relatively wide range of pressures and inlet temperatures. However, pressure drop is not the only constraint on core performance that must be considered in selecting suitable operating conditions. The above calculations were based on the assumption that the core exit temperature would be only about 5.6°C (10°F) below the saturation temperature. This assumption does not give much leeway for avoiding the possibility of boiling in the core, due to accident conditions, operational transients, or normal non-uniform temperature variations at the core exit (which could be due to unavoidable radial variations in the core, such as non-uniform power distributions or non-uniform inlet flow distributions). In addition, the core exit temperature essentially specifies the steam pressure that will be obtained in the steam generation step, since steam will be generated by throttling the flow to the saturation pressure corresponding to the core exit temperature. Design constraints unrelated to core thermal-hydraulic behavior may dictate a specific value or possible range of values on the steam pressure. (In the original AFPR design, with steam generated by means of boiling in the core, steam pressure was specified as 7.2 MPa (1045 psia).)

Core pressure drop results are shown in Figures 5.5 through 5.7 for core exit subcooling values ranging from 5.6°C (10°F) to 27.8°C (50°F) below saturation for a range of core exit pressures and core inlet temperature values. Figure 5.5 shows that for the low inlet temperature of 204°C (400°F), a core pressure drop of less than 0.138 MPa (20 psi) can be achieved at any reasonable core exit subcooling, for a core exit pressure of 6.895 MPa (1000 psia) or above. Figure 5.6 shows that when the core inlet temperature is somewhat higher, at 225°C (437°F), the core exit pressure must be at least 10.34 MPa (1500 psia) to achieve a core pressure drop of less than 0.138 MPa (20 psi) at all core exit subcooling values considered.

Figure 5.7 shows that when the core inlet temperature is relatively high, at 250°C (482°F), the core exit pressure must be at least 12.07 MPa (1750 psia) to obtain a core pressure drop below 0.138 MPa (20 psi) at the higher core exit subcooling values.

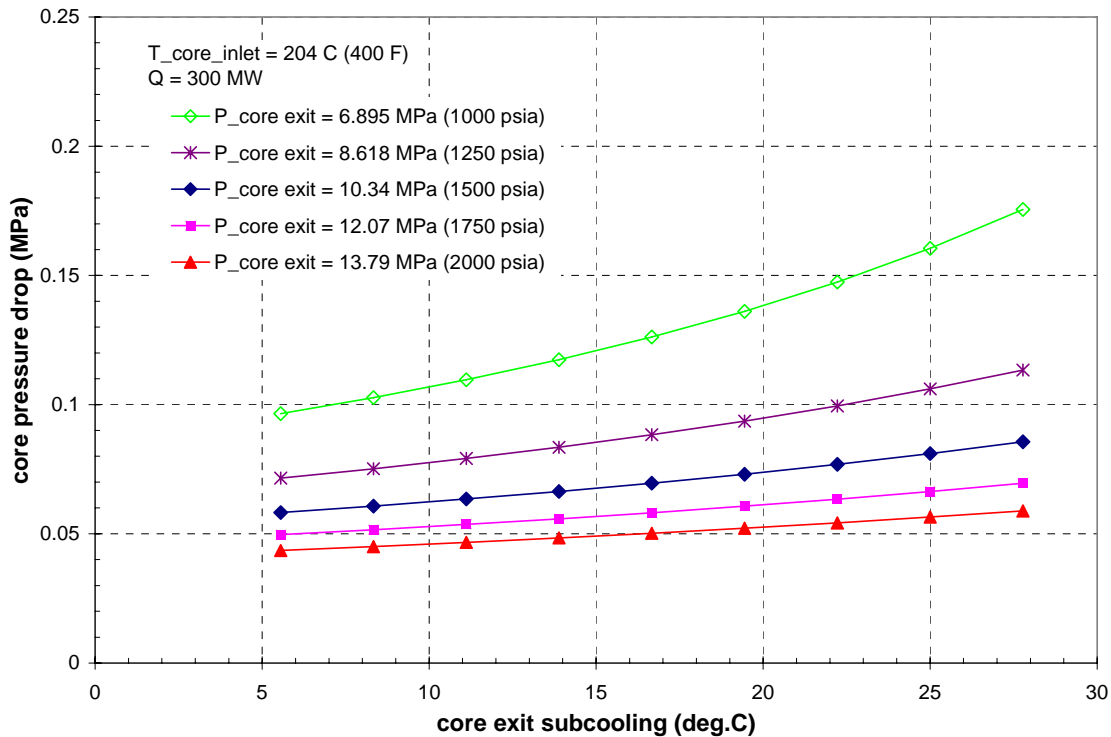


Figure 5.5. Core Pressure Drop as a function of Core Exit Subcooling at Core Inlet Temperature of 204°C (400°F)

All of the analyses presented so far point to the desirability of having a relatively low core inlet temperature and a relatively high core exit pressure, in order to obtain the lowest possible core pressure drop. Figure 5.8 shows that a relatively high core exit pressure is also desirable in order to have a relatively high steam pressure in the steam generating step of the cycle, and at the same time have adequate head room (in terms of the core exit subcooling), to protect against boiling in the core.

Based on these results, recommendations can be made for an acceptable range of normal operating conditions in the core, as follows:

1. core inlet temperature of 204°C (400°F)
2. core exit pressure of 12.41 MPa (1800 psia)
3. core exit subcooling of 16.7°C (30°F) below saturation at the core exit pressure.

These parameters produce the following operating conditions:

1. core pressure drop of 0.0564 MPa (8.2 psi)
 - a. compared to a typical BWR at about 40 psi and a PWR at about 25 psi
2. total flow rate of 585 kg/sec (1290 lbm/sec), assuming 1.5% bypass flow
 - a. compared to a typical PWR core loaded with 17x17 fuel, the core total flow rate is about 12,600 kg/sec (28,000 lbm/sec)

3. core exit temperature of 310°C (590°F)
4. steam generated at a pressure of 9.875 MPa (1432 psia).

These are not the only conditions that could produce acceptable operating conditions in the core, but they provide a reasonable starting point for further analysis.

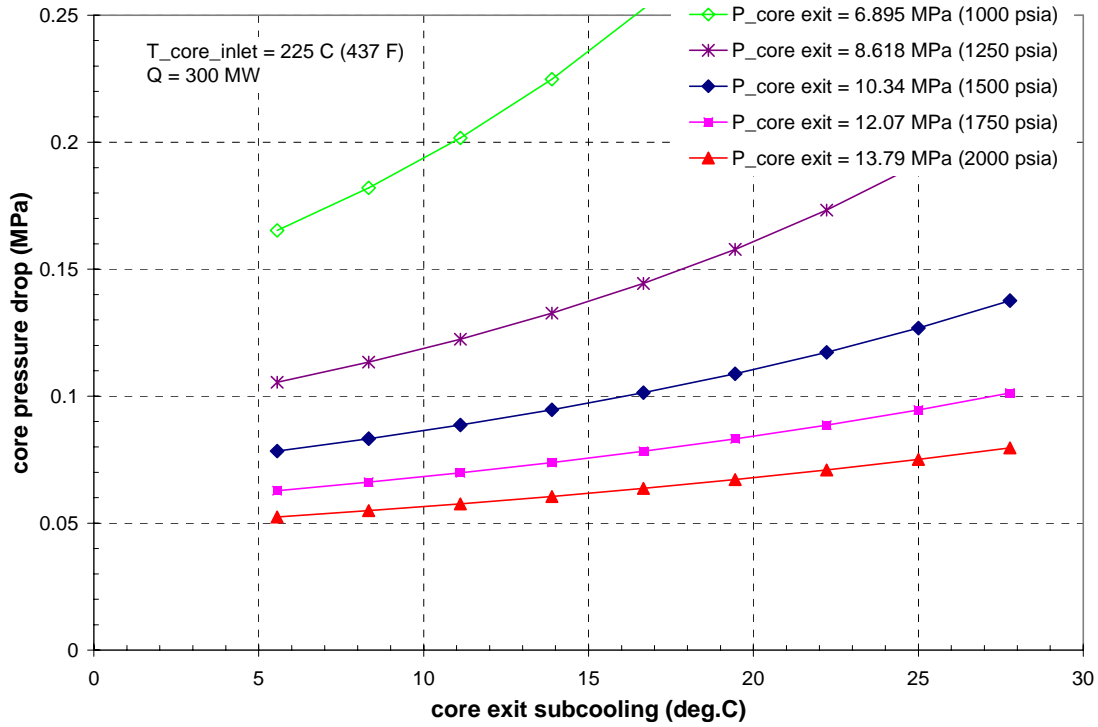


Figure 5.6. Core Pressure Drop as a function of Core Exit Subcooling at Core Inlet Temperature of 225°C (437°F)

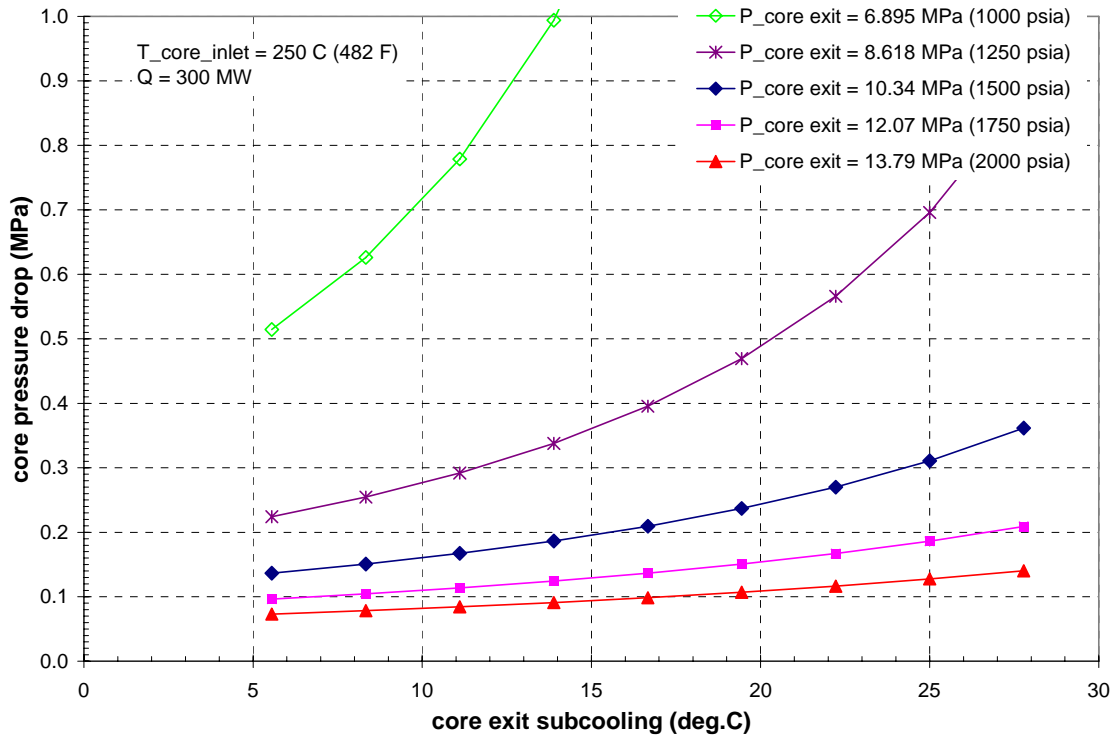


Figure 5.7. Core Pressure Drop as a function of Core Exit Subcooling at Core Inlet Temperature of 250°C (482°F)

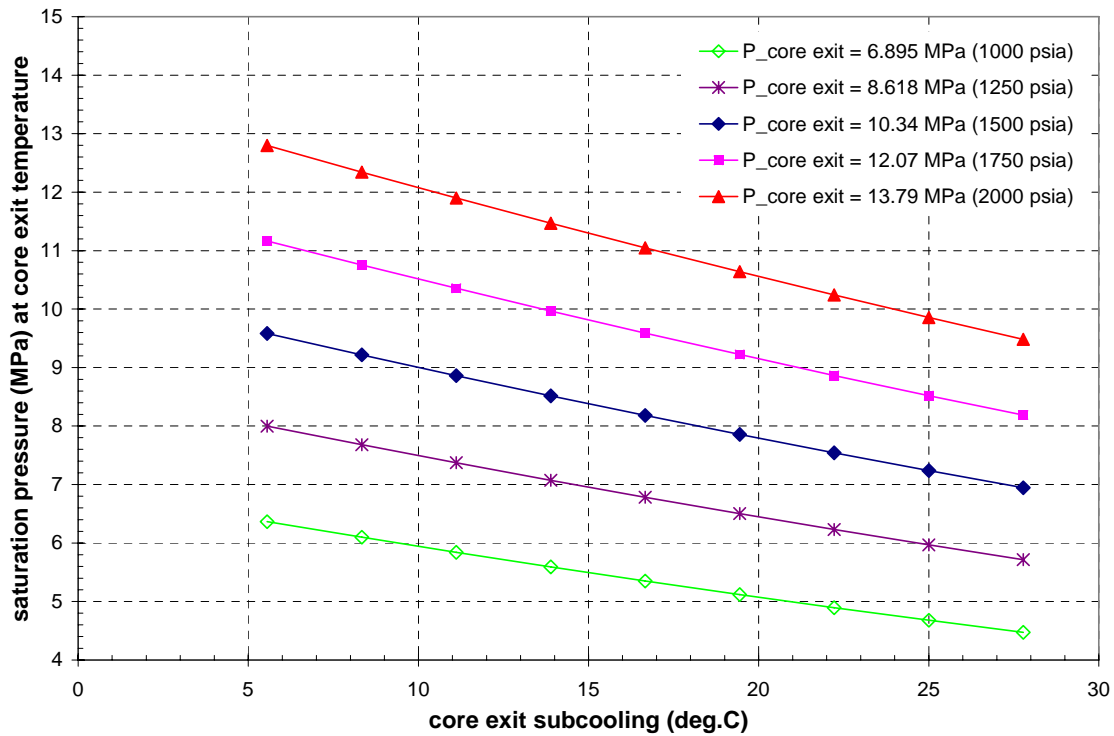


Figure 5.8. Saturation Pressure at Core Exit Temperature as a Function of Core Exit Subcooling

5.2.2 Material Temperatures in AFPR Core

As with the thermal-hydraulic analysis of the coolant conditions in the core, a detailed evaluation of the core material temperatures is beyond the appropriate scope of analysis at the current stage of the design process. It is necessary, however, to establish that material temperatures in the core will be within reasonable ranges for the expected core operating conditions. In particular, this means obtaining estimates of the fuel temperatures expected for the conditions including estimates of the fuel surface temperature and of the peak temperature within the fuel particles.

The temperature of a fuel particle within the core is determined by the rate of convection heat transfer from the surface of the particle, which is governed by the relationship

$$q = Nu \left(\frac{k}{D} \right) A_p (T_s - T_\ell) \quad (5.8)$$

where q = heat generated within a fuel particle (W)

Nu = Nusselt number

k = thermal conductivity of the coolant (W/m-°C)

D = characteristic length for heat transfer (m)

A_p = particle surface area (m²)

T_s = particle surface temperature (°C)

T_ℓ = coolant temperature (°C)

The Nusselt number for heat transfer within a particle bed is usually defined with the particle diameter as the characteristic length, so that

$$Nu = h \left(\frac{D_p}{k} \right)$$

The heat generated within the fuel is a known quantity, based on the characteristics of the fuel, and the coolant temperature can be estimated from the thermal-hydraulic analysis. The surface heat transfer coefficient, however, is a quantity that must be determined empirically and is highly dependent on the geometry and flow characteristics of a particular particle bed. Various heat transfer correlations have been developed to describe convection within a particle bed, but there is no general correlation that is suitable for application to all particle beds. Therefore, selecting a particular heat transfer correlation for application in the design of the AFPR core is not a simple matter.

In most particle bed reactors (of the chemical type, that is), the main design constraint related to the thermal characteristics of the bed is that it be kept at a uniform temperature. In some cases, the processes occurring in the bed involve endothermic or exothermic reactions, wherein the particles themselves generate or absorb heat from coolant flowing through the bed, but more typically, conditions are such that the particles are not a major source of heat deposited into the coolant. In most applications, the main design goal is to maintain the bed at some constant temperature throughout, or within some optimum range, and to achieve this, significant heat must be added through the walls of the bed. The heat transfer behavior of interest in such cases is the temperature distribution due the migration of heat from the walls into the particle bed.

Heat transfer correlations developed for 'typical' particle beds are, therefore, unlikely to be applicable to the conditions expected in the AFPR core, and it would be extremely difficult to justify the application of a particular correlation to obtaining estimates of fuel surface temperatures. Continued development of the detailed design of the AFPR will require an experimental program to determine the heat transfer

correlations that can appropriately describe convection within the particle beds comprising the fuel channels in the core. In the meantime, however, it is necessary to obtain some estimate of the surface temperatures within the core for postulated design conditions.

Even when lacking an appropriate heat transfer correlation for the geometry and flow conditions of the AFPR core, it is nevertheless possible to use the relationship in Eq. 5.8 to determine what heat transfer rate would be required to obtain a particular fuel surface temperature. For a given coolant flow rate and temperature, and the known heat generation rate within a fuel particle, it is possible to specify the desired surface temperature, evaluate the required Nusselt number, and hence the desired heat transfer coefficient. If the required Nusselt number is extremely large, it suggests that the desired surface temperature will not be achieved, and the actual surface temperature is likely to be much higher for the postulated flow conditions. If the required heat transfer coefficient is relatively small, then it is reasonable to suppose that the desired temperatures could be achieved within the system.

Based on the values given in Table 5.1 for acceptable ranges of core inlet temperature and peak fuel particle temperature, and the results of the thermal-hydraulic analysis presented in Section 5.2.1, the fuel surface temperature must be somewhere in the range 250-350°C (482-662°F). Figure 5.9 shows the predicted Nusselt number values obtained for this range of assumed fuel surface temperatures for postulated flow conditions in the AFPR core. Using this “back door” approach provides an evaluation of the likely heat transfer performance of the selected hydraulic conditions that were determined to produce acceptable core pressure drop and core exit temperature values in the analyses in Section 5.2.2. The results in Figure 5.9 show that the Nusselt number is less than 100, on average, in the AFPR core for fuel surface temperatures above about 290°C (554°F) for all flow conditions considered. A Nusselt number below 100 can generally be achieved even at a relatively modest heat transfer rate. This suggests that it will be possible obtain acceptable fuel surface temperatures in the core, even if the convection heat transfer coefficient is relatively low.

Exactly what constitutes an acceptable fuel surface temperature, however, depends on the heat transfer properties of the fuel particle itself. The peak temperature within the fuel particle depends on the rate of heat generation within the particle and the thermal conductivity of the fuel material and any cladding or coating on the particle surface. Considering a single fuel particle in isolation with a fixed heat transfer coefficient at the surface, the temperature distribution in the particle can be obtained from a straightforward application of the energy equation (Arpaci, 1966).

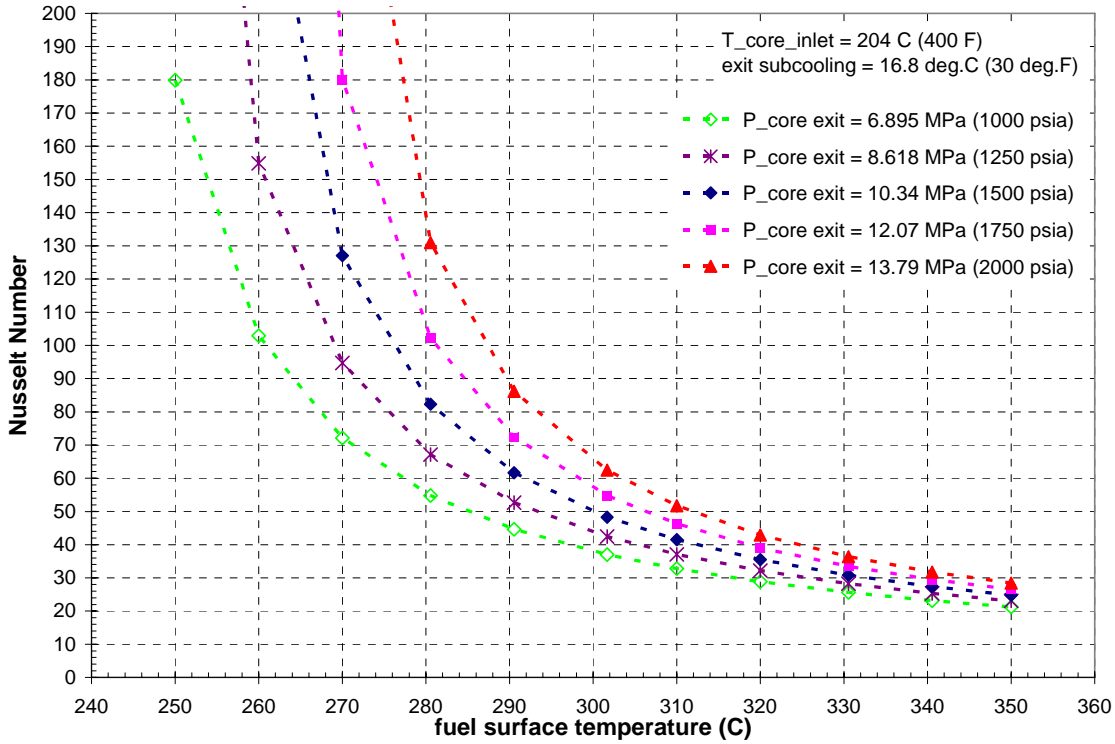


Figure 5.9. Estimated Nusselt Number for Acceptable Range of Fuel Particle Surface Temperatures

The temperature at the clad surface can be estimated from the Nusselt number and the known heat flux at the fuel particle surface. The temperature rise through the fuel particle cladding can be obtained from the conduction equation using the shape factor for a spherical shell, such that

$$q'' = k_c S \frac{(T_i - T_c)}{(R_p - R_f)}, \text{ for } S = \frac{4\pi R_p R_f}{R_p - R_f} \quad (5.9)$$

where T_c = clad temperature ($^{\circ}\text{C}$)

T_i = temperature on inner surface of clad, at clad/fuel interface ($^{\circ}\text{C}$)

R_p = particle radius (m)

R_f = fuel radius (m)

k_c = clad material thermal conductivity ($\text{W/m}\cdot^{\circ}\text{C}$)

The temperature within the heat-generating fuel region of the particle can be determined from the energy equation in spherical coordinates,

$$\frac{d}{dr} \left(r^2 \frac{dT_f}{dr} \right) + \frac{\Gamma_0}{k_f} \left[1 - \left(\frac{r}{R_f} \right)^2 \right] = 0 \quad (5.10)$$

where T_f = fuel temperature ($^{\circ}\text{C}$)

k_f = fuel material thermal conductivity ($\text{W/m}\cdot^{\circ}\text{C}$)

R_f = fuel radius (m)

Γ_0 = heat generation rate at center of fuel particle (W/m^3)

This formulation assumes a parabolic distribution of the heat generation rate in the fuel region of the particle, such that

$$\Gamma(r) = \Gamma_0 \left[1 - \left(\frac{r}{R_f} \right)^2 \right]$$

As described in detail in Section 2, the actual fuel material within the 0.5-mm diameter fuel particle consists of approximately 2000 spherical kernels of UO₂ distributed essentially uniformly throughout a Zircaloy matrix. The actual heat generation rate distribution within a fuel particle, therefore, can only be approximated by a smooth parabolic distribution. However, for the purposes of this preliminary analysis, the distribution of the heat generation rate is unimportant. Because the fuel particles are small (only about 10 μm in diameter), the exact shape of the heat generation rate profile will not have a large effect on the temperature at the center of the particle. The uncertainty incurred by this assumption is a small price to pay for the luxury of an exact solution to the energy equation for this configuration, which gives the temperature distribution in the fuel region as

$$\frac{T_r(r) - T_i}{\Gamma_0 R_f^2 / k_f} = \frac{7}{60} - \left(\frac{r}{R_f} \right)^2 \left[\frac{1}{6} - \frac{1}{20} \left(\frac{r}{R_f} \right)^2 \right], \quad 0 \leq r \leq R_f \quad (5.11)$$

Applying this relationship, with the further simplifying assumption of using the average heat generation rate in the fuel particle in place of the peak rate for the Γ_0 term, shows that the temperature gradient through the fuel particle should be very small over the range of fuel surface and center temperatures of interest for normal operation. Figure 5.10 shows a plot of the fuel center temperature as a function of fuel surface temperature, and over this range, the surface-to-center temperature difference is less than 5°C (9°F), and is essentially linear.

These results indicate that the fuel temperatures in the core should be well within the acceptable range, as described in Table 5.1, for normal operating conditions. Figure 5.11 shows the fuel temperatures (surface and center) for a large range of Nusselt number values, assuming nominal operating conditions of 12.41 MPa (1800 psia), core inlet temperature of 204°C (400 °F), and core exit subcooling of 16.7°C (30°F) below saturation at the core exit pressure. For a Nusselt number greater than about 8, the fuel temperatures can be expected to be below 350°C (662°F) for these conditions. A Nusselt number of 8 requires only a modest rate of heat transfer, and in general, the heat transfer rates obtained in the particle bed should be much higher, based on the expected flow rate, operating pressure, and material and coolant temperatures in the bed.

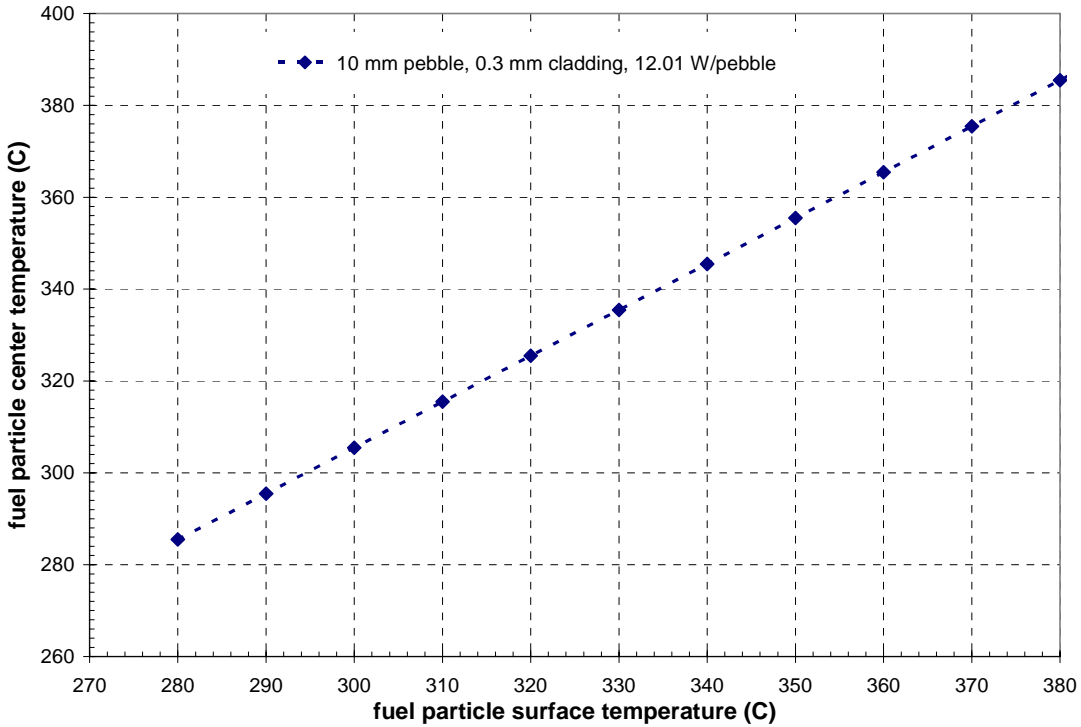


Figure 5.10. Fuel Particle Center Temperatures for Acceptable Range of Fuel Particle Surface Temperatures

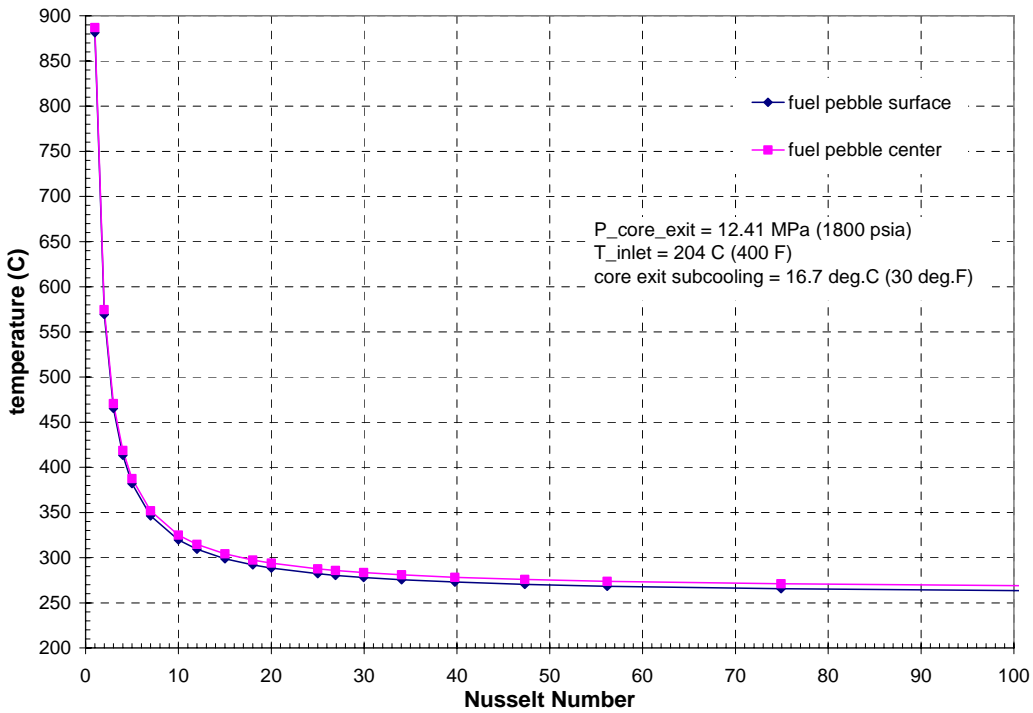


Figure 5.11. Fuel Particle Center and Surface Temperatures as a Function of Nusselt Number for Heat Transfer to Coolant

The results presented in Figures 5.9 through 5.11 are for average coolant and fuel temperatures. A more detailed evaluation of peak temperatures and core temperature distributions would require a more finished design and more sophisticated analyses employing computational fluid dynamics and heat transfer simulations. However, these results show that the AFPR core can be operated within the desired range of conditions, with acceptable coolant and fuel temperatures in single-phase vertical upflow of light water.

5.3 Core Cooling in Accident Conditions

At this point in the conceptual design phase, the specific details of accident conditions that the AFPR might be subjected to cannot be precisely defined. However, the general types of accident conditions that might be expected to be the most severe for any reactor system are reasonably well known. These are loss of pumping power (e.g., station black-out, pump trip, turbine trip), and pipe rupture in the primary system (e.g., double-ended guillotine break in vessel inlet piping). The salient feature of all events of this type is a rapid loss of flow to the core or rapid system depressurization, or both, which results in a sudden decrease in the ability to remove heat from the core. Fortunately, there is also generally an extremely rapid decrease in core power at the initiation of such events. Figure 5.12 illustrates this behavior with the standard power decay curve for LWRs and typical complete loss of flow accident (CLOFA) flow decay curves for operating commercial reactors.

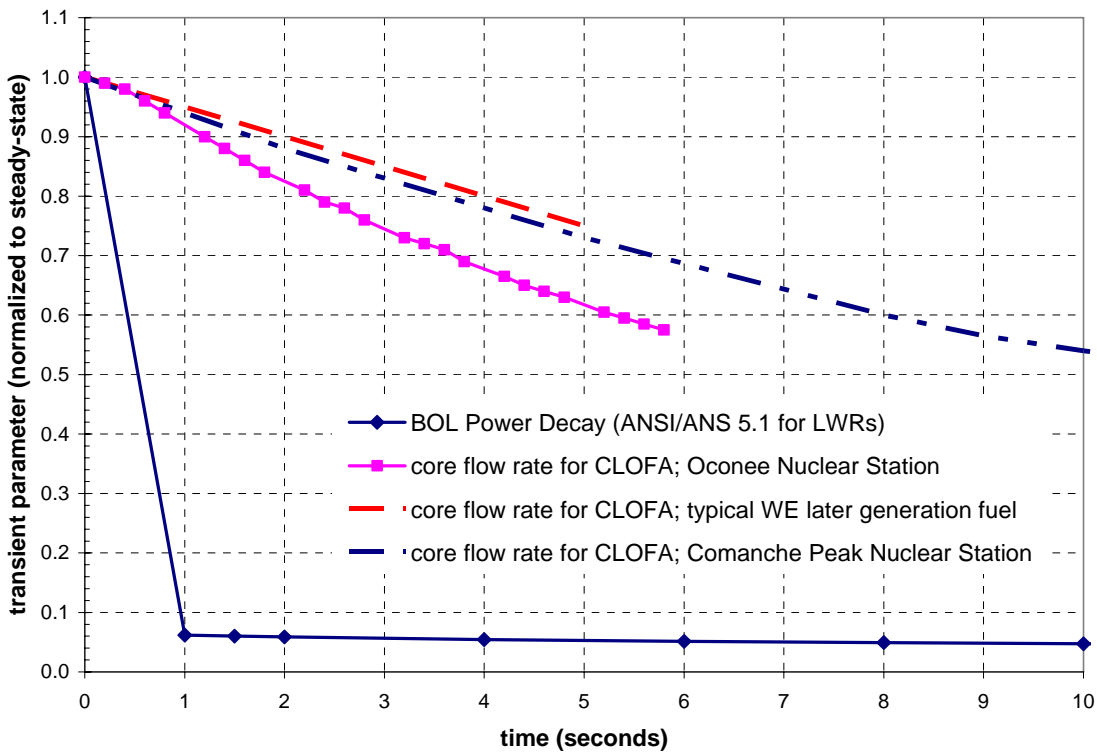


Figure 5.12. Core Flow Rate and Power Decay Forcing Functions for Complete Loss of Flow Accident (CLOFA) in typical LWRs

The general response of the core to such events can be evaluated in two distinct phases. First, there is the immediate response of the system to the sudden change in boundary conditions and second, the long-term response, which should be a new stable configuration for the system at “hot shutdown” conditions. The initial response to the AFPR core to rapidly decreasing inlet flow rate, system pressure, and thermal

power output is discussed in Section 5.3.1. The long-term response of the AFPR core, which consists of analysis of new steady-state conditions at greatly reduced flow, pressure, and power output, is discussed in Section 5.3.2.

5.3.1 Short-term Response of AFPR Core to Accident Conditions

The basic design of the AFPR core includes a number of features that make it less vulnerable to severe accident conditions than is the case with most commercial LWRs. The overall core will have an effective thermal conductivity that will result in better thermal dissipation. Reactor safety will be enhanced for many accident conditions (e.g., loss of flow and station blackout) based on the ability to dissipate heat through the pebble bed. Furthermore, simply reducing the total power output to the relatively low level of 300 MW(thermal), compared to the more typical 1000 to 3000 MW(thermal) capacity of large-scale nuclear stations greatly reduces the amount of thermal energy that must be removed with emergency core cooling measures in accident conditions. In the AFPR core, the peak fuel center temperature is expected to be only 3-6°C (5-10°F) above the temperature at the fuel particle surface, compared to the 600-1000°C (1112-1832°F) temperature difference between the cladding surface and fuel centerline that is typical of fuel in commercial LWR cores during normal operations and off normal events.

The significance of this difference becomes apparent from a brief examination of the energy balance on the fluid in the core, with the time-dependent terms included. In a simple one-dimensional representation, the energy balance can be expressed as

$$A_f \frac{\partial}{\partial t}(\rho h) + \frac{\partial}{\partial x}(\rho V h) A_f = Q_L \quad (5.13)$$

where A_f = cross-sectional area of flow (m²)
 ρ = local coolant density (kg/m³)
 h = local coolant enthalpy (kJ/kg)
 V = local coolant velocity (m/sec)
 Q_L = coolant linear heating rate (W/m)

The heat that must be absorbed and convected away by the coolant is simply the heat generated in the fuel particles. For transient conditions, this can be expressed as

$$Q_L L = Q''' V - (\rho c_p V) \frac{\partial T}{\partial t} \quad (5.14)$$

where L = axial length of fuel region of core (m)
 Q''' = heat generation rate (W/m³)
 V = volume of fuel material (m³)
 c_p = specific heat of fuel material (kJ/kg-°C)
 T = local fuel temperature (°C)
 t = time (seconds)

As the flow decreases in a loss-of-flow transient, the convective term in Eq. 5.13—that is, the $(\rho V h)$ term—will necessarily decrease, which means that the flow can removed less energy. However, because of the extremely rapid drop in the power output (as shown in Figure 5.12 for the power decay curve), the Q''' term in Eq. 5.14 will also decrease relatively rapidly. Because the power decreases much more rapidly than the flow rate, convection heat transfer might be expected to “keep pace” with the decreasing heat generation rate of the core, even as the flow rate decreases. However, there is also the effect of the

temperature derivative term in Eq. 5.14 to consider. With the heat generation rate decreasing more rapidly than the rate of flow decrease, the severity of the transient is governed primarily by the amount of energy stored in the fuel, as represented by the term containing the time-derivative of the temperature. For UO_2 fuel, the higher the steady-state operating temperature, the larger the $\partial T/\partial t$ term will be in the transient, and the more energy that must be carried away by the (rapidly decreasing) flow rate. For the AFPR core, this term should be at least two orders of magnitude smaller than would be expected in commercial LWR fuel for a comparable transient.

In general, the relatively low thermal capacity of the AFPR core suggests that the thermal response of the fuel in a transient will have a relatively small time constant, and the fuel temperature will tend to closely follow the power decay curve. If loss-of-flow transients in the AFPR follow the same general pattern as in typical LWRs, with the flow rate decreasing much more slowly than the power decay curve, there should not be a large time lag between a decrease in power generation rate and a decrease in fuel temperature, even when the flow is also decreasing.

5.3.2 Long-term Response of AFPR Core to Accident Conditions

The desired end state for a severe accident condition in a reactor is a stable hot-shutdown condition, in which the decay heat generated in the core can be removed by the emergency core cooling system, or a back-up system providing a stable but relatively low flow rate, compared to normal operating conditions. In the AFPR, one of the design goals is to develop a primary system that can sustain adequate core cooling in hot-shutdown mode indefinitely with natural recirculation only, and will not require positive pumping power to maintain core temperatures within acceptable limits. The postulated mechanism for driving recirculating flow through the core is the density difference between coolant in a cold “downcomer” region and hotter fluid in the core. (This configuration implies two significant features that must be included in the system design; a feedwater flow path that has a very small inherent pressure drop, and an efficient means of removing heat from the single-phase flow exiting the core under emergency conditions. However, these are reasonable constraints, and do not imply any severe limitations on the overall reactor vessel and system design.)

Because of the extremely low decay heat generated by the AFPR core, and the relatively low flow rate needed to cool the fuel particle bed, natural recirculation cooling could be a viable option for hot-shutdown conditions. Table 5.2 summarizes the projected decay heat levels for the AFPR core following reactor shutdown from 300 MW. As can be seen from Table 5.2 (and also Figure 5.12), the core thermal output drops by 95% within 5 seconds of shutdown, from 300 MW to approximately 15 MW. In less than 3 hours, the total core thermal output is less than 1% of full power. The flow rate required to remove this extremely reduced thermal output is relatively small. Figure 5.13 shows the core flow rate that would be required to remove this amount of heat for a range of postulated core exit pressure values, from the nominal operating pressure of 12.41 MPa (1800 psia) to the relatively low value of 0.698 MPa (100 psia). Figure 5.14 shows the friction pressure drop through the core for these postulated flow rates.

The required shutdown flow rates illustrated in Figure 5.13 are for the most part less than 1% of the total core flow rate at full power. Even for the highest decay heat (1.8 MW at 1 day after shutdown) at the lowest pressure considered, the required flow rate is less than 5% of the full power flow rate. Assuming that the full 3-m height of the core could be made available to provide the needed driving head, natural recirculation flow might be sufficient to provide the driving pressure needed to sustain the extremely small pressure drops shown in Figure 5.14. This suggests that with thoughtful design of the primary

system and emergency core cooling features, natural recirculation flow could be a viable means of cooling the AFPR core in hot shutdown conditions.

Table 5.2. Decay Heat After Shutdown in AFPR Core

| Time after shutdown | Decay heat (MW) |
|---------------------|-----------------|
| 1 second | 18.6 |
| 5 seconds | 15.0 |
| 2.2 hours | 3.0 |
| 1 day | 1.8 |
| 1 month | 0.7 |
| 1 year | 0.3 |
| 5 years | 0.1 |

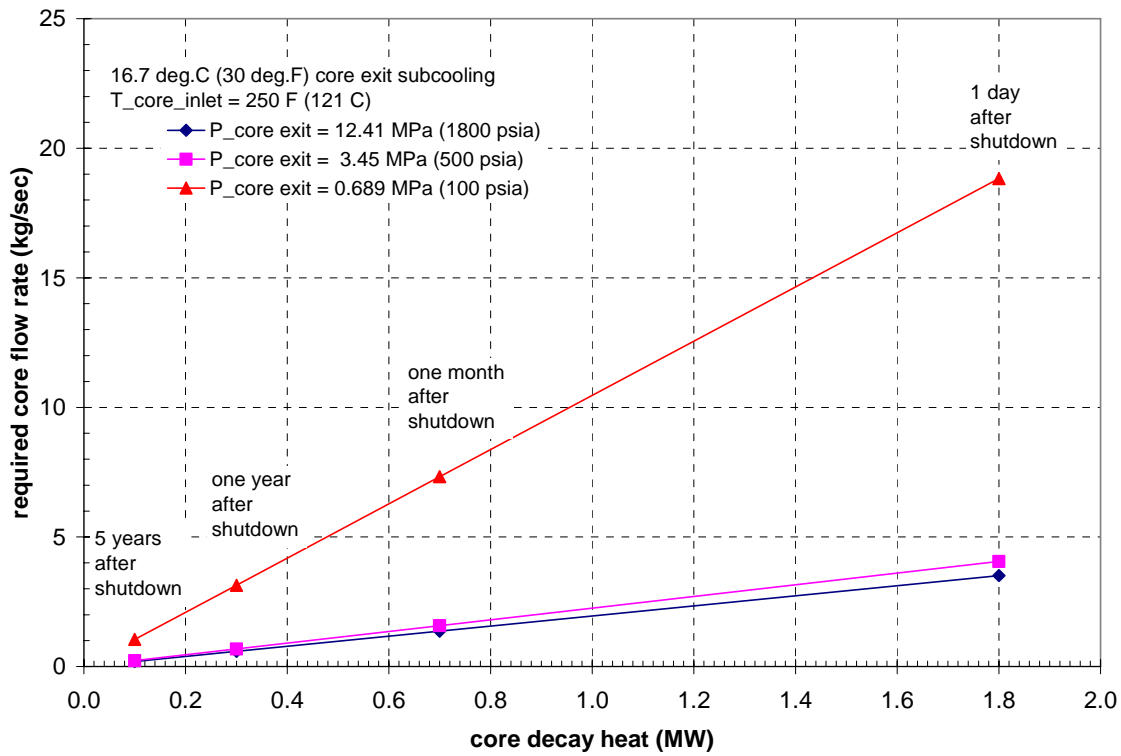


Figure 5.13. Flow Rate Required to Remove Decay Heat in Hot Shutdown Conditions for AFPR Core

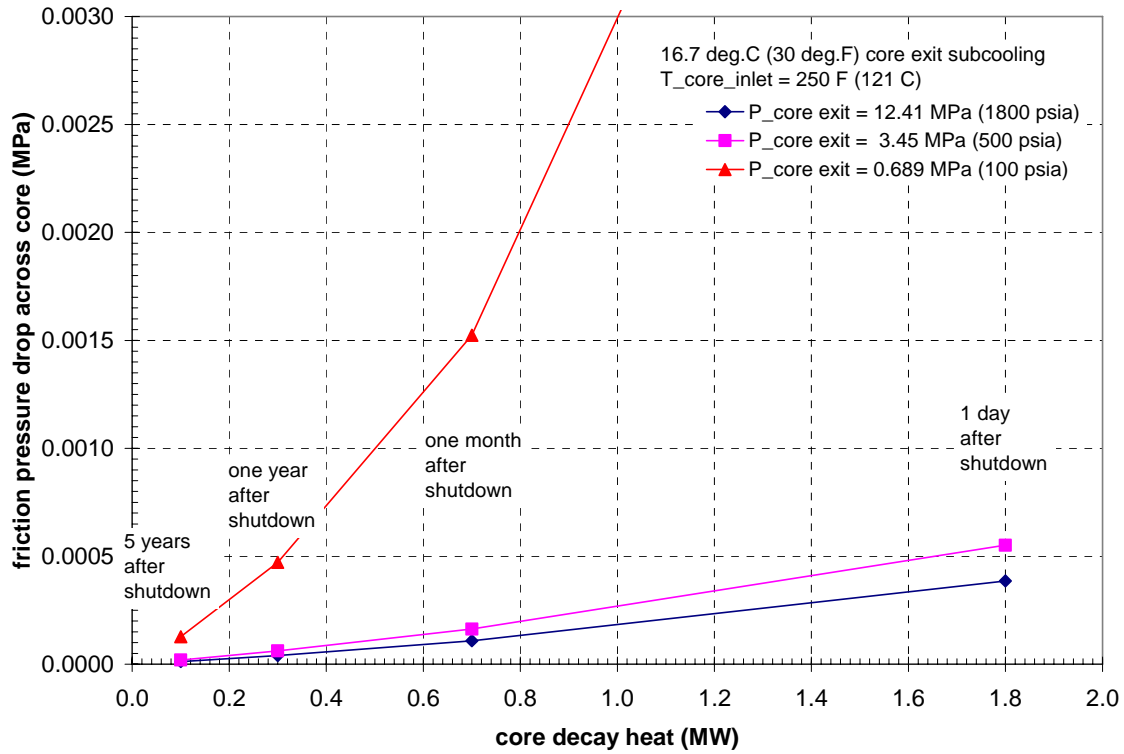


Figure 5.14. Friction Pressure Drop in Particle Bed Core for Flow Rate Required to Remove Decay Heat in Hot Shutdown Conditions

6.0 Conclusions and Recommendations for Future Work

Preliminary design of a new innovative spherical cermet fuel for use in grid-appropriate LWRs has been presented. The preliminary design results indicate that this new fuel form would perform well in an LWR environment for 20+ years. The advantages of such a fuel form over existing zircaloy clad fuel are as follows:

- ~3 times higher thermal conductivity,
- lower fuel temperatures over the life of the reactor,
- good fission product retention, and
- good performance at high burnup.

Preliminary neutronics, thermal-hydraulics, and fuel performance studies have been completed and suggest that the proposed 10-15 mm diameter spherical cermet fuel element would be an ideal fuel for use in a small grid appropriate reactor. Furthermore, industry has developed fuel assemblies capable of housing spherical fuel elements. One such concept is reported in a U.S. patent filed by Blanpain et al. in 2004. The fuel assembly replaces a standard 17X17 PWR assembly and can be used in existing PWRs as shown in Figure 6.1.

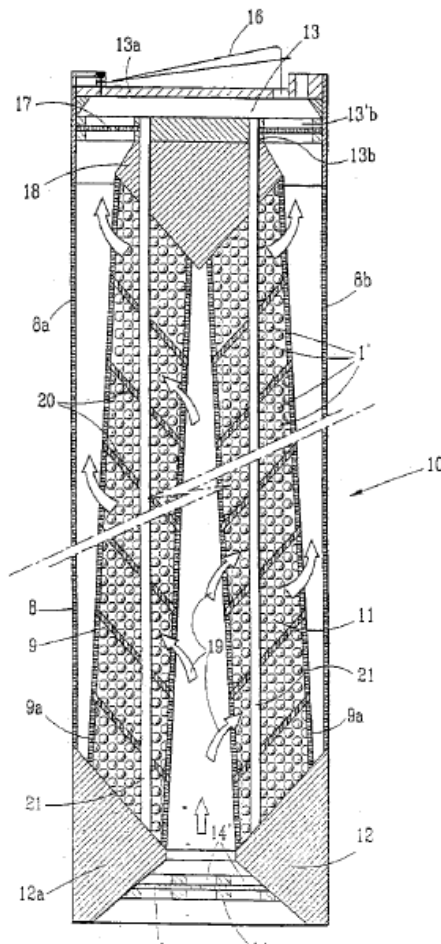


Figure 6.1 PWR Pebble Bed Fuel Assembly

A summary of key AFPR system parameters associated with the use of this new fuel in a small LWR (e.g., AFPR-100) is presented in Table 6.1. Further work could be done to greatly minimize the delta T across the core.

Table 6.1 Summary of Key System Characteristics with Spherical Cermet Fuel Elements

| Core Parameter | Value |
|--|---|
| Thermal Power | 300 MWt |
| Core Height | 3.0 m |
| Core Diameter | 3.0 m |
| Core Volume | 21.1 m ³ |
| UO ₂ Mass | 36.1 Mt |
| Coolant Conditions | |
| Coolant | Water |
| Inlet Temperature | 204°C |
| Outlet Temperature | 310°C |
| Average Coolant Temperature | ~260°C |
| Coolant Pressure | 12.4 MPa |
| Pressure drop across the core | 0.06 MPa |
| Spherical Fuel Characteristics | |
| UO ₂ enrichment | 12% |
| Kernal Size | 500 μm |
| Pebble Size | 10 mm |
| Outer Coating Thickness | 300 μm |
| Fuel Zones | 4 |
| Pebble Bed Porosity | 0.35 |
| Number of pebbles in reactor | ~21,000,000 |
| Fuel, Lifetime, and Damage Conditions | |
| Peak fuel center temperature above surface | 3-6°C |
| Average particle heat generating rate | 36.9 W |
| Peak fuel burnup | ~100 GWd/MTU |
| Peak dose to structural materials | 35 dpa-SS |
| Average fast flux (E>0.1 MeV) | 1x10 ¹⁴ n/cm ² -s |
| Fast fluence (E>0.1 MeV) | 7x10 ²² n/cm ² |
| Core lifetime (without optimization) | 20+ years |

Based on this study efforts are continuing in FY 2007 to demonstrate key fuel fabrication steps (i.e., kernel coating, pebble pressing, and pebble coating). The fabrication demonstration will include consideration of incorporating burnable absorbers either within or on the surface of the fuel elements. Materials testing will include sectioning for metallography, SEM and perhaps TEM examination of the interface regions to search for deleterious reaction zones, porosity measurements, density measurements, and thermal diffusivity measurements to characterize the thermal properties. Continued neutronic evaluation of the fuel concept will study the use of burnable absorbers and alternate fuel materials (e.g. ThO₂) as well as define in more detail parameters such as zonal enrichment schemes, reactivity coefficients, and control rod worth. Thermal-hydraulic studies will continue to optimize flow orificing schemes and evaluate accident scenarios and the possibility of passive cooling after shutdown. The study will employ computational modeling in conjunction with targeted experiments. This work seeks to build on the historically strong focus at the laboratory on advanced fuels and materials development and characterization.

7.0 References

- Armstrong, PE and HL Brown. 1964. *Transactions AIME*, 230:962.
- Arpaci, VS. 1966. *Conduction Heat Transfer*. Addison-Wesley, Boston, MA.
- Berna, GA, CE Beyer, KL Davis, and DD Lanning. 1997. "FRAPCON-3: A Computer Code for the Calculation of Steady-State, Thermal-Mechanical Behavior of Oxide Fuel Rods for High Burnup," NUREG/CR-6534 Vol. 2, Pacific Northwest National Laboratory, Richland, Washington.
- Carslaw, HS and Jaeger, JC. 1959, *Conduction of Heat in Solids*. Oxford Science Publications
- El-Wakil, MM. 1978. *Nuclear Heat Transport*. American Nuclear Society, La Grange Park, IL
- Erfiling, HD. 1939. *Annalen der Physik*, 34:136.
- Fiero, I.B., M.A. Krammen, and H.R. Freeburn. 1987. ESCORE -the Steady-State Core Reload Evaluator Core: General Description EPRI-NP-5100, Projects 2061-6, -13 Final Report. Prepared for Electric Power Research Institute, Palo Alto, California.
- Finnk, JK and L. Leibowitz. 1995. *Journal of Nuclear Materials*, 226:44.
- Geelhood, KJ, CL Painter, DJ Senor, and HE Adkins. 2006. "Feasibility Assessment of AFPR Reference Fuel Particle Concept from a Materials Standpoint," *PNNL-xxxxx*. Richland, WA: Pacific Northwest National Laboratory.
- Greenwood, LR et al. 1985. SPECTER: Neutron Damage Calculations for Materials Irradiations, ANL/FPP/TM-197, Argonne National Laboratory.
- Hagrman, DL, GA Reymann, and RE Mason. 1981. *MATPRO-Version 11 (Revision 2). A Handbook of Materials Properties for Use in the Analysis of Light Water Reactor Fuel Rod Behavior*, NUREG/CR-0479 (TREE-1280, Rev. 2), EG&G Idaho, Inc., Idaho Falls, ID.
- Ho, CY, RW Powell and PE Liley. 1972. *Journal of Physical Chemistry Reference Data*, 1:279.
- Hunt, RD and JL Collins. 2004. "Uranium Kernel Formation Via Internal Gelation," *Radiochemica Acta*, 92:909-915.
- Kato, S, S. Yoshimuta, T Hasumi, K Sato, K Sawa, S Suzuki, H Mogi, S Shiozawa, and T Tanaka. 1998. "Fabrication of HTTR First Loading Fuel," *Proceedings of the International Working Group of Gas-Cooled Reactors Technical Committee Meeting, IAEA-TECDOC—1210*, Beijing, China, 2-4 November 1998, pp. 187-199. Vienna, Austria: International Atomic Energy Agency.
- Kodas, TT and MJ Hampden-Smith. 1994. *The Chemistry of Metal CVD*. Weinheim, Germany: VCH Publishers.
- Lanning, DD, CE Beyer, and CL Painter. 1997. "FRAPCON-3: Modifications to Fuel Rod Material Properties and Performance Models for High-Burnup Applications," NUREG/CR-6534 Vol. 1, Pacific Northwest National Laboratory, Richland, Washington.
- Lanning, DD, CE Beyer, and KJ Geelhood. 2005. "FRAPCON-3 Updates, Including Mixed-Oxide Fuel Properties," NUREG/CR-6534 Vol. 4, Pacific Northwest National Laboratory, Richland, Washington.
- M. Kinoshita, T. Sonoda, S. Kitajima, A. Sasahara, T. Kameyama, T. Matsumura, E. Kolstad, V.V. Rondinella, C. Ronchi, J.-P. Hiernaut, T. Wiss, F. Kinnart, J. Ejton, D. Papaioannou, Hj. Matzke, 2004. "HIGH BURNUP RIM PROJECT: (III) Properties of Rim-Structured Fuel", Proceedings

- of the 2004 International Meeting on LWR Fuel Performance, Orlando, Florida, September 19-22, 2004, pp. 207-213.
- Maxwell, J.C. 1873. "Treatise on Electricity and Magnetism", UK: Oxford University Press.
- MatWeb. 2006. *Material Property Data*, <http://www.matweb.com>.
- McBride, B.J., S Gordon, and MA Reno. 1993. *NASA Technical Paper 3287*.
- Mueller, W.M., J.P. Blackledge, and G.G. Libowitz. 1968. *Metal Hydrides*. New York: Academic Press.
- Oxley, J.H., 1966. "Nuclear Fuels" in Vapor Deposition, (C. Powell, J. Oxley, and J. Blocher, Jr., eds.), pp. 484-505, John Wiley and Sons, New York.
- Painter, C.L., G.V. Tsiklauri, K.J. Geelhood, D.J. Senior, B.A. Johnson, and L.R. Greenwood. 2006. "A Summary of Technical Data Needed to Evaluate the Feasibility of Using a Modified TRISO Fuel Element in the Atoms for Peace Reactor Concept," *PNNL-16050*. Richland, WA: Pacific Northwest National Laboratory.
- PBMR. 2001. "Draft Scoping Report for the Proposed Manufacturing of Nuclear Fuel at Pelindaba in the North-West Province and the Associated Transportation of Nuclear Materials," *00-0247-05.002, Rev. 1*. Centurion, South Africa: The PBMR EIA Consortium.
- Pierson, H. 1999. *Handbook of Chemical Vapor Deposition*, 2nd Edition. New York: Noyes Publications.
- Petukhov, V. 2004. *High Temperatures-High Pressures*, 35/36:15.
- Powell, C.F., J.H. Oxley, and J.M. Blocher. 1966. *Vapor Deposition*. New York: John Wiley and Sons.
- Rayleigh, L. 1892. "On the Influence of Obstacles Arranged in Rectangular Order Upon the Properties of a Medium," *Phil. Mag.*, 34:481-502.
- Sargent-Welch Scientific Company. 1979. Periodic Table of the Elements, Skokie, Illinois.
- Sherman, A. 2006. Powdermet Technologies, Inc., per telecon
- Simnad, M.T. 1981. "The U-ZRHx Alloy: Its properties and use in TRIGA Fuel," *Nuclear Engineering and Design*, 64:403-422.
- Tsiklauri, G.V., T.E. Shaw, A.E. Waltar, D.V. Newman, R.J. Talbert, F.A. Garner, G.H. Meriwether, W.W. Little, Jr., R.P. Omberg, and B.W. Smith. 2005. "Long Life Small Nuclear Reactor Without Open-Vessel Re-Fueling," *PNNL-15134*. Richland, WA: Pacific Northwest National Laboratory.
- Tsuchiya, B., M. Teshigawara, K. Konoshi, S. Nagata, T. Shikama, and M. Yamawaki. 2002. "Isotope Effect in Thermal Diffusivity and Electrical Resistivity of Zirconium Hydride and Deuteride," *Nuclear Science and Technology*, 39-4:402-406.
- Yamanaka, S., K. Yoshioka, M. Uno, M. Katsura, H. Anada, T. Matsuda, and S. Kobayashi. 1999. "Thermal and Mechanical Properties of Zirconium Hydride," *Journal of Alloys and Compounds*, 293-295:23-29.

Distribution List

**No. of
Copies**

23 Pacific Northwest National Laboratory
P.O. Box 999
Richland, WA 99352

| | |
|--------------------|-------|
| D. J. Senior (5) | P8-10 |
| J. M. Cuta (2) | K7-15 |
| C. L. Painter (5) | K8-60 |
| H. E. Adkins | K7-15 |
| K. J. Geelhood (3) | K8-34 |
| D. W. Matson | K3-59 |
| D. W. Wootan (2) | K8-34 |
| G.H. Meriwether | K8-34 |
| J.L. Buelt | K8-46 |
| G.B. Dudder | K8-02 |
| J.R. Phillips | K8-46 |